

# Chemically speciated mass size distribution, particle ~~effective~~-density, shape and origin of non-refractory PM<sub>1</sub> measured at a rural background site in Central Europe

Petra Pokorná<sup>1</sup>, Naděžda Zíková<sup>1</sup>, Petr Vodička<sup>1</sup>, Radek Lhotka<sup>1,2</sup>, ~~Petr Vodička<sup>1</sup>~~, Saliou Mbengue<sup>3</sup>, Adéla Holubová Šmejkalová<sup>4</sup>, Véronique Riffault<sup>5</sup>, Jakub Ondráček<sup>1</sup>, Jaroslav Schwarz<sup>1</sup>, Vladimír Ždímal<sup>1</sup>

<sup>1</sup>Department of Aerosol Chemistry and Physics, Institute of Chemical Process Fundamentals, Czech Academy of Sciences, Rozvojová 135/1, 165 02 Prague, Czech Republic

<sup>2</sup>Institute for Environmental Studies, Faculty of Science, Charles University, Benátská 2, 128 01 Prague 2, Czech Republic

<sup>3</sup>Global Change Research Institute, Czech Academy of Sciences, Bělidla 986/4a, 603 00 Brno, Czech Republic

<sup>4</sup>Czech Hydrometeorological Institute, Air Quality Division, Na Šabatce 2050/17, 143 06 Prague, Czech Republic

<sup>5</sup>IMT Lille Douai, Institut Mines-Télécom, Université de Lille, Centre for Energy and Environment, F-59000 Lille, France

Correspondence to: Petra Pokorná ([pokornap@icpf.cas.cz](mailto:pokornap@icpf.cas.cz))

## Abstract

~~S~~The seasonal variability of non-refractory PM<sub>1</sub> (NR-PM<sub>1</sub>) was studied at a rural background site (National Atmospheric Observatory Košetice – NAOK) in the Czech Republic to ~~investigate~~ examine the ~~effect~~ impact of ~~atmospheric~~-regional and long-range atmospheric transport in Central Europe. NR-PM<sub>1</sub> measurements were performed by compact time-of-flight aerosol mass spectrometry (C-ToF-AMS), and the chemically speciated mass size distributions, ~~effective~~-density, shape and origin were discussed. ~~A~~The average PM<sub>1</sub> concentrations, calculated as the sum of the NR-PM<sub>1</sub> (after collection efficiency corrections – CE corrections of 0.4 and 0.33 in summer and winter, respectively) and the equivalent black carbon (eBC) concentrations measured by an aethalometer (AE), were  $8.58 \pm 3.70 \mu\text{g m}^{-3}$  in summer and  $10.08 \pm 8.04 \mu\text{g m}^{-3}$  in winter. Organics ~~dominated~~ were dominant during both campaigns (summer/winter:  $4.97 \pm 2.92/4.55 \pm 4.40 \mu\text{g m}^{-3}$ ), followed by  $\text{SO}_4^{2-}$  in summer ( $1.68 \pm 0.81/1.36 \pm 1.38 \mu\text{g m}^{-3}$ ) and  $\text{NO}_3^-$  in winter ( $0.67 \pm 0.38/2.03 \pm 1.71 \mu\text{g m}^{-3}$ ). The accumulation mode dominated the average mass size distribution during both seasons, with larger particles of all species measured in winter (mode diameters: Org: 334/413 nm,  $\text{NO}_3^-$ : 377/501 nm,  $\text{SO}_4^{2-}$ : 400/547 nm, and  $\text{NH}_4^+$ : 489/515 nm) ~~indicating pointing to~~ regional and long-range transport. However, since the winter aerosols were less oxidized than the summer aerosols (comparing fragments  $f_{44}$  and  $f_{43}$ ), the importance of local sources in the cold part of the year was still enough to be considered ~~not negligible~~ significant. ~~The average PM<sub>1</sub>-particle effective density, defined as the ratio of the mass to the volume of a particle, corresponded to higher inorganic contents during both seasons (summer:  $\sim 1.30 \text{ g cm}^{-3}$  and winter:  $\sim 1.40 \text{ g cm}^{-3}$ )~~ Although aged continental air masses from the south-east (SE) were rare in summer (7%), they were connected ~~related~~ with ~~to~~ the highest concentrations of PM<sub>1</sub>, eBC and all NR-PM<sub>1</sub> species, especially  $\text{SO}_4^{2-}$  and  $\text{NH}_4^+$ . In winter, slow continental air masses from the south-west (SW)

(44%) were linked to inversion conditions over Central Europe and were associated with the highest concentrations among all NR-PM<sub>1</sub> species as well as PM<sub>1</sub> and eBC. Average PM<sub>1</sub> material density ( $\rho_m$ ) corresponded to higher inorganic contents in both seasons (summer:  $\sim 1.30 \text{ g cm}^{-3}$  and winter:  $\sim 1.40 \text{ g cm}^{-3}$ ). However, the effective densities  $\rho_{eff}$  during episodes of higher mass concentrations  $\rho_m$  ranged calculated based on the particle number (mobility diameter) and mass size distribution (vacuum aerodynamic diameter) were even higher, ranging from  $1.340 - 1.460 \text{ g cm}^{-3}$  in summer and from  $1.340 - 1.5075 \text{ g cm}^{-3}$  in winter. The dynamic shape factors ( $\chi$ ) decreased slightly with particle mobility diameter ( $D_m$ ) in both seasons. This study provides insights into the seasonal effects and air mass variability on aerosol particles, focusing with focus on episodes of high mass and number concentrations measured at Central European rural background site. Although aged continental air masses from the SE were rare in summer (7%), they were connected with the highest concentrations of all NR-PM<sub>1</sub> species, especially  $\text{SO}_4^{2-}$  and  $\text{NH}_4^+$ . In winter, slow continental air masses from the SW (44%) were linked to inversion conditions over Central Europe and were associated with the highest concentrations among all NR-PM<sub>1</sub> measurements.

## 1. Introduction

Studies on airborne particulate matter (PM) are needed to better understand its temporal and spatial variations, atmospheric processing, long-term trends, adverse health effects and environmental consequences, and pollution sources (Putaud, et al., 2004; Tørseth et al., 2012; Belis et al., 2013; EEA 2019). Therefore, detailed analysis of the physicochemical properties of aerosol particles is crucial to understand their processes and lifetime in the atmosphere.

Aerosol particles can be characterized by many different properties such number concentration, mass concentration, particle size, mass, volume, density, shape etc. Particle density and shape is an important physical property of atmospheric particles and along with chemical composition is linked to particle emission sources and atmospheric physical and chemical ageing processes. The effective density, which is defined as the ratio of the mass of the particle to its apparent volume, assuming a spherical particle, and can be estimated by comparing the size distributions of the aerodynamic and mobility diameters, is a quantity reflecting the physiochemical properties of aerosol particles (e.g., DeCarlo 2004; Pitz et al., 2003, 2008; Hu et al., 2012; Qiao et al., 2018).

A network of measurement sites as the Aerosol, Clouds, and Trace Gases Research Infrastructure Network (ACTRIS, <https://www.actris.eu/>, last access: February 2022) enables to study the study of long-term variability of aerosol particle properties in the European environment. However, still a prevalent coarse time and size resolution of the measurements still limits our knowledge on the physicochemical properties of aerosol particles (Putaud et al., 2004; 2010; Cavalli et al., 2016). Over the last decades, a growing number of scientific studies have investigated the detailed chemical composition of PM with variable temporal resolutions (1, 12, and 24 hours or higher) using offline filter analyses (Putaud et al., 2010; Watson and Chow, 2011). Nowadays, online methods with high temporal resolutions (30 min and less) are available, as aerosol mass spectrometers (AMSs) utilized are utilized that can quantitatively measure chemical composition as well as the chemically resolved size distributions of submicron non-refractory PM (NR-PM<sub>1</sub>) (Jayne et al., 2000; Jimenez et al., 2003a). Although measuring the seasonal variability of NR-PM<sub>1</sub> is becoming more common (Bressi et al., 2021),

systematic studies considering chemically speciated mass size distributions are still rare. The available studies have also focused on new particle formation and growth, temporal variations, and the origin and sources of particles, including results presented from urban (Drewnick et al., 2004; Dall'Osto et al., 2009; Hersey et al., 2011; Freutel et al., 2013; Salimi et al., 2015; Kubelová et al., 2015), forestry (Allan et al., 2006), mid-altitude (Freney et al. 2011) and rural (Poulain et al., 2011; Milic et al., 2017) background environments.

Measurements ~~obtained~~ at rural background sites ~~that are~~ representative of wider areas are important ~~to study for investigating~~ the influence of regional and long-range transport as well as the long-term trends in PM characteristics. In the Czech Republic, the National Atmospheric Observatory Košetice (NAOK), officially classified as a Central European rural background site, ~~participates is involved~~ in the European Monitoring and Evaluation Programme (EMEP), Aerosol, Clouds, and Trace Gases Research Infrastructure Network (ACTRIS), and Global Atmosphere Watch (GAW) network. This site has been characterized in terms of the local PM<sub>2.5</sub> chemical composition and seasonal variability (Schwarz et al., 2016), the PM<sub>1</sub> isotopic composition (Vodička et al., 2019) and the PAHs ~~that are~~ bound to PM<sub>1</sub> (Křůmal and Mikuška, 2020). Studies conducted at NAOK have also characterized the long-term trends of atmospheric carbonaceous aerosols (Mbengue et al., 2018, 2020) and PM<sub>2.5</sub> elemental compositions and sources (Pokorná et al., 2018). The particle number size distribution (PNSD) and influence of in-cloud and -below-cloud scavenging have been investigated with long-term measurements by Zíková and Ždímal (2013, 2016). However, detailed work focused on the seasonal variability in PM chemical composition data with high temporal and spatial resolutions is still lacking at this site. In this paper we assess NR-PM<sub>1</sub> based on the chemically speciated mass size distribution, particle ~~effective~~-density, shape and origin during intensive campaigns in summer and winter. The focus of this study was to characterise individual episodes of high mass and number concentrations determined based on highly-time resolved measurement linked to ~~the~~ different air masses types, ~~and~~ thereby offering insights into the physicochemical properties and sources of aerosol particles arriving at a rural background site.

## 2. Materials and methods

### 2.1 Instrumentation

Two intensive sampling campaigns were carried out in July 2019 (1.7. – 31.7.) and in January-February 2020 (16.1. – 10.2.) at NAOK. During the campaigns, several physical and chemical atmospheric aerosol properties were measured together with complete meteorological data collected from a professional meteorological station (WMO station 11628).

The size-resolved NR-PM<sub>1</sub> chemical composition (the sum of organic, sulphate, nitrate, ammonium and chloride) was measured by a compact time-of-flight aerosol mass spectrometer (C-ToF-AMS, Aerodyne, USA, Drewnick et al., 2005) with a 5-min temporal resolution. The instrument was connected to an inlet consisting of a PM<sub>2.5</sub> sampling head (16.7 l min<sup>-1</sup>) and a Nafion dryer (Perma Pure MD-110-24P-4). Isokinetic sub-sampling was used to split the flow into AMS (0.1 l min<sup>-1</sup>) from the main flow. The AMS size ~~and~~ flow, as well as ~~and~~ ionization efficiency (IE) calibrations ~~were performed~~ in the brute-force single-particle mode (BFSP, Drewnick et al., 2005, monodisperse 350-nm ammonium nitrate aerosol particles) were performed in at the beginning, during and after of each campaign. The resulting IE was the average IE from all calibrations. Additionally, the measurements were performed with a HEPA

filter applied to the inlet to account for zero-value measurements and to adjust the fragmentation table (Allan et al., 2004).

Additionally, 12-h PM<sub>1</sub> filter samples were collected by a sequential Leckel Low Volume Sampler-3 (LVS-3), Sven Leckel Ingenieurbüro, Germany) for subsequent chemical analyses of cations, anions and monosaccharide anhydrides (levoglucosan, mannosan and galactosan) using ion chromatography (Dionex ICS-5000+ system, Sunnyvale, CA, USA). More details about the methods can be found in Kozáková et al., 2019.

The particle number concentration (PNC) and particle number size distribution (PNSD) were measured every 5 min by a mobility particle size spectrometer (MPSS, IFT TROPOS, Germany, with CPC 3772, TSI USA) in the size range of 10 – 800 nm (a detailed description of the measurement set-up can be found in Zíková and Ždímal, 2013). The cumulative particle number concentrations over seven size ranges (10 – 25 nm, 25 – 50 nm, 50 – 80 nm, 80 – 150 nm, 150 – 300 nm, 300 – 800 nm, and 10 – 800 nm) were subsequently calculated from the PNSD. Additionally, the 1-h PM<sub>2.5</sub> mass concentrations were measured using a beta-gauge (MP101M, Environement SA, France).

The concentrations of equivalent black carbon (eBC) were estimated using a 7-wavelength aethalometer (Model AE33, Magee Scientific, Berkeley, CA, USA) sampling through a PM<sub>10</sub> sampling head (Leckel GmbH) with a 1-min temporal resolution. Additionally, 4-h PM<sub>2.5</sub> online organic and elemental carbon (OC/EC) concentrations (Sunset Laboratory Inc., USA) were measured following the shortened EUSAAR2 protocol (Cavalli et al., 2010).

## 2.2 Data analysis

The standard data processing procedure of AMS data (i.e., m/z calibration, baseline subtraction, and air beam correction) was carried out by running the Squirrel v1.62 program in Igor Pro data analysis software (WaveMetrics, Inc.).

The statistical data treatment was performed using R version 3.6.1 (R Core Team, 2019) with the ggplot2 (Wickham, 2016) and Openair (Carslaw and Ropkins, 2012) packages.

### 2.2.1 Collection efficiency determination

To determine the collection efficiency (CE; Drewnick et al., 2005) in the AMS, PM<sub>1</sub> filter sampling with subsequent ion chromatography (IC) analysis was conducted in parallel with the AMS measurements. A comparison between the sulphate concentrations measured by AMS and by IC revealed the better suitability of the CE corrections for summer (CE = 0.40;  $y = 0.99x$ ,  $R^2 = 0.95$ ) as well as for winter (CE = 0.33;  $y = 1.00x$ ,  $R^2 = 0.81$ ) in comparison to the composition-dependent CE correction (CDCE; Middlebrook et al., 2012) shown in Fig. A1. Therefore, CE correction was applied to the AMS data for both seasons to maintain consistency in the data corrections. Similarly, using the same methodology, seasonal CE corrections (summer CE = 0.29 and winter CE = 0.35) were also successfully applied to AMS data measured at a suburban site in Prague (Kubelová et al., 2015).

### 2.2.2 Particle ~~effective~~ density and shape factor estimation ~~calculation~~



The effective density ( $\rho_{\text{eff}}$ ) and material density ( $\rho_m$ ) was estimated along with the dynamic shape factor inferred from the two densities. Two approaches were employed to calculate the particle effective density. In the first approach,

DeCarlo et al. (2004) gives three different possible definitions of the effective density estimation: i) from mobility and mass measurements, ii) as a fitted parameter, and iii) from mobility and aerodynamic measurements. Here we proceed from the latter definition with the AMS data representing the mass size distributions based on the vacuum aerodynamic diameter ( $D_{va}$ ) in the approximate size range approximately from of 450 to 78000 nm (calculated in Squirrel software extrapolated; in range- 1500 – 8700000 nm-in-reality), and MPSS data based on mobility diameter ( $D_m$ ) representing the  $dN/d\log D_p$  in the size range from 11.3 to 987 nm were utilized. In the MPSS-AMS data, the  $D_{mva}$  were recalculated to using the vacuum aerodynamic diameters mobility diameters with a density of  $1.5 \text{ g cm}^{-3}$ , and the  $D_{va}$  were then recalculated back to mobility diameters with the assumption of spherical particles as in DeCarlo et al. (2004):

$$D_{vam} = \frac{D_{vam}}{\rho_0 \rho} \rho \rho_0, \quad (1)$$

where  $D_m$  is the mobility diameter,  $D_{va}$  is the vacuum aerodynamic diameter,  $\rho_0$  is the water density, and  $\rho$  is the total density of particles, resulting in the sizes ranging from 7.53 to 658 nm. The position of the main mode of mass contribution distribution (analysis preformed with increment of  $0.05 \text{ g cm}^{-3}$ , uncertainty of the sizing of MPSS – within 3%, see Wiedensohler et al. 2017 and AMS – within 8%, see Takegawa et al., 2005) -was compared between the AMS and MPSS data to estimate the aerosol effective density ( $\rho_{\text{eff}}$ ).

The density was first used to recalculate the diameters and was later also used for the mass calculations. The  $dN$  data were calculated and used for the  $dV$  and  $dM$  distribution calculations. In the second approach, the mass concentrations of NR-PM<sub>1</sub> species and eBC were converted to the estimated size-dependent material density ( $\rho_m$ ) based on the following equation from Salcedo et al. (2006).

$$\rho_m = \frac{[Total_{AMS+eBC}]}{\frac{[NO_3^-]}{1.75} + \frac{[SO_4^{2-}]}{1.75} + \frac{[NH_4^+]}{1.75} + \frac{[Cl^-]}{1.52} + \frac{[Org]}{1.20} + \frac{[eBC]}{1.77}} \quad (2)$$

The densities were assumed to be approximately  $1.75 \text{ g cm}^{-3}$  for ammonium nitrate, ammonium sulphate, and ammonium bisulphate (Lide, 1991);  $1.52 \text{ g cm}^{-3}$  for ammonium chloride (Lide, 1991);  $1.20 \text{ g cm}^{-3}$  for organics (Turpin and Lim, 2001); and  $1.77 \text{ g cm}^{-3}$  for black carbon (Park et al., 2004).

From the two densities the Jayne Shape factor ( $S$ ) proposed by Jayne et al. (2000) was inferred and the dynamic shape factor ( $\chi$ ) assuming near the free molecular regime limit  $S \sim 1/\chi^{1/3}$  (Jimenez et al., 2003b, c; DeCarlo et al., 2004) was estimated.

### 2.2.3 Cluster analysis

For both campaigns, 96-hour backwards trajectories were calculated using the Hybrid Single-Particle Lagrangian Integrated Trajectory (HYSPLIT) model (Rolph et al., 2017) with a 500-m AGL starting position and Global Data Assimilation System (GDAS) Archive Information at a resolution of  $1^\circ \times 1^\circ$  as input data. The calculations were initialized every 6 hours for the cluster

analysis. For the episodes of high mass concentrations (Section 2.2.4) the trajectory ensemble option with calculation initialized every hour and a total duration of 72 hours was utilized. The trajectories were further clustered using Hysplit4 software based on the total spatial variance.

From HYSPLIT, the planetary boundary layer height data were extracted using the vmixing program ([https://www.ready.noaa.gov/HYSPLIT\\_vmixing.php](https://www.ready.noaa.gov/HYSPLIT_vmixing.php)). For the planetary boundary layer height calculations, the  $0.25^\circ \times 0.25^\circ$  Global Forecast System (GFS) dataset was used as input data to obtain a 3-hour temporal resolution.

## 2.2.4 Episodes of high particle number and mass concentrations

To determine episodes of high particle number and mass concentrations, a two-steps approach was utilized: i) the application of positive matrix factorization (PMF) to PNSDs and ii) depiction of the mass size distributions of nitrate, sulphate and organic NR-PM<sub>1</sub> species were depicted in a colour-coded 3D plot and, ii) episodes of high mass concentrations were chosen based on a set of criteria: high mass size distribution of at least one main NR-PM<sub>1</sub> specie corresponding to the season – summer/winter ( $NO_3^- \geq 0.5/0.2 \mu\text{g m}^{-3}$ ,  $SO_4^{2-} \geq 1/0.5 \mu\text{g m}^{-3}$ ,  $Org \geq 6/2 \mu\text{g m}^{-3}$ ); monomodal mass size distribution of all main NR-PM<sub>1</sub> species; duration of the episodes min 1.5 hours. Ten summer (S1 – 10) and thirteen winter (W1 – 13) high mass concentration episodes were selected. Additionally, due to the long duration of episode W6 and bimodal mass size distribution of Org, the episode was split into two sections: W6a (67 hours) and W6b (25.5 hours). The episodes were studied in detail from the organic fragments, mass size distribution, particle effective density (material density –  $\rho_m$  and effective density –  $\rho_{eff}$ ) and dynamic shape factor and mass size distribution perspectives.

### 2.2.4.1 PMF on PNSD

PMF (US EPA, version PMF 5.0) was applied to the seasonal 5-min PNSDs in the range from 10 nm to 800 nm to estimate the number and profile of the PNSD factors and their contributions to the receptor. Episodes in which the factor contributions to the total particle number concentrations were higher than 80 % were chosen for the subsequent particle effective density calculations.

The input data were prepared by merging three consecutive bins to reduce the noise in the raw data, decrease the number of variables, and reduce the number of zeroes in the raw data (Leoni et al., 2018). The uncertainties were calculated according to Vu et al. (2015). The total variables were calculated by summing all the bins (N10 – 800). PMF was conducted using different uncertainty input matrices and different C3 (Vu et al., 2015) to obtain the  $Q_{true}$  closest to  $Q_{expected}$ ; different modelling uncertainties and different numbers of factors were also applied. A C3 of 0.8 was chosen.

### 2.2.4.2 3D plots

~~The mass size distributions of nitrate, sulphate and organic matter are depicted in a colour-coded 3D plot showing episodes of high mass concentrations.~~

### 3. Results and discussions

#### 3.1 Campaign overview

The campaigns were characterized by prevailing westerly winds with average wind speeds of  $3.20 \pm 1.5 \text{ m s}^{-1}$  in summer and  $4.45 \pm 3.1 \text{ m s}^{-1}$  in winter (Fig. A2), average temperatures of  $18.5 \pm 4.7 \text{ }^{\circ}\text{C}$  in summer and  $1.4 \pm 3.9 \text{ }^{\circ}\text{C}$  in winter, and negligible precipitation. The average  $\text{PM}_{2.5}$  was  $10.9 \pm 5.9 \text{ } \mu\text{g m}^{-3}$  in summer and  $11.8 \pm 9.9 \text{ } \mu\text{g m}^{-3}$  in winter (2019 average annual  $\text{PM}_{2.5}$  concentration:  $10.1 \text{ } \mu\text{g m}^{-3}$ , CHMI, 2019a).

Based on the PNSD, in summer, particles in the size range of 25 – 80 nm (N25 – 50 and N50 – 80) were predominated, while whereas in winter, N80 – 150 were dominant (Table 1). Particles in the size range of 25 – 80 nm, also called referred to as the Aitken mode, are typical for rural background stations and originate from the ageing of particles generated during new particle formation (NPF) events (Costabile et al., 2009). Based on a 5-year study (2013 – 2017) evaluating PNSDs at NAOK, June and July were classified as the months with the highest NPF event frequencies (38 and 36% of days, respectively, Holubová Šmejkalová et al., 2021). The prevailing accumulation-mode particles in winter were presented in Schwarz et al., 2016, as well as in Žíková and Ždímal (2013). The average PNCs recorded during the two studied seasons were lower than the annual mean total concentration ( $6.6 \times 10^3 \text{ cm}^{-3}$ , Žíková and Ždímal, 2013).

Table 1. Average cumulative particle number concentrations ( $\text{cm}^{-3}$ ) measured by MPSS during the summer and winter campaigns.

| Size range (nm)   | Summer    | Winter    |
|-------------------|-----------|-----------|
| N10 – 25          | 979±1488  | 315±344   |
| N25 – 50          | 1726±1536 | 529±402   |
| N50 – 80          | 1112±715  | 478±492   |
| N80 – 150         | 907±472   | 606±654   |
| N150 – 300        | 508±191   | 437±368   |
| N300 – 800        | 51±41     | 86±76     |
| N10 – 800 (Total) | 4971±2794 | 2451±1749 |

#### 3.2 Volume and mass closure analysis with PNSD

For the mass closure analysis, the total mass concentrations measured by AMS (the sums of the organic, sulphate, nitrate, ammonium and chloride concentrations) were complemented by the eBC mass concentrations. The average  $\text{PM}_1$  concentrations for the summer and winter campaigns were  $8.58 \pm 3.70 \text{ } \mu\text{g m}^{-3}$  (filter-based 12-hour  $\text{PM}_1$   $10.10 \pm 6.44 \text{ } \mu\text{g m}^{-3}$ ) and  $10.08 \pm 8.04 \text{ } \mu\text{g m}^{-3}$  (filter-based 12-hour  $\text{PM}_1$   $11.05 \pm 7.22 \text{ } \mu\text{g m}^{-3}$ ), respectively. Since the PNSD (10 to 800-nm mobility diameter) was measured continuously in parallel with the eBC and NR- $\text{PM}_1$  mass, volume mass closure of the 10-min averages was performed. To do so, two approaches were utilized: i) converting the NR- $\text{PM}_1$  + eBC mass concentrations into volume concentrations using the composition-dependent density, and ii) converting the PNSDs into

mass concentrations using a constant density of  $1.5 \text{ g cm}^{-3}$ . Over the summer campaign, the NR-PM<sub>1</sub> + eBC volume and mass concentrations agreed well with the MPSS volume and mass concentrations in comparison to the winter campaign (Fig. 1). The seasonal effect on mass closure already reported by Poulain et al., 2020 using ACSM at rural Melpitz, as well as by Fröhlich et al., 2015 using ToF ACSM at Jungfraujoch could be explained by higher concentrations in larger size bins of the volume size distribution in winter compared to in summer (Fig. 2), since the AMS underestimates the particle mass concentrations for the larger size bins. This is due to the specific size cutting of each instrument and the transmission efficiency of the aerodynamic lens (Poulain et al., 2020). Moreover, the constant density is a limitation of the mass approach due to the density variability within the distinct episodes. Irregularities in the mass size distributions of nitrate, sulphate, and ammonium are discussed further in this paper.

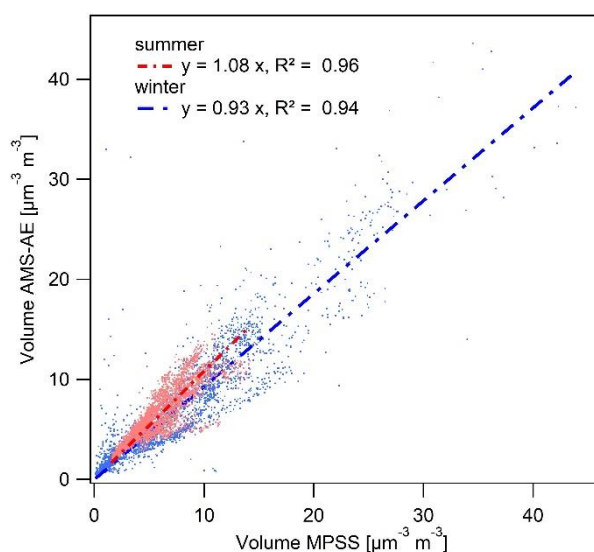


Fig. 1. Comparison between the AMS-AE and MPSS measurements during both campaigns: volume closure (left) and mass closure (right).

### 3.3 Concentration and origin of NR-PM<sub>1</sub>

The CE-corrected mass concentrations of NR-PM<sub>1</sub> species, calculated as functions of time during the two campaigns, are shown in Fig. A3 and the seasonal average concentrations are presented in Table 2. Organics dominated were dominant during both campaigns, followed by  $\text{SO}_4^{2-}$  in summer and  $\text{NO}_3^-$  in winter. The PM<sub>1</sub> IC results confirmed higher mean  $\text{SO}_4^{2-}$  concentrations in summer ( $\text{SO}_{4\text{IC}}^{2-} 1.63 \pm 0.84 \mu\text{g m}^{-3}$  and  $\text{NO}_{3\text{IC}}^- 0.23 \pm 0.18 \mu\text{g m}^{-3}$ ). However, the mean  $\text{NO}_3^-$  concentrations were slightly lower than the  $\text{SO}_4^{2-}$  concentrations in winter ( $\text{NO}_{3\text{IC}}^- 0.72 \pm 0.52 \mu\text{g m}^{-3}$  and  $\text{SO}_{4\text{IC}}^{2-} 0.78 \pm 0.58 \mu\text{g m}^{-3}$ ). The difference between the  $\text{NO}_3^-$  concentrations in NR-PM<sub>1</sub> and PM<sub>1</sub> for both seasons could be explained by the loss of ammonium nitrate from the filter due to its dissociation into its gaseous precursors. Good agreement was obtained between the summer average NR-PM<sub>1</sub>  $\text{NH}_4^+$  and PM<sub>1</sub>  $\text{NH}_4^+$  ( $0.80 \pm 0.37 \mu\text{g m}^{-3}$  vs  $0.70 \pm 0.36 \mu\text{g m}^{-3}$ ) in comparison to those obtained in winter ( $1.11 \pm 0.99 \mu\text{g m}^{-3}$  vs  $0.46 \pm 0.35 \mu\text{g m}^{-3}$ ). The seasonal variability in nitrate, which displayed higher concentrations in winter, was related to the thermal instability of ammonium nitrate (Seinfeld

and Pandis, 2006). A higher share of  $\text{Cl}^-$  along with eBC on NR-PM<sub>1</sub> in winter (3 % and 9%, respectively) indicates the influence of coal combustion used for domestic heating (CHMI, 2019b).

Overall, the average  $\text{SO}_4^{2-}$  concentration obtained in this study was lower than that measured at the Melpitz rural background site ( $2.44 \mu\text{g m}^{-3}$  in summer and  $1.66 \mu\text{g m}^{-3}$  in winter, Poulain et al., 2011) and lower than the values presented in previous studies by Schwarz et al. (2016) conducted at NAOK (PM<sub>2.5</sub> IC  $2.30 \mu\text{g m}^{-3}$  in summer and  $3.86 \mu\text{g m}^{-3}$  in winter) and by Kubelová et al. (2015) conducted in a Prague urban background site ( $2.0 \mu\text{g m}^{-3}$  in summer and  $4.4 \mu\text{g m}^{-3}$  in winter). The average summer  $\text{NO}_3^-$  concentration was comparable to those measured in Melpitz ( $0.66 \mu\text{g m}^{-3}$ ), NAOK (PM<sub>2.5</sub> IC  $0.55 \mu\text{g m}^{-3}$ ) and Prague ( $0.80 \mu\text{g m}^{-3}$ ); however, the winter average concentration was lower than those reported in all three studies (Melpitz:  $3.62 \mu\text{g m}^{-3}$ , NAOK:  $2.83 \mu\text{g m}^{-3}$ , Prague:  $5.40 \mu\text{g m}^{-3}$ ). The average organic concentration was lower in summer but higher in winter than compared to the values recorded in Melpitz ( $6.89 \mu\text{g m}^{-3}$  (51%) and  $2.08 \mu\text{g m}^{-3}$  (23%), respectively). The comparison of organic mass (OM) by AMS and OC using an OCEC field analyser is shown in Fig. A4. Turpin and Lim, 2001 recommended an OM/OC ratio of 2.1 for non-urban (aged) particles and of 1.6 for urban particles. In this study, the average OM/OC ratio was  $2.06 (\pm 0.68)$  in summer and  $1.51 (\pm 0.36)$  in winter. An average OM<sub>1</sub> and OC<sub>2.5</sub> of  $2.1 \pm 1.4$  was determined at the Hohenpeissenberg rural site in spring, referring to continental OA (Hock et al., 2002). The higher summer OM/OC ratio could be explained by the presence of more oxidized organic compounds, as the products of photochemical reactions increase the average organic molecular weight per carbon weight (Turpin and Lim, 2001). This result is consistent with the increasing OC/EC ratio observed during summer, when photochemical activity leads to larger secondary organic carbon formation (Mbengue et al., 2018, 2020). Another explanation could be the increased boundary layer height, which enables mixing from higher altitudes and therefore the entrainment of aged, and thus more oxidized, aerosols from long-range transport (Querol et al., 1998). On the other hand, the winter season is characterized by fresh emissions of hydrocarbons owing to the lowered boundary layer height in winter, which does not support the transport of oxidized pollutants within the mixing layer (Schwarz et al., 2008).

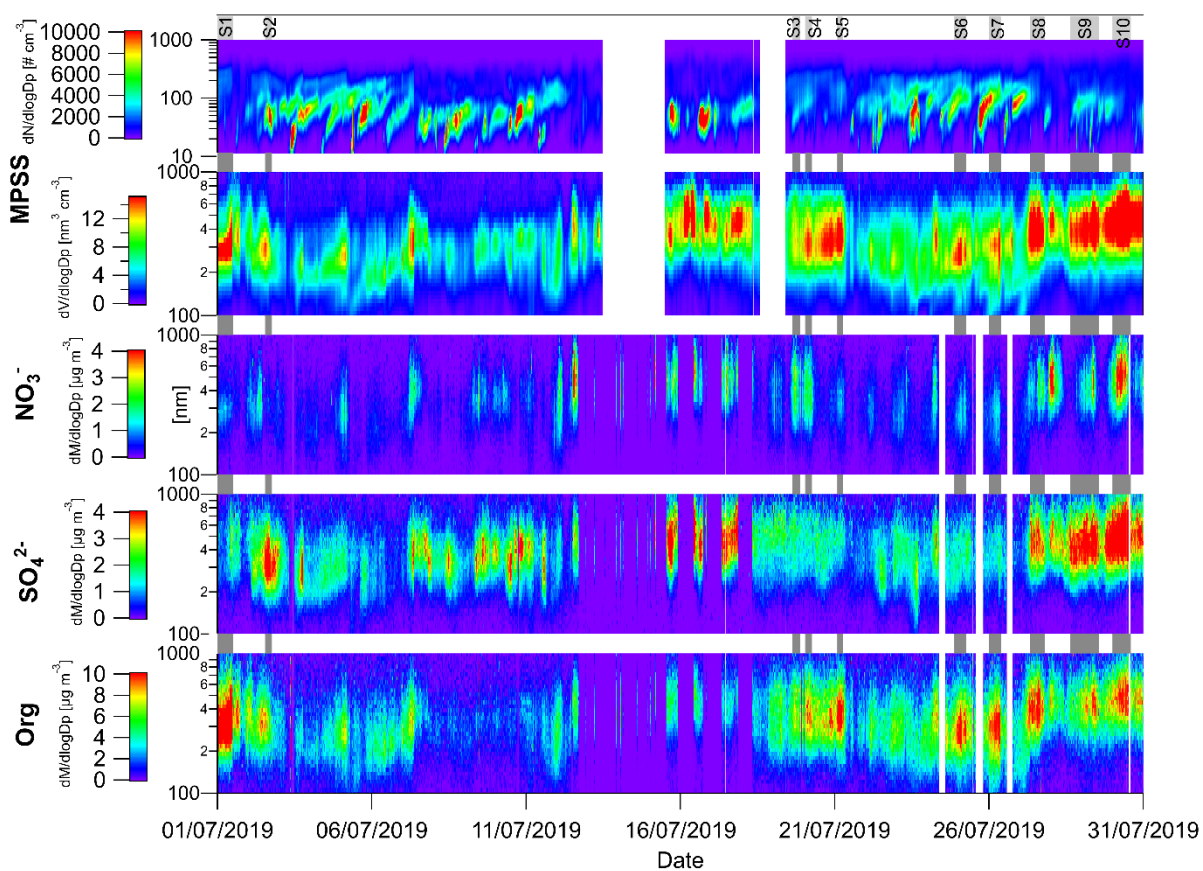
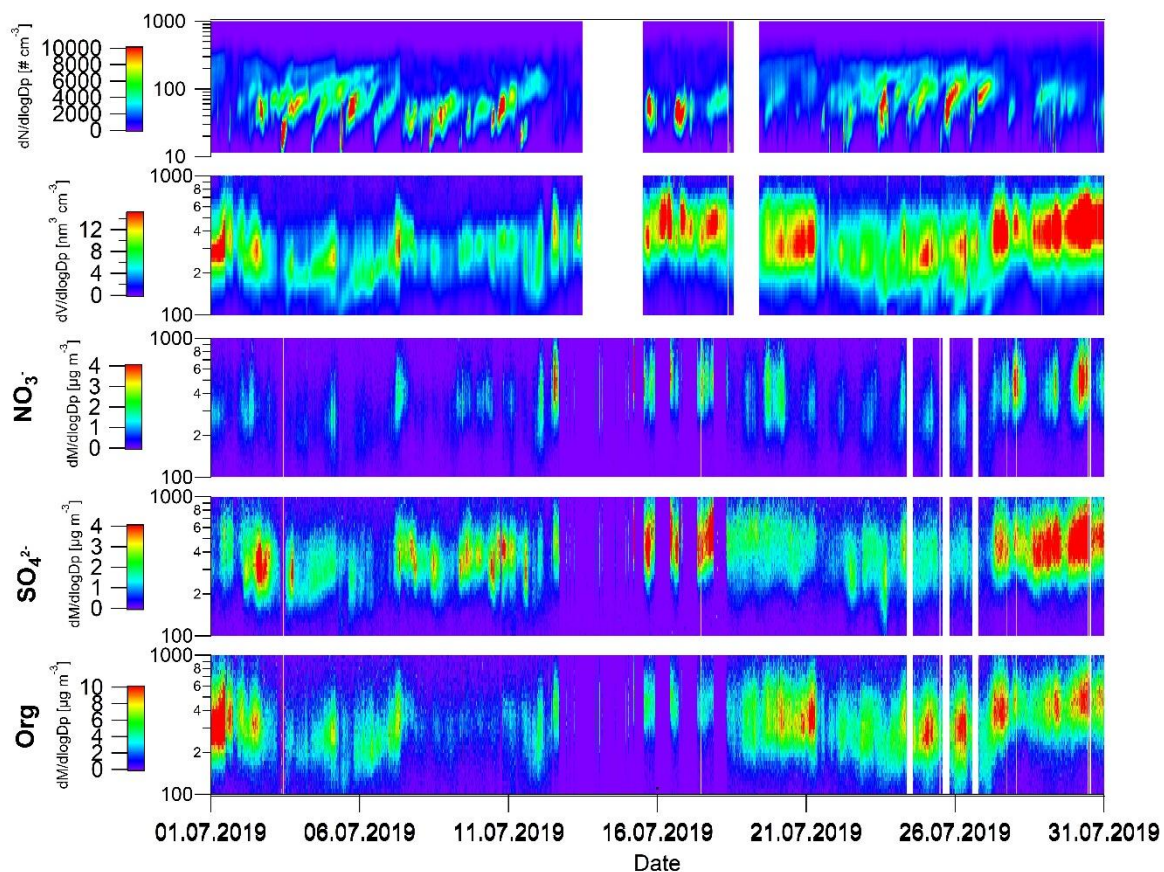
Table 2. Basic statistics of the NR-PM<sub>1</sub> and eBC concentrations (median, mean, standard deviation (SD) and average share of species in the total concentration) measured during summer and winter. The values were calculated from five-min-resolution CE-corrected data.

| Summer                              | Org    | $\text{SO}_4^{2-}$ | $\text{NO}_3^-$ | $\text{NH}_4^+$ | $\text{Cl}^-$ | eBC  |
|-------------------------------------|--------|--------------------|-----------------|-----------------|---------------|------|
| Median ( $\mu\text{g m}^{-3}$ )     | 4.32   | 1.53               | 0.57            | 0.75            | 0.06          | 0.36 |
| Mean ( $\mu\text{g m}^{-3}$ )       | 4.97   | 1.68               | 0.67            | 0.80            | 0.06          | 0.40 |
| SD                                  | 2.92   | 0.81               | 0.38            | 0.37            | 0.02          | 0.20 |
| Average share on NR-PM <sub>1</sub> | 568%   | 212%               | 98%             | 10%             | 1%            | 4%—  |
| Winter                              |        |                    |                 |                 |               |      |
| Median ( $\mu\text{g m}^{-3}$ )     | 3.35   | 0.98               | 1.67            | 0.93            | 0.16          | 0.84 |
| Mean ( $\mu\text{g m}^{-3}$ )       | 4.55   | 1.36               | 2.03            | 1.11            | 0.18          | 0.92 |
| SD                                  | 4.40   | 1.38               | 1.71            | 0.99            | 0.09          | 0.77 |
| Average share on NR-PM <sub>1</sub> | 4550 % | 134 %              | 202 %           | 104 %           | 3 %           | 9%—  |



355

356 Fig. 2 shows the variations in the particle number and volume and in the sulphate, nitrate and  
357 organic size distributions as function of time. In summer, several NPF episodes were recorded  
358 (Zíková and Ždímal, 2013; Holubová Šmejkalová et al., 2021); however, accumulation-mode  
359 particles were prominent in volume and species mass size distributions.



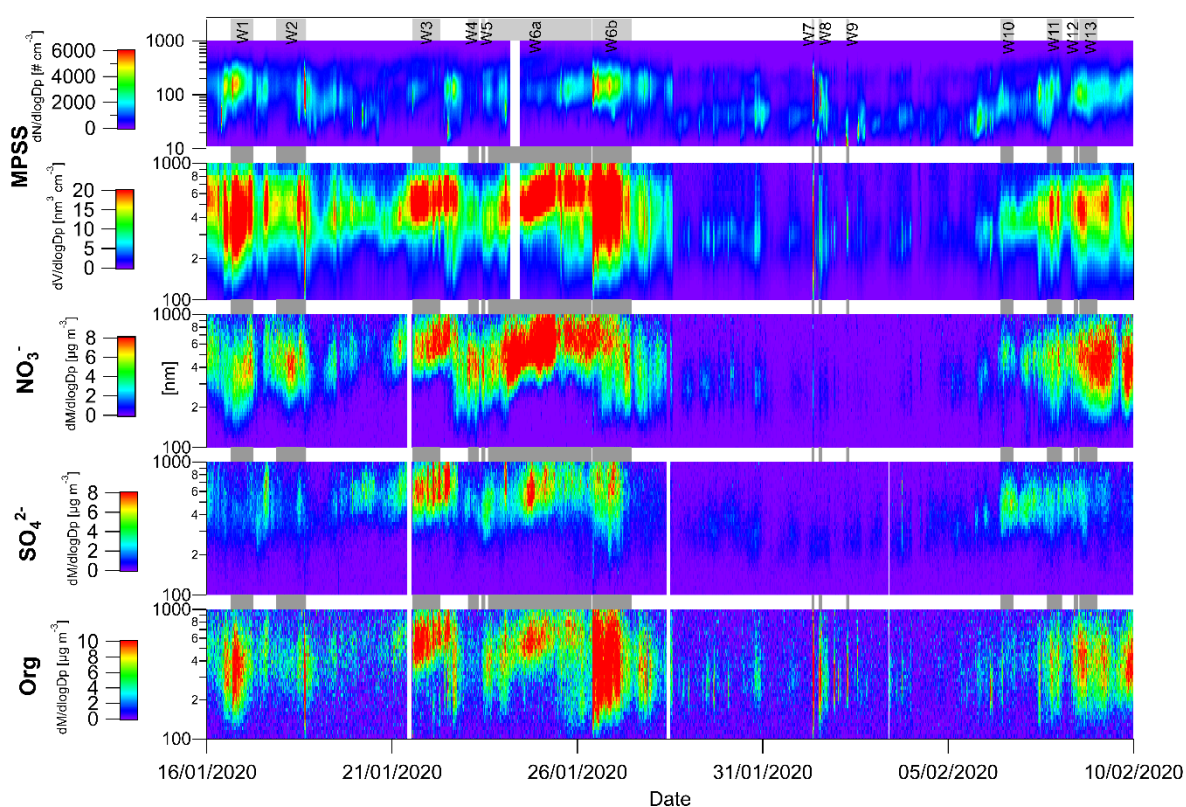
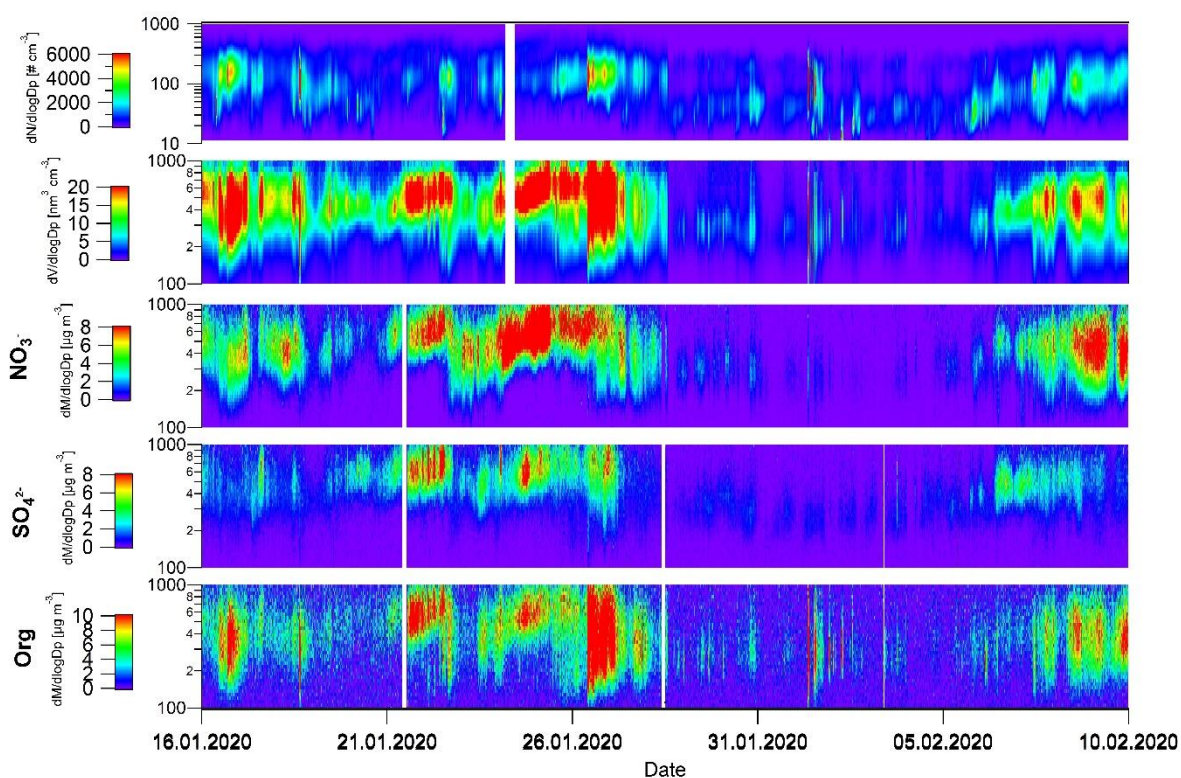


Fig. 2. Time series of particle number and volume concentrations obtained by MPSS ( $D_{va}$  recalculated from mobility diameter ~~using a density of  $1.50 \text{ g cm}^{-3}$~~ ) and mass size distributions of nitrate, sulphate and organics obtained by AMS in summer (top) and in winter (bottom) with marked episodes of higher mass concentrations.



The accumulation mode of  $SO_4^{2-}$  does not show a large amount of variation, indicating a regional origin. In contrast,  $NO_3^-$  shows diurnal variations in mass concentrations corresponding to the local photochemical formation of this species (Fig. A53). In winter, the accumulation mode dominated all distributions and was linked to regional and/or long-range transport (see 3.4 Size distribution of NR-PM<sub>1</sub>).

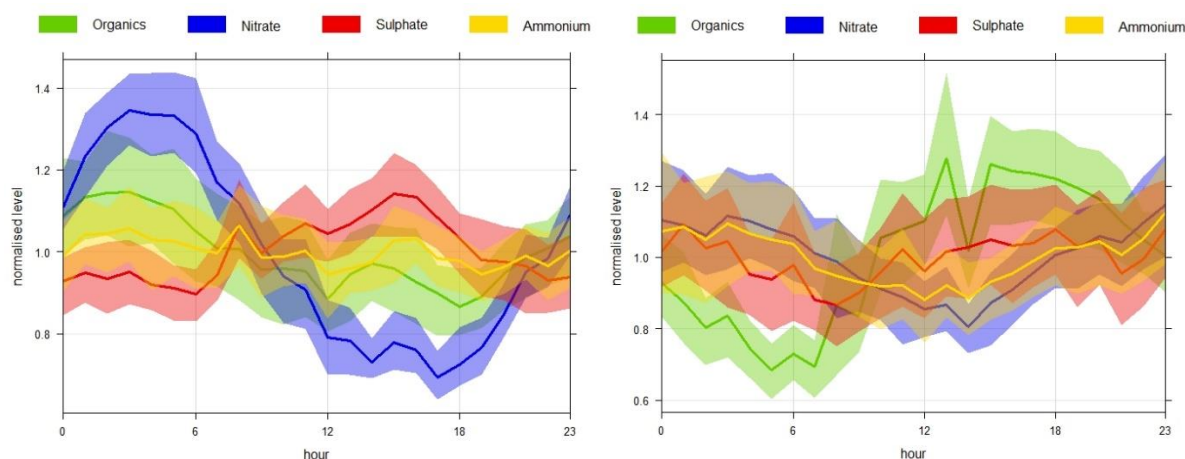


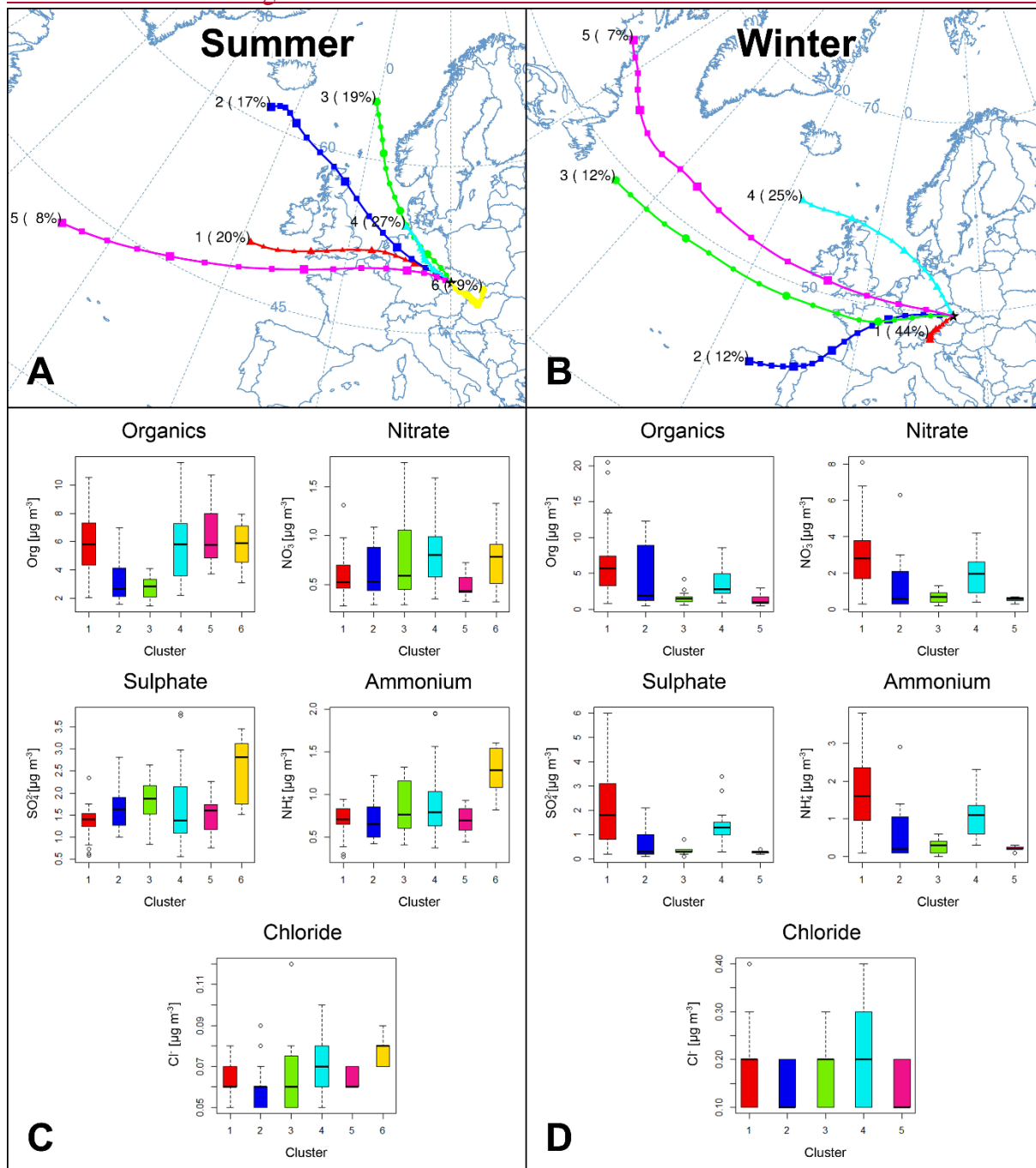
Fig. 3. Mean diurnal trends (time in UTC) of the NR-PM<sub>1</sub> species (95% confidence interval) in summer (left) and winter (right).

To determine the origin of NR-PM<sub>1</sub> species, back-trajectories describing their air mass origins were clustered using the HYSPLIT model into 6 and 5 clusters in summer and winter, respectively (Fig. 445.), and linked to the PM<sub>1</sub>, N10 – 800, organic, nitrate, sulphate, ammonium and chloride-eBC concentrations. A seasonal difference was observed in the air mass back-trajectories, with continental air masses prevailing in summer and marine air masses prevailing in winter.

In summer, clusters #1, 2 and 3 (fresh marine air masses from the NW, 56%) and cluster #4 (continental air masses from the W-NW, 27%) and cluster #3 (fresh marine air masses from the NW, 28%) were most frequent. Although aged continental air masses from the SE probably related to stable anticyclonic conditions (cluster #6) were rare (7%), they were connected with the highest concentrations of PM<sub>1</sub>, eBC and all NR-PM<sub>1</sub> species, especially  $SO_4^{2-}$ ,  $NH_4^+$  and  $Cl^-$ .  $NO_3^-$  was linked to fresh marine air masses (cluster #4, 7%), and Org was linked to continental air masses coming from the W-NW (#1 and #5, 29% and 19%, respectively) (Fig. 445.). The highest particle number concentrations (N10 – 800) were linked to fresh marine air masses (cluster #1, 2 and 3). There was statistically significant difference among all clusters at the 0.05 level (Kruskal-Wallis test).

In winter, slow continental air masses from the SW cluster #1 (44%) prevailed. The air masses remaining over Central Europe, likely under inversion conditions, were associated with the highest concentrations of PM<sub>1</sub>, eBC and all NR-PM<sub>1</sub> species, except  $Cl^-$  since there was no statistically significant difference among the clusters at the 0.05 level (Fig. 45.). The high pollution loads over Central Europe agree well with the high average mass concentrations of secondary species during periods when air masses are advected from Central Europe to Paris (Freney et al., 2011, Crippa et al., 2013; Freutel et al., 2013, Freney et al., 2014). N10 – 800 was linked mainly linked to marine clusters #1 and 5. There was statistically significant

401 difference among all clusters at the 0.05 level.



402



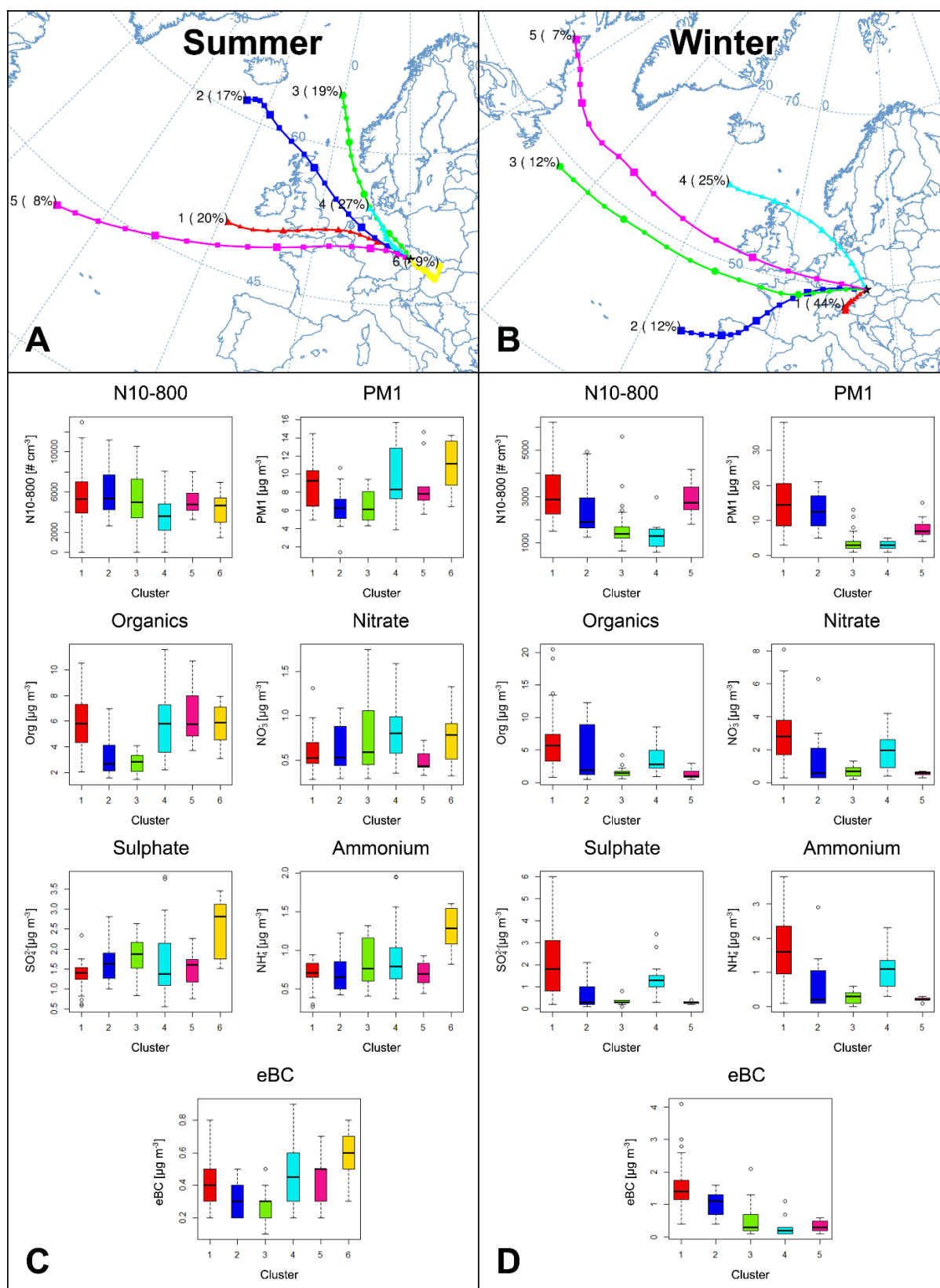


Fig. 445. Geographical locations of the means of the clusters observed in summer (A) and winter (B) along with boxplots of the  $PM_1$ ,  $N_{10-800}$ , organic, nitrate, sulphate, ammonium and  $eBC_{chloride}$  concentrations in individual clusters measured during the summer (C) and winter (D) campaigns. The boxes are colour coded as the clusters, the black horizontal line is the median, the boxes border the 25<sup>th</sup> and 75<sup>th</sup> percentiles and the whiskers represent 1.5 x IQR.

Based on the mass size distributions of the species (Fig. 2), ten summer (S1 – 10) and 13 winter (W1 – 13) high mass -concentration episodes were selected (Table A1). The organic mass dominated in summer; however, distinct episodes of high  $SO_4^{2-}$  concentrations (S2, S8, S9, S10) linked to continental air masses from the NW and S-SE were also recorded (Fig. A6A45). In winter, episodes of dominant  $SO_4^{2-}$  (W10) and  $NO_3^-$  (W1, W2, W4, W5, W6) concentrations were observed. W10 was influenced by fresh marine air masses reaching NAOK over the UK, Benelux and Germany. The episodes of high  $NO_3^-$  concentrations were mainly linked mainly to continental air masses (from the NW-SW, Fig. A7A6) from northern France, Benelux, central Germany and northern Italy. These regions were traced as hotspots of high particulate nitrate concentrations related to intense agricultural activities under anticyclonic conditions in late-winter and early-spring (Waked et al., 2014; Petit et al., 2017, 2019; Favez et al., 2021).

In summer, the highest Org concentrations ( $14.58 \mu\text{g m}^{-3}$ ) together with the lowest  $SO_4^{2-}$  and  $NH_4^+$  ( $1.24 \mu\text{g m}^{-3}$  and  $0.91 \mu\text{g m}^{-3}$ ) concentrations were observed during the S1 night-morning episode linked to western continental air masses (Table A1 and Fig. A3). S10 represents the night-morning-early afternoon episode of the highest concentrations of  $SO_4^{2-}$ ,  $NO_3^-$  and  $NH_4^+$  ( $6.14 \mu\text{g m}^{-3}$ ,  $3.37 \mu\text{g m}^{-3}$ , and  $2.98 \mu\text{g m}^{-3}$ , respectively) resulting from mixed continental air masses (NW-S) that were potentially influenced by emissions from coal power plants situated in North Bohemia.

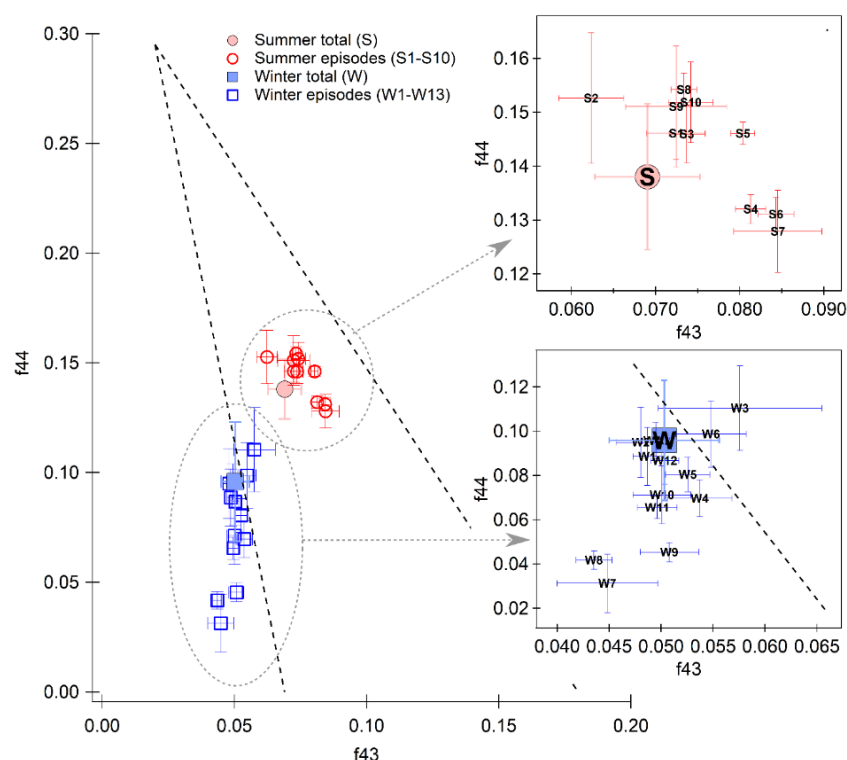


Fig. 354. Comparison of organic fragments  $f_{44}$  and  $f_{43}$  for the whole summer and winter campaigns (full markers) and for specific episodes (empty markers). Bars represent the standard deviation and the triangular space area typical for ambient OOAs (Ng et al., 2010).

The highest concentrations of Org ( $15.63 \mu\text{g m}^{-3}$ ) as well as low concentrations of  $SO_4^{2-}$ ,  $NO_3^-$  and  $NH_4^+$  ( $0.74 \mu\text{g m}^{-3}$ ,  $0.93 \mu\text{g m}^{-3}$  and  $0.96 \mu\text{g m}^{-3}$ , respectively) measured in winter during

W7 were influenced by maritime air masses crossing France and Germany before reaching the NAOK (Fig. A7A6). Nevertheless, a one-day inversion preceded this episode (Fig. A3), characterized by less oxidized OA (Fig. 354) and ~~f<sub>44</sub>f<sub>60</sub> trending towards f<sub>60</sub>~~ (Fig. A8A7). In contrast, the highest winter  $SO_4^{2-}$  and  $NH_4^+$  concentrations ( $7.13 \mu\text{g m}^{-3}$  and  $7.90 \mu\text{g m}^{-3}$ , respectively) measured in the W3 episode and the highest  $NO_3^-$  concentrations ( $10.66 \mu\text{g m}^{-3}$ ) measured in the W6a episode were characterized by slightly below-freezing temperatures (average temperature  $-2.4^\circ\text{C} \pm 1.3^\circ\text{C}$ ), which probably arose due to inversion conditions in Central Europe. The conditions prevailing during the W6a episode, in combination with ammonia due to the agricultural activities, including the spreading of fertilizers, probably induce increases of particulate nitrate and ammonium concentrations similarly as reported by Favez et al., 2021 for Northern France.

Organic fragments  $f_{44}$  and  $f_{43}$  (ratios of organics in  $m/z$  44 and  $m/z$  43 to total organics) can serve as a proxy of aerosol oxidation and its aging, respectively (Ng et al., 2010). In simplified form, more oxidized aerosols have higher  $f_{44}$  and lower  $f_{43}$  while less oxidized and more volatile aerosols have the opposite  $f_{44}$  vs  $f_{43}$  relationship. These oxidation properties of organic aerosols are well defined by the triangular region defined by Ng et al. (2010). This triangular area is shown in Fig. 54 together with the evolution of  $f_{44}$  and  $f_{43}$  fragments during both campaigns. In general, it shows that Organic aerosol ageing was examined on the  $f_{44}$  and  $f_{43}$  fragments (Fig. 3). Winter aerosols were less oxidized than summer aerosols. This results along with the organics diurnal trends of late evening maxima (Fig. 3) and polar plots (Fig. A5) pointing to the importance of local sources during the cold part of the year. The importance of local fossil/fossil fuels combustion for residential heating as a source of fresh OA/ hydrogen-like OA in winter is presented in a study by Chen et al., 2021 (under review). In summer, the oxidation rate of organic aerosols within the episodes does not differ greatly, and most of the episodes revealed more oxidized organic aerosols (MO-OOAs) or less volatile organic aerosols (LV-OOAs) (e.g. Jimenez et al. (-2009); Crippa et al. (-2013)-ete). Within the summer campaign, the most oxidized aerosols were detected during the afternoon episode S2 (Fig. 35), at which time the highest global radiation was also measured (Table A1.). In contrast, S4, S6 and S7 represent night-time and early morning episodes, and S5 represents a night-time and morning episode, and thus less oxidized aerosols (Fig. 35). In winter, the difference between the episodes is more obvious, mainly due to the higher variability in the local sources that influence the receptor site. The W7, W8 and W9 (Fig. 35) episodes are exceptions; these episodes were linked to clean fresh marine air masses that cause prevailing influence of local, fresh, and less oxidized aerosol (Fig. A7A6.).

The organic fragment  $f_{60}$  fragment was used as a biomass-burning (BB) marker. If ambient aerosols are characterized by an  $f_{60}$  higher than 0.003, they are considered to be influenced by BB emissions (Cubison et al., 2011). During both campaigns, the average  $f_{60}$  was 0.003, in contrast to the presence of levoglucosan in the  $PM_{10}$  samples during both seasons (summer average  $0.02 \pm 0.02 \mu\text{g m}^{-3}$  and winter average  $0.18 \pm 0.20 \mu\text{g m}^{-3}$ ). Levoglucosan concentrations point to BB influence, which was similarly discussed in previous studies conducted at NAOK by Schwarz et al. (2016) and Mbengue et al. (2020). Additionally, a comparison of fragments  $f_{44}$  and  $f_{60}$  enabled us to assess the presence of fresh or aged organic aerosols emitted by BB (e.g., Milic et al., 2017), revealing that aged organic aerosols from BB influenced the site during both seasons, especially in winter (Fig. A9A78). The comparison of organic fragments  $f_{44}$  and  $f_{60}$  determined at the rural and urban background sites shows a difference in the ageing of BB emissions, with the presence of fresh organic aerosols at the urban site and aged organic aerosols at the rural site in winter (Fig. A9A8).

483

### 484 3.4 Size distribution of NR-PM<sub>1</sub>

485 The average mass size distributions of the main NR-PM<sub>1</sub> species (except chloride) during the  
 486 entire summer and winter campaign are presented in Table 3. To determine the mode diameters  
 487 and the widths of the size distributions, the mass distributions were fitted with log-normal  
 488 modes using the Igor MultiPeak Package as follows:

$$489 \quad y = M \exp \left[ - \left( \frac{\ln(x/x_0)}{\text{width}} \right)^2 \right], \quad (3)$$

490 where  $M$  is the amplitude,  $x_0$  is the peak position in nm, and  $\text{width}$  denotes the peak width. For  
 491 each season, the mean spectra were fitted separately with one peak, and fitting was also  
 492 performed for episodes S1-10 and W1-13. ~~Due to the long duration of episode W6, the episode~~  
 493 ~~was split into two sections: W6a (67 hours) and W6b (25.5 hours).~~

494 The accumulation mode dominated the average mass size distributions during both campaigns,  
 495 with larger particles of all species observed in winter (Table 3). Shifts towards larger  $SO_4^{2-}$ ,  
 496  $NO_3^-$  and  $NH_4^+$  particles in winter compared to summer were also observed in a previous study  
 497 by Schwarz et al. (2012) that determined urban aerosol chemical compositions and size  
 498 distributions using a 7-stage impactor with an upstream diffusional aerosol drier. The  $SO_4^{2-}$   
 499 particles were significantly larger than the  $NO_3^-$  particles during both measurement campaigns  
 500 except for ~~during those collected during~~ two episodes (W7 and W9) with regional transport  
 501 (Table A13). An accumulation mode of  $SO_4^{2-}$  with regional origin was even detected during a  
 502 Mexico City Metropolitan Area field study by Salcedo et al. (2006). Dall'Osto et al. (2009) also  
 503 observed two nitrate particle types at an urban background site, both of which were internally  
 504 mixed with sulphate, ammonium and carbon: the locally produced particles were smaller than  
 505 300 nm, ~~and while~~ the regional particles peaked at 600 nm. In a study by Schwarz et al. (2012)  
 506 at an urban site in Prague, two types of  $SO_4^{2-}$  particles were determined.  $SO_4^{2-}$  particles in sea-  
 507 influenced aerosol samples showed maxima between 210 and 330 nm (condensation growth)  
 508 for both seasons, and  $SO_4^{2-}$  particles in continental-influenced samples showed maxima  
 509 between 500 and 890 nm in winter and between 330 and 500 nm in summer (droplet-phase  
 510 growth).  $NO_3^-$  particles with maxima between 330 nm and ~500 nm were observed under  
 511 maritime and continental air masses during both seasons. Freutel et al., 2013 observed a single  
 512 mode of NR-PM<sub>1</sub> species of approximately 300 nm under marine air masses as well as a shift  
 513 of the accumulation mode to a larger size (approximately 400 nm) during a summer campaign  
 514 in the Paris region due to aerosol particle ageing of continental air masses from Central Europe.  
 515 During a summer measurement campaign in New York, the average mass distributions of  $NO_3^-$ ,  
 516  $SO_4^{2-}$  and  $NH_4^+$  were monomodal, with mode diameters of 440 nm, 450 nm and 400 nm,  
 517 respectively, and the average Org mass distribution was bimodal, with mode diameters of 80  
 518 nm and 360 nm (Drewnick et al., 2004). A study by Freney et al. (2011) conducted during three  
 519 seasons at the Puy-de-Dôme research station presented a major accumulation mode of NR-PM<sub>1</sub>  
 520 species peaking at 600 nm, indicating aged aerosol particles.

521 Table 3. Average-Mode diameter of masssize distributions of species measured by AMS ( $D_p$   
 522 corresponds to the vacuum aerodynamic diameter ( $D_{va}$ )) for the summer (left) and winter (right)  
 523 campaigns.

---

Org  $SO_4^{2-}$   $NO_3^-$   $NH_4^+$

|                      |     |     |     |     |
|----------------------|-----|-----|-----|-----|
| Summer $D_{va}$ (nm) | 334 | 377 | 401 | 497 |
| Winter $D_{va}$ (nm) | 413 | 501 | 547 | 517 |

524

525 In summer, the smallest mode diameters of Org (279 nm) and  $NO_3^-$  (253 nm) were observed  
526 during the S7 episode, while for  $SO_4^{2-}$  and  $NH_4^+$  (325 nm and 335 nm, respectively), they were  
527 influenced by continental air masses of regional origin during the S2 episode (from the N-NE-  
528 E, Fig. A6A5). In contrast, the largest mode diameters (Org: 466 nm,  $NO_3^-$ : 491 nm,  $SO_4^{2-}$ :  
529 494 nm and  $NH_4^+$ : 478 nm) were recorded during the S10 episode by continental long-range  
530 transport from the W-NW (Fig. A6A5). The smallest mode diameters of all species (Org: 295  
531 nm,  $NO_3^-$ : 240 nm,  $SO_4^{2-}$ : 242 nm and  $NH_4^+$ : 365 nm) in winter (W8) were linked to fresh marine  
532 air masses, and the largest winter diameters (Org: 563 nm,  $NO_3^-$ : 609 nm,  $SO_4^{2-}$ : 636 nm and  
533  $NH_4^+$ : 607 nm, W3) were linked to the regional and long-range transport of air masses of  
534 continental origin and were ~~also probably likely~~ influenced by inversion conditions (Fig. A7A6).  
535 The aging of aerosol particles is often connected with particle growth similarly as with  
536 oxidation of organic mass. Comparison of fragment  $f_{44}$  and mode diameter fully confirmed the  
537 ideas. Additionally, as expected, the Org particle size showed growth, and the increasing mode  
538 diameter was more significant in the winter season, with the ageing of aerosols resulting in  
539 oxygenated organic aerosols (Fig. 56). In both seasons, the correlation of the linear fit between  
540 Org size and  $f_{44}$  ~~is~~ was significant (p-value < 0.001). However, the data presented here ~~does~~ not  
541 allow us to extend this size range due to both instrumental (C-ToF-AMS particle size range is  
542 ca from 50 – 800 nm) and data characterization reasons, as we did not observe a major mode  
543 of organics at sizes below 200 nm.

544 In general, however, Fig. 6 suggests that the larger the particles with the organic contribution,  
545 the more oxidised they are due to its longer residence time in the atmosphere. The milder slope  
546 of the line for the summer dataset (Fig. 6) indicates that oxidation is still occurring on the  
547 particles, but appears to be approaching ~~some~~ an oxidation limit with growing particle size. In  
548 the case of winter, the steeper slope of the line and lower  $f_{44}$  values for smaller particles suggest  
549 that the ~~change of oxidation state with particle size~~ level of oxidation is relatively more intense  
550 than in summer (Fig. 6). However, even so, under the given winter conditions (e.g., lower  
551 photochemical oxidation in winter than in summer), the degree of oxidation of organic aerosols  
552 does not reach the same level as in summer.



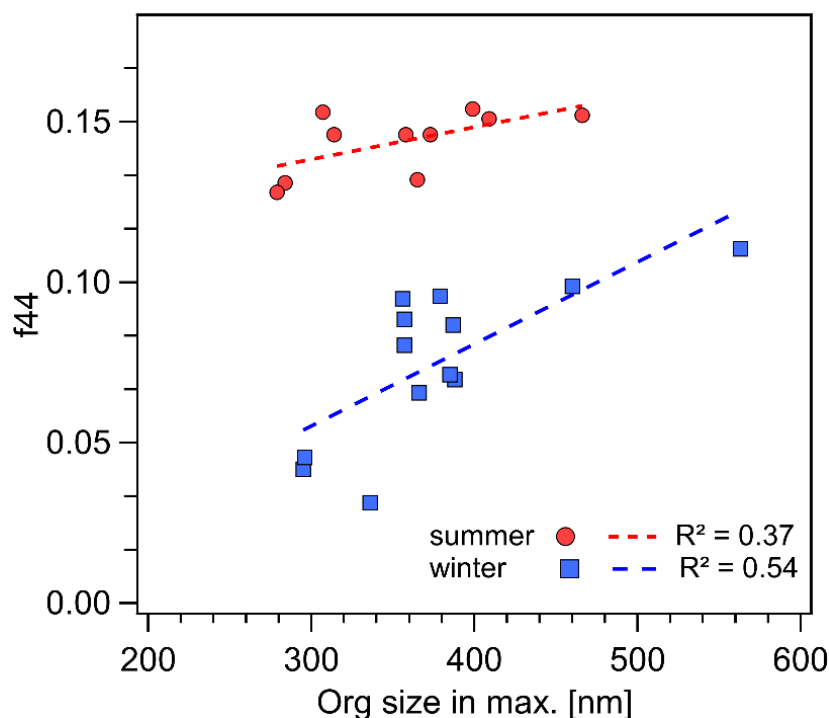


Fig. 56. Relationship between the organic fragment  $f_{44}$  and the size of the organic fraction during episodes of high NR-PM<sub>1</sub> species mass concentrations in both seasons.

### 3.5 Particle ~~effective~~ density and shape factor

The particle ~~effective~~ density and shape factors ~~was~~ were calculated for each episode of high ~~particle numbers and mass concentrations. The episodes were determined as follows: i) PMF application to PNSDs and ii) depiction of mass size distributions of NR-PM<sub>1</sub> species in a 3D plot (Fig. 2).~~

~~The PMF model was run several times until the most physically meaningful results and the best diagnostics were obtained. The two-sided size bins containing variables (9.7 nm, 11.5 nm, 557.2 nm and 733.6 nm; midpoint of the size bins) were set as weak along with the total variables (N10—800). The model was run with different factor numbers (3—8). The most stable solution was found when 6 factors in summer and 5 factors in winter were considered (Fig. A10A9). With all runs converged, the scaled residuals were normally distributed, any unmapped factors were detected with bootstrap error estimations. No swaps were observed with the displacement error analysis, indicating that the solution was stable (Table A2). The non-normalized PNSD ( $\text{N cm}^{-3}$ ) was analysed using the model.~~

#### 3.5.1 Episodes of high particle number concentrations

~~One high-particle-contribution episode occurred in summer, and eight short episodes occurred in winter (W1<sub>MPSS</sub>, factor 3 of 5 and W2<sub>MPSS</sub>—W8<sub>MPSS</sub>, factor 1 of 5; the durations ranged from 25 to 95 minutes). No NR-PM<sub>1</sub> data were available for effective density calculations during the summer period (3<sup>rd</sup> July from 9:20 to 10:05). The effective density ranged between 1.40 and 1.85  $\text{g cm}^{-3}$  (Table 4). During W1<sub>MPSS</sub>, accumulation mode particles dominated (F3, mode diameter  $\sim$  429 nm, Fig. A10A9) with an effective density of 1.85  $\text{g cm}^{-3}$ . A density of 1.85  $\text{g$~~

$\text{cm}^{-3}$  corresponds to black carbon (Martins et al., 1998), and a density of  $2.0 \text{ g cm}^{-3}$  relates to aged biomass burning particles (Moffet et al., 2008). The remaining episodes (W2<sub>MPSS</sub>—W8<sub>MPSS</sub>) were linked mainly to particles of the Aitken mode (F1, mode diameter  $\sim 32 \text{ nm}$ , Fig. A10A9) with effective densities ranging from  $1.40$  to  $1.60 \text{ g cm}^{-3}$ . Rissler et al. (2014) observed the dominance of particles with effective density  $\sim 1.4 \text{ g cm}^{-3}$  at a rural background site (Vavihill, Sweden) during the winter months, and Qiao et al. (2018) reported a decrease in particle effective densities ranging from  $1.43$  to  $1.55 \text{ g cm}^{-3}$  at rural sites (Changping, China) with increasing particle sizes.

Table 4. Particle effective densities ( $\text{g cm}^{-3}$ ) calculated during episodes of high particle contributions to N10—800 using MPSS data:

| Episode MPSS | W1   | W2   | W3   | W4   | W5   | W6   | W7   | W8   |
|--------------|------|------|------|------|------|------|------|------|
| Density      | 1.85 | 1.45 | 1.50 | 1.55 | 1.45 | 1.55 | 1.40 | 1.60 |
| # of spectra | 13   | 8    | 8    | 19   | 7    | 5    | 8    | 8    |

### 3.5.2 Episodes of high mass concentrations

The densities ( $\rho_{\text{eff}}$ ) calculated based on the particle mass size distributions using Eq. (1) corresponding to the episodes discussed in section 3.4 (Size distribution of NR-PM<sub>1</sub>) and summarised in Table A1 ranged from  $1.40 - 1.60 \text{ g cm}^{-3}$  in summer and from  $1.30 - 1.75 \text{ g cm}^{-3}$  in winter (Table 45, Fig. A11A940 and Fig. A12A1101). In comparison, the densities calculated using Eq. (2) were lower in both seasons, ranging ranged from  $1.30$  to  $1.40 \text{ g cm}^{-3}$  in summer (with a seasonal average of  $1.34 \pm 0.28 \text{ g cm}^{-3}$ ) and from  $1.30$  to  $1.50 \text{ g cm}^{-3}$  in winter (with a seasonal average of  $1.44 \pm 0.16 \text{ g cm}^{-3}$ ) (Table 45). The average summer density ( $\rho_m$ ) did not show a diurnal trend compared to the winter density (Fig. A137), followed by a diurnal trend (inverse dependence) observed for organics (Fig. A53). The summer diurnal variation in the concentrations of organics was flatter than that in winter and was not sufficient to significantly affect the diurnal density trend. In summer, we observed the most significant diurnal trend for nitrate, but yet the absolute concentrations of nitrate were low, and therefore this variation therefore did not significantly affect the summer diurnal density trend (Fig. A53).

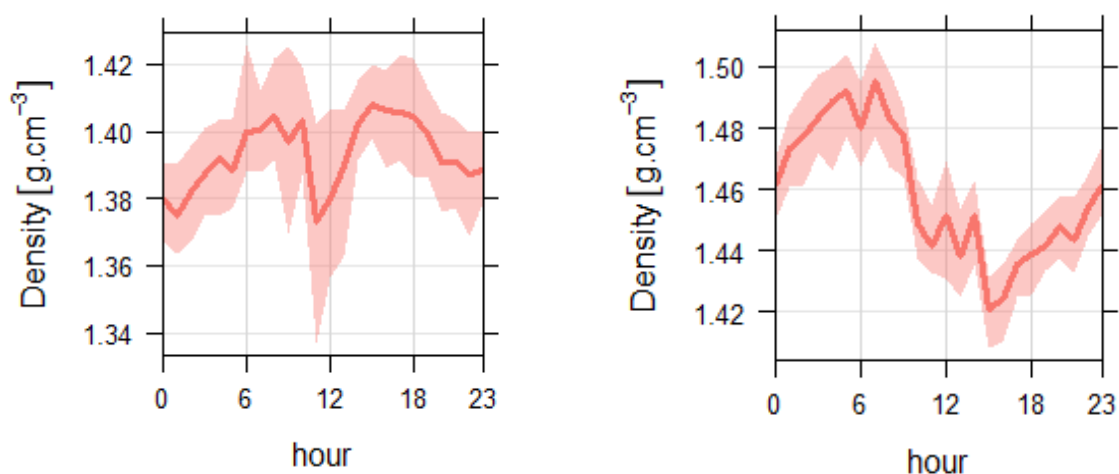


Fig. 7. Diurnal trends of average ~~effective particle density~~  $\rho_m$  calculated based on Eq. (2) in the main text from Salcedo et al., 2006 in summer (left) and winter (right).

In summer, ~~with a~~ where there was a higher ratio of ammonium sulphate, the density increased. In winter, the density was influenced by the inorganic content (ammonium nitrate and sulphate). In both seasons, the density increased with a decrease in the organic ratio ~~and vice versa~~. This relation evidently arises from the parameters in Eq. (2) (Fig. A148). The largest uncertainty in the PM density calculations performed using Eq. (2) is linked to the density of organics, which was set to  $1.2 \text{ g cm}^{-3}$ . The density applied for the organic fraction refers to the urban and urban background stations (Turpin and Lim, 2001), and the organics density of a rural background site is expected to be higher than that of an urban site due to organic aerosol ageing. However, a density of  $1.2 \text{ g cm}^{-3}$  was also utilized in a study conducted by Freney et al. (2011) at a mid-altitude Puy-de-Dôme site and in a study conducted by Poulain et al. (2020) at a rural background site in Melpitz. To be able to compare our results with above mentioned studies, we also used density of  $1.2 \text{ g cm}^{-3}$  for organics in Eq. (2). Therefore, as the mass fraction of organics in the aerosols increased, the density calculated using Eq. (2) converged to a value of  $1.2 \text{ g cm}^{-3}$  (Fig. 8). The use of higher density value for Org in Eq. (2) (e.g.,  $1.3$  and  $1.4 \text{ g cm}^{-3}$ ) affects the overall density value, thus so that the  $\rho_m$  is more in agreement with  $\rho_{\text{eff}}$ . Increasing value of the Org density in Eq. (2) also flatten the diurnal trend in winter, but it still holds significant diurnal variations (Fig. A11).

Values of Jayne shape factor (S) and the inferred dynamic shape factor ( $\chi$ ) for summer and winter episodes of high mass concentrations are presented in the Table 4. In summer the dynamic shape factor was almost constant ( $1.02 - 1.09$ ) and shape of the particle nearly spherical as a sphere  $\chi = 1$  (Hinds, 1999). In winter dynamic shape factor ranged from  $0.96$  to  $1.15$  ~~implies~~implying particles of nearly spherical shape and/or as compact agglomerates (DeCarlo et al., 2004; Zelenyuk et al., 2006). There was a slight decrease in dynamic shape factor ( $\chi$ ) with particle size (Fig. 9, statistically significant at the  $0.05$  level for winter). In comparison ~~in~~with the laboratory studies, the dynamic shape factor increased with particle mobility diameter or remained ~~s~~constant (Jimenez et al., 2003b, c; Slowik et al., 2004; Park et al., 2004; Zelenyuk et al., 2006). Additionally, in the study by Zelenyuk et al., 2006 the produced organic particles were found to be nearly spherical and the data suggested that an addition of organics to ammonium sulphate particles lowers their dynamic shape factor.

Table 45. Particle ~~effective~~ densities ( $\text{g cm}^{-3}$ ) and shape factors calculated during episodes of high mass concentrations using AMS data in summer (a) and winter (b).

a)

| Episode                         | S1   | S2   | S3   | S4   | S5   | S6   | S7   | S8   | S9   | S10  |
|---------------------------------|------|------|------|------|------|------|------|------|------|------|
| AMS                             |      |      |      |      |      |      |      |      |      |      |
| Density ( $\rho_{\text{eff}}$ ) | 1.45 | 1.60 | 1.50 | 1.55 | 1.40 | 1.45 | 1.45 | 1.45 | 1.45 | 1.50 |
| Density ( $\rho_m$ )            | 1.30 | 1.40 | 1.40 | 1.40 | 1.30 | 1.30 | 1.30 | 1.35 | 1.40 | 1.40 |
| Jayne shape factor (S)          | 1.12 | 1.14 | 1.07 | 1.11 | 1.08 | 1.12 | 1.12 | 1.07 | 1.04 | 1.07 |
| Dynamic shape factor ( $\chi$ ) | 1.08 | 1.09 | 1.05 | 1.07 | 1.05 | 1.08 | 1.08 | 1.05 | 1.02 | 1.05 |
| # of spectra                    | 145  | 61   | 73   | 61   | 49   | 109  | 109  | 133  | 265  | 169  |

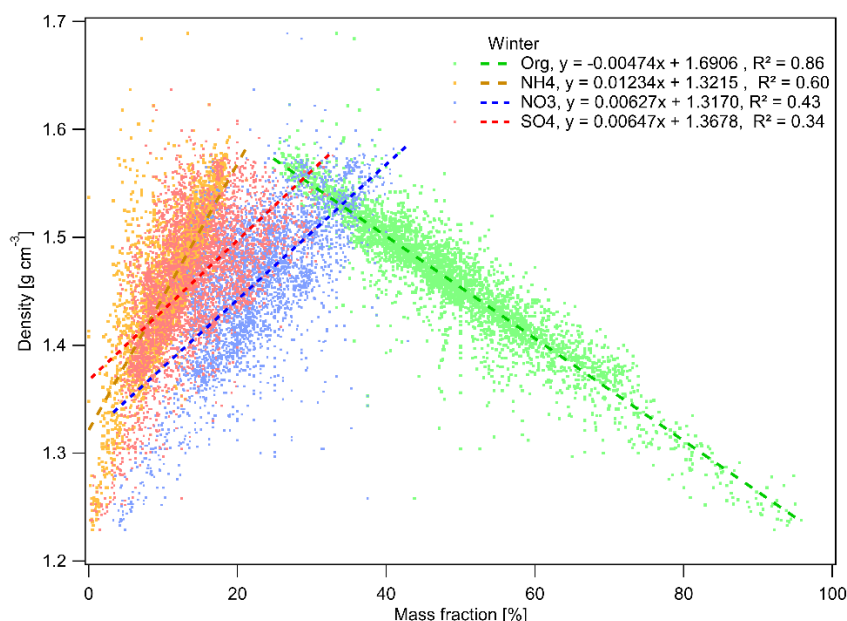
b)

| Episode<br>AMS                               | W1          | W2          | W3          | W4          | W5          | W6a         | W6b         |
|--|-------------|-------------|-------------|-------------|-------------|-------------|-------------|
| Density ( $\rho_{\text{eff}}$ ) <sup>*</sup> | 1.40        | 1.40        | 1.70        | 1.60        | 1.70        | 1.6         | 1.55        |
| Density ( $\rho_m$ )                         | 1.40        | 1.50        | 1.50        | 1.50        | 1.50        | 1.50        | 1.40        |
| Jayne shape factor (S)                       | <u>1.00</u> | <u>0.93</u> | <u>1.13</u> | <u>1.07</u> | <u>1.13</u> | <u>1.07</u> | <u>1.11</u> |
| Shape factor ( $\chi$ )                      | <u>1.00</u> | <u>0.96</u> | <u>1.09</u> | <u>1.04</u> | <u>1.09</u> | <u>1.04</u> | <u>1.07</u> |
| # of spectra                                 | 175         | 229         | 337         | 85          | 25          | 805         | 307         |
| Episode<br>AMS                               | W7          | W8          | W9          | W10         | W11         | W12         | W13         |
| Density ( $\rho_{\text{eff}}$ )              | <u>1.55</u> | <u>1.60</u> | <u>1.45</u> | <u>1.75</u> | <u>1.50</u> | <u>1.60</u> | <u>1.55</u> |
| Density ( $\rho_m$ )                         | <u>1.30</u> | <u>1.30</u> | <u>1.30</u> | <u>1.50</u> | <u>1.40</u> | <u>1.40</u> | <u>1.40</u> |
| Jayne shape factor (S)                       | <u>1.19</u> | <u>1.23</u> | <u>1.12</u> | <u>1.17</u> | <u>1.07</u> | <u>1.14</u> | <u>1.11</u> |
| Dynamic shape factor ( $\chi$ )              | <u>1.12</u> | <u>1.15</u> | <u>1.08</u> | <u>1.11</u> | <u>1.05</u> | <u>1.09</u> | <u>1.07</u> |
| # of spectra                                 | <u>19</u>   | <u>25</u>   | <u>19</u>   | <u>97</u>   | <u>115</u>  | <u>31</u>   | <u>139</u>  |

\*. Density calculated using Eq. 1.

\*\*. Density calculated using Eq. 2 (Salcedo et al., 2006).

The differences between the densities obtained using the two approaches (spectra fitting—Eq. 1 versus chemical equation—Eq. 2.), ranging from 2–12% in summer and 7–19% in winter, indicate the presence of different compounds of lower or higher densities that are not taken into consideration by the effective density calculations, as well as the lower density used for organics in Eq. (2), the physical characteristics of the particles, such as the particle size, porosity and non-compactness, and calculation uncertainties that are primarily related to the single CE correction used for the whole data set. The smaller differences between the two approaches obtained in summer indicate aerosol particles composed mainly of NR-PM<sub>1</sub> species along with eBC. In winter, the differences were larger, and both negative (compounds with lower densities and/or particle physical characteristics) and positive (compounds with higher densities) differences were obtained. However, the larger differences in winter could be strongly influenced by the considerable CE correction applied to the AMS data.



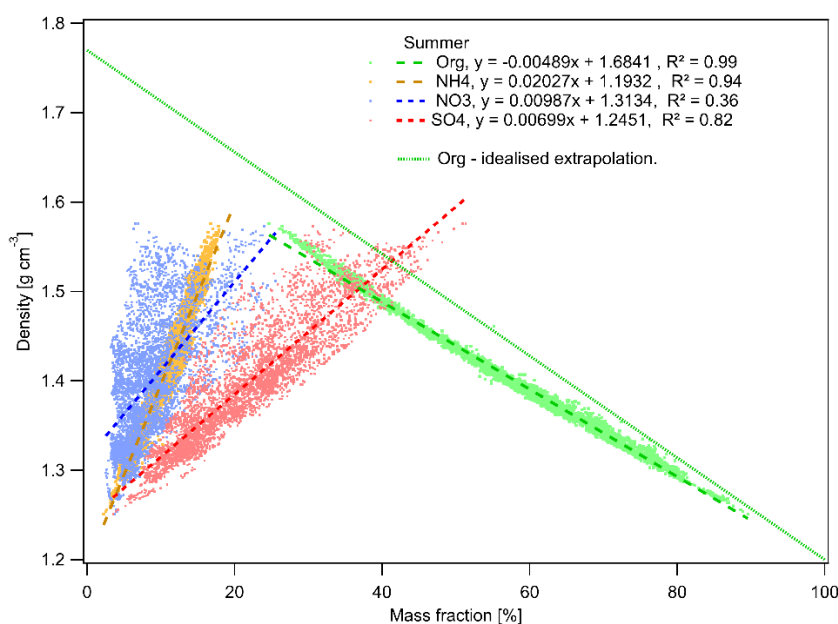


Fig. 8. The relationship between density ( $\rho_m$ ), calculated according to Eq. 2, and mass fractions of the main NR-PM<sub>1</sub> species. Idealized extrapolation of organics densities is added to the summer figure for  $\rho = 1.2 \text{ g cm}^{-3}$  at 100% Org, and  $\rho = 1.77 \text{ g cm}^{-3}$  for 0% organics.

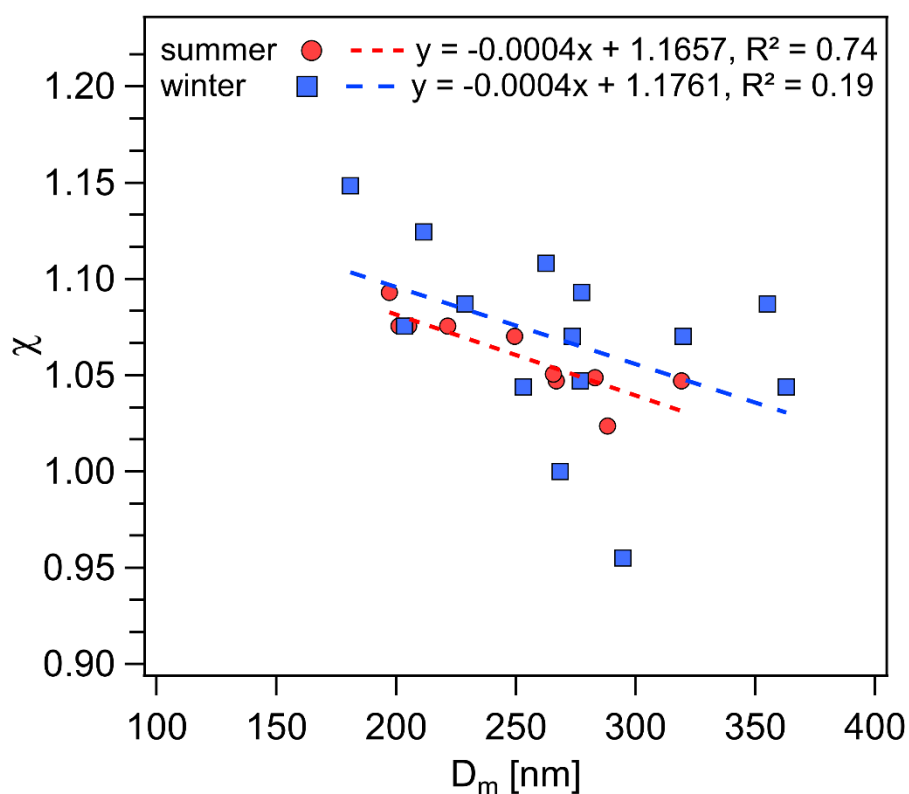


Figure 9. Calculated variation of the mobility diameter ( $D_m$ ) as a function of the dynamic shape factor ( $\chi$ ) for the summer and winter episodes of high mass concentrations.

### 3.6 Episodes of high particle number concentrations



The particle densities and shape factors was also calculated for episodes of high particle number concentrations determined by PMF application to PNSDs (see more in Section A1). PMF application to PNSDs enables us to [getretrieved](#) episodes of one factor, and therefore of same origin reflected as well as in the particle density and shape. The PMF model was run until the most physically meaningful results (factor profiles – lognormal distribution Fig. A12 and origin Fig. A13) and the best diagnostics were obtained (Tab. A2).

One high-particle-contribution episode occurred in summer, and eight short episodes occurred in winter (N W1, factor 3 of 5 and N W2 – N W8, factor 1 of 5; the durations ranged from 25 to 90 minutes, Tab. A3). No NR-PM<sub>1</sub> data were available for effective density ( $\rho_{\text{eff}}$ ) calculations during the summer period (3<sup>rd</sup> July from 9:20 to 10:05). There was only one partial overlap of episodes N W1 and W3. The densities ( $\rho_{\text{eff}}$ ) calculated using Eq. (1) ranged from 1.40 and 1.85 g cm<sup>-3</sup> and material densities ( $\rho_m$ ) based on Eq. (2) ranged from 1.30 to 1.55 g cm<sup>-3</sup>. The densities for episodes of high particle number and mass concentrations were similar in range as well as the mass median mobility diameters in the range of 261 – 623 nm and 290 – 604 nm, respectively. During N W1, accumulation-mode particles dominated (F3, mode diameter of main mode ~ 334 nm, Fig. A12, local origin, Fig. A13) with an effective density of 1.85 g cm<sup>-3</sup> (Tab. 5). A density of 2.0 g cm<sup>-3</sup> relates to aged biomass-burning particles (Moffet et al., 2008). The remaining episodes (N W2 – N W8) were linked mainly to particles of the Aitken mode (F1, mode diameter ~32 nm, Fig. A12, rather regional origin Fig. A13) with effective densities ranging from 1.40 to 1.60 g cm<sup>-3</sup> (Tab 5). Rissler et al. (2014) observed the dominance of particles with effective density ~ 1.4 g cm<sup>-3</sup> at a rural background site (Vavihill, Sweden) during the winter months, and Qiao et al. (2018) reported a decrease in particle effective densities ranging from 1.43 to 1.55 g cm<sup>-3</sup> at rural sites (Changping, China) with increasing particle sizes. The dynamic shape factor was almost constant (1.00 – 1.05) and shape of the particle spherical, except the episode N W1 (1.15) with particles of nearly spherical shape and/or as compact agglomerates.

Table 5. Particle effective densities (g cm<sup>-3</sup>) and shape factors calculated during episodes of high particle contributions to N10 – 800 using MPSS data.

| Episode MPSS                    | N W1 | N W2 | N W3 | N W4 | N W5 | N W6 | N W7 | N W8 |
|---------------------------------|------|------|------|------|------|------|------|------|
| Density ( $\rho_{\text{eff}}$ ) | 1.85 | 1.45 | 1.50 | 1.55 | 1.45 | 1.55 | 1.40 | 1.60 |
| Density ( $\rho_m$ )            | 1.50 | 1.40 | 1.50 | 1.50 | 1.40 | 1.55 | 1.30 | 1.50 |
| Jayne shape factor (S)          | 1.23 | 1.04 | 1.00 | 1.03 | 1.04 | 1.00 | 1.08 | 1.07 |
| Dynamic shape factor ( $\chi$ ) | 1.15 | 1.02 | 1.00 | 1.02 | 1.02 | 1.00 | 1.05 | 1.04 |
| # of spectra                    | 13   | 8    | 8    | 19   | 7    | 5    | 8    | 8    |

#### 4. Summary and conclusions

This study is the first of its kind in the Czech Republic to evaluate NR-PM<sub>1</sub> based on its chemically speciated mass size distribution, density, shape, and origin at a rural background site. Seasonal effects and air mass variability on aerosol particles, in particular episodes of high mass and number concentrations, were investigated using highly time-resolved measurements conducted at the National Atmospheric Observatory Košetice (NAOK) during intensive campaigns in summer 2019 and winter 2020.

The average NR-PM<sub>1</sub>+eBC concentrations were 8.58±3.70 µg m<sup>-3</sup> in summer and 10.08±8.04 µg m<sup>-3</sup> in winter, with organics dominating during both seasons, followed by SO<sub>4</sub><sup>2-</sup> in summer and NO<sub>3</sub><sup>-</sup> in winter. The accumulation mode dominated the average mass size distributions in both seasons, with the larger particles of all species in winter as a result of aerosol ageing. Therefore, larger particles in accumulation mode are also often connected with long range transport. Organics showed the smallest modal diameter from all NR-PM<sub>1</sub> chemical species, which suggests its condensation on pre-existing particles.

The performed cluster analysis revealed rare occurrences of summer continental air masses from the SE (7%) associated with the highest concentrations of PM<sub>1</sub>, eBC and all NR-PM<sub>1</sub> species. Meanwhile, predominant slow winter continental air masses from the SW (44%) were associated with inversion conditions over Central Europe associated with the highest concentrations of PM<sub>1</sub>, eBC and all NR-PM<sub>1</sub> species.

Analysis of the diurnal trend of average ρ<sub>m</sub> showed a diurnal trend for winter that was opposite to the diurnal trend of organics, reflecting the change in aerosol composition toward local chemical formation of NO<sub>3</sub><sup>-</sup> during the night, and probably also the change in total aerosol organics density during the day and night. The studied relationships between ρ<sub>m</sub> (with different input of Org density), ρ<sub>eff</sub>, -and mass fractions of the main NR-PM<sub>1</sub> species suggest that the application of the density usually used in urban environments for organics (1.2 g cm<sup>-3</sup>) is inappropriate for rural aerosol particles due to the aging of organic aerosols and should be probably used higher value around 1.3 – 1.4 g cm<sup>-3</sup>.

Considering the seasonal differences in the χ of the episodes with high mass concentrations, the χ was almost constant in summer, indicating almost spherical mainly organic particles, compared to winter, indicating almost spherical shape and/or compact agglomerates with a slight statistically significant decrease in χ with particle size. This could be caused by larger influence of irregular BC/EC core in winter, continuously coated by both organic and inorganic compounds making the larger particles more and more spherical. On the other hand, χ was almost constant in the episode of high number concentrations and the shape of the particles was spherical with no decreasing trend in χ with particle size.

By examining individual episodes of high mass and number concentrations, we show that the seasonal differences in the physicochemical properties of aerosol particles were caused by the diversity of sources and were related to the different air masses and meteorological conditions during summer and winter season. We also confirmed the relation between particle size and age reflected both in its oxidation state and shape factor. The results of these specific properties (density, shape and oxidation state of particles) have general validity and thus transcend the regional character of this study.

#### *Data availability.*

All relevant data for this paper ~~are~~<sup>is</sup> archived at the ICPF of the CAS (Institute of Chemical Process Fundamentals of the Czech Academy of Sciences) and are available upon request from the corresponding author (Petra Pokorná).

#### *Author contribution.*

PP, JS and VŽ conceived the research. PP, RL, PV, SM, AHŠ and JO conducted the atmospheric aerosol measurements during both intensive campaigns. PP, NZ, RL, PV, VR and

JS analysed and interpreted the data. PP prepared the manuscript with contributions from all co-authors.

#### *Competing interests*

The authors declare that they have no conflict of interest.

#### *Acknowledgements*

We would like to thank Daniel Vondrák for the graphical editing. Thanks also goes to American Journal Experts [and Laurence Windell](#) for the English proof reading of the manuscript. The authors gratefully acknowledge the NOAA Air Resources Laboratory (ARL) for the provision of the HYSPLIT transport and dispersion model and/or READY website (<http://www.ready.noaa.gov>) used in this publication. We greatly thank the two anonymous reviewers for their effort to critically review the manuscript and for providing constructive comments.

#### *Financial support*

This work was supported by the GACR under grant P209/19/06110Y and by the MEYS of the Czech Republic under grant ACTRIS-CZ LM2018122 and ACTRIS-CZ RI (CZ.02.1.01/0.0/0.0/16\_013/0001315) as well as by COST Action CA16109 COLOSSAL within STSM.

#### **References**

- Allan, J.D., Delia, A.E., Coe, H., Bower, K.N., Alfarra, M.R., Jimenez, J.L., Middlebrook, A.M., Drewnick, F., Onasch, T.B., Canagaratna, M.R., Jayne, J.T., Worsnop, D.R., 2004. A generalised method for the extraction of chemically resolved mass spectra from Aerodyne aerosol mass spectrometer data. *J. Aerosol Sci.* 35, 909–922.
- Allan, J.D., Alfarra, M.R., Bower, K.N., Coe, H., Jayne, J.T., Worsnop, D.R., Aalto, P.P., Kulmala, M., Hyötyläinen, T., Cavalli, F., Laaksonen, A., 2006. Size and composition measurements of background aerosol and new particle growth in a Finnish forest during QUEST 2 using an Aerodyne Aerosol Mass Spectrometer. *Atmos. Chem. Phys.* 6, 315–327.
- Belis, C.A., Karagulian, F., Larsen, B.R., Hopke, P.K., 2013. Critical review and metaanalysis of ambient particulate matter source apportionment using receptor models in Europe. *Atmos. Environ.* 69, 94–108.
- Bressi, M., Cavalli, F., Putaud, J.P., Fröhlich, R., Petit, J.-E., Aas, W., Äijälä, A., Alastuey, A., Allan, J.D., Aurela, M., Berico, M., Bougiatioti, A., others. 2021. A European aerosol phenomenology - 7: High-time resolution chemical characteristics of submicron particulate matter across Europe. *Atmospheric Environment: X* 10, 100108, 1–16.
- Carslaw, D.C., Ropkins, K., 2012. Openair – an R package for air quality data analysis. *Environ. Model. Software* 27–28, 52–61.
- Cavalli, F., Viana, M., Ytri, K.E., Genberg, J., Putaud, J.-P., 2010. Toward a standardised thermal-optical protocol for measuring atmospheric organic and elemental carbon: the EUSAAR protocol. *Atmospheric Measurement Techniques* 3, 79–89.
- [Cavallia, F., Alastue, A., Areskoug, H., Ceburnis, D., Čech, J., Genber, J., Harrison, R.M., Jaffrezo, J.L., Kiss, G., Laj, P., Mihalopoulos, N., Perez, N., Quincey, P., Schwarz, J., Sellegri, K., Spindler, G., Swietlicki, E., Theodosi, C., Putaud, J.P., 2016. A European](#)

aerosol phenomenology – 4: Harmonized concentrations of carbonaceous aerosol at 10 regional background sites across Europe. *Atmospheric Environment* 144, 133-145.

Chen, G. et al., 2021 (under review). *European Aerosol Phenomenology – 8: Harmonised Source Apportionment of Organic Aerosol using 22 Yearlong ACSM/AMS Datasets*.

Costabile, F., Birmili, W., Klose, S., Tuch, T., Wehner, B., Wiedensohler, A., Franck, U., König, K. and Sonntag, A., 2009. Spatio-Temporal Variability and Principal Components of the Particle Number Size Distribution in an Urban Atmosphere. *Atmos. Chem. Phys.* 9: 3163–3195.

CHMI, Tabular Survey 2019, Czech Hydrometeorological Institute (CHMI) 2019(a) [http://portal.chmi.cz/files/portal/docs/uoco/isko/tab\\_roc/2019\\_enh/index\\_GB.html](http://portal.chmi.cz/files/portal/docs/uoco/isko/tab_roc/2019_enh/index_GB.html), last access: 4.6.2021

CHMI, Annual report 2019, Czech Hydrometeorological Institute (CHMI) 2019(b) [https://www.chmi.cz/files/portal/docs/uoco/isko/grafroc/19groc/gr19cz/19\\_rocenka\\_UKO\\_web\\_tisk\\_up1.pdf](https://www.chmi.cz/files/portal/docs/uoco/isko/grafroc/19groc/gr19cz/19_rocenka_UKO_web_tisk_up1.pdf), last access: 4.6.2021

Cubison, M.J., Ortega, A.M., Hayes, P.L., Farmer, D.K., Day, D., Lechner, M.J., Brune, W.H., Apel, E., Diskin, G.S., Fisher, J. a., Fuelberg, H.E., Hecobian, A., Knapp, D.J., Mikoviny, T., Riemer, D., Sachse, G.W., Sessions, W., Weber, R.J., Weinheimer, A.J., Wisthaler, A., Jimenez, J.L., 2011. Effects of aging on organic aerosol from open biomass burning smoke in aircraft and laboratory studies. *Atmos. Chem. Phys.* 11, 12049–12064.

Crippa, M., DeCarlo, P. F., Slowik, J. G., Mohr, C., Heringa, M. F., Chirico, R., Poulain, L., Freutel, F., Sciare, J., Cozic, J., Di Marco, C. F., Elsasser, M., Nicolas, J. B., Marchand, N., Abidi, E., Wiedensohler, A., Drewnick, F., Schneider, J., Borrmann, S., Nemitz, E., Zimmermann, R., Jaffrezo, J.-L., Prévôt, A. S. H., and Baltensperger, U. 2013. Wintertime aerosol chemical composition and source apportionment of the organic fraction in the metropolitan area of Paris, *Atmos. Chem. Phys.*, 13, 961-981, doi:10.5194/acp-13-961-2013, 2013.

Dall’Osto, M., Harrison, R.M., Coe, H., Williams, P.I., Allan, J.D., 2009. Real time chemical characterization of local and regional nitrate aerosols. *Atmos. Chem. Phys.*, 9, 3709-3720.

DeCarlo, P.F., Slowik, J.G., Worsnop, D.R., Davidovits, P., Jimenez, J.L., 2004. Particle Morphology and Density Characterization by Combined Mobility and Aerodynamic Diameter Measurements. Part 1: Theory. *Aerosol Sci. Technol.* 38, 1185–1205.

Drewnick, F., Jayne, J.T., Canagaratna, M., Worsnop, D.R., Demerjian, K.L., 2004. Measurement of ambient aerosol composition during the PMTACS-NY 2001 Using and Aerosol Mass Spectrometer. Part II: Chemically speciated mass distribution.

Drewnick, F., Hings, S.S., DeCarlo, P., Jayne, J.T., Gonin, M., Fuhrer, K., Weimer, S., Jimenez, J.L., Demerjian, K.L., Borrmann, S., Worsnop, R., 2005. A new Time-of-Flight Aerosol Mass Spectrometer (TOF-AMS) – Instrument description and first field deployment. *Aerosol Science and Technology* 39, 637–658.

EEA, 2019. Air Quality in Europe - 2019 Report. European Environment Agency Report No 10/2019. <https://www.eea.europa.eu/publications/air-quality-in-europe-2019>.

Favez, O., Weber, S., Petit, J.-E., Alleman, L.Y., Albinet, A., Riffault, V., Chazeau, B., Amodeo, T., Salameh, D., Zhang, Y., Srivastava, S. et al., 2021. Overview of the French Operational Network for In Situ Observation of PM Chemical Composition and Sources in Urban Environments (CARA Program). *Atmosphere* 12, 207, 1-43.

Freney, E. J., Sellegri, K., Canonaco, F., Boulon, J., Hervo, M., Weigel, R., Pichon, J. M., Colomb, A., Prévôt, A.S.H., and Laj, P., 2011. Seasonal variations in aerosol particle composition at the puy-de-Dôme research station in France, *Atmos. Chem. Phys.*, 11, 13047–13059.

Freney, E.J., Sellegri, K., Canonaco, F., Colomb, A., Borbon, A., Michoud, V., Doussin, J., F., Crumeyrolle, S., Amarouche, N., Pichon, J.M., Bourianne, L., Gomes, L., Prévôt, A.S.H.,



- Beekmann, M., Schwarzenböck, A., 2014. Characterizing the impact of urban emission on regional aerosol particles: airborne measurements during the MEGAPOLI experiment. *Atmos. Chem. Phys.* 14, 1397–1412.
- Freutel, F., Schneider, J., Drewnick, von der Weiden-Reinmüller, S.L., Crippa, M., Prévôt, A.S.H., Baltensperger, U., Poulain, L., Wiedensohler, A., Sciare, J., Sarda-Estève, R., Burkhardt, J.F., Eckhardt, S., Stohl, A., Gros, V., Colomb, A., Michoud, V., Doussin, J.F., Borbon, A., Haeffelin, M., Morille, Y., Beekmann, M., Borrmann, S., 2013. Aerosol particle measurements at three stationary sites in the megacity of Paris during summer 2009: meteorology and air mass origin dominated aerosol particle composition and size distribution. *Atmos. Chem. Phys.* 13, 933–959.
- Fröhlich, R., Cubison, M. J., Slowik, J. G., Bukowiecki, N., Canonaco, F., Croteau, P. L., Gysel, M., Henne, S., Herrmann, E., Jayne, J. T., Steinbacher, M., Worsnop, D. R., Baltensperger, U., and Prévôt, A. S. H., 2015. Fourteen months of on-line measurements of the non-refractory submicron aerosol at the Jungfraujoch (3580 m a.s.l.) – chemical composition, origins and organic aerosol sources. *Atmos. Chem. Phys.* 15, 11373–11398.
- Hersey, S.P., Craven, J.S., Shilling, K.A., Metcalf, A.R., Sorooshian, A., Chan, M.N., Flagan, R.C., Seinfeld, J.H., 2011. The Pasadena Aerosol Characterization Observatory (PACO): chemical and physical analysis of the Western Los Angeles basin aerosol. *Atmos. Chem. Phys.* 11, 7417–7443.
- Hinds, W. C., 1999. *Aerosol Technology*. 2nd ed. John Wiley & Sons. New York.
- Holubová Šmejkalová, A., Zíková, N., Ždímal, V., Plachá, H., Bitter, M., 2021. Atmospheric aerosol growth rates at different background station types. *Environmental Science and Pollution Research* 28, 13352–13364.
- Hock, N., Schneider, J., Borrmann, S., Römpf, A., Moortgat, G., Franze, T., Schauer, C., Pöschl, U., Plass-Dülmer, C., Berresheim, H., 2008. Rural continental aerosol properties and processes observed during the Hohenpeissenberg Aerosol Characterization Experiment (HAZE2002). *Atmos. Chem. Phys.* 8, 603–623.
- ~~Hu, M., Peng, J., Sun, K., Yue, D., Guo, S., Wiedensohler, A., Wu, Z., 2012. Estimation of size-resolved ambient particle density based on the measurement of aerosol number, mass, and chemical Size Distributions in the winter in Beijing. *Environmental Science & Technology* 46, 9941–9947.~~
- Jayne, J. T., Leard, D. C., Zhang, X., Davidovits, P., Smith, K. A., Kolb, C. E., and Worsnop, D. R., 2000. Development of an Aerosol Mass Spectrometer for Size and Composition Analysis of Submicron Particles, *Aerosol Sci. Technol.*, 33, 49–70, 2000.
- Jimenez, J. L., Jayne, J. T., Shi, Q., Kolb, C. E., Worsnop, D. R., Yourshaw, I., Seinfeld, J. H., Flagan, R. C., Zhang, X., Smith, K. A., Morris, J., and Davidovits, P., (2003a)–. Ambient aerosol sampling using the Aerodyne Aerosol Mass Spectrometer, *J. Geophys. Res.*, 108, 8425.
- Jimenez, J. L., Bahreini, R., Cocker, D. R., III, Zhuang, H., Varutbangkul, v., Flagan, R. C., Seinfeld, J. H., O'Dowd, C D., and Hoffman, T (2003b). New Particle Formation from Photooxidation of Diiodomethane (CH<sub>2</sub>I<sub>2</sub>). *J. Geophys. Res.s-Atmos.* 108(D10):AAC5/1-AAC5/25.
- Jimenez, J. L., Bahreini, R., Cocker, D. R., III, Zhuang, H., Varutbangkul, v., Flagan, R. C., Seinfeld, J. H., O'Dowd, C D., and Hoffman, T (2003c). Correction to "New Particle Formation from Photooxidation of Diiodomethane (CH<sub>2</sub>I<sub>2</sub>)," *J. Geophys. Res.- Atmos.* 108(D23):4733.
- Jimenez, J.L., M.R. Canagaratna, N.M. Donahue, A.S.H. Prevot, Q. Zhang, J.H. Kroll, P.F. DeCarlo, J.D. Allan, H. Coe, N.L. Ng, A.C. Aiken, K.D. Docherty, I.M. Ulbrich, A.P. Grieshop, A.L. Robinson, J. Duplissy, J. D. Smith, K.R. Wilson, V.A. Lanz, C. Hueglin, Y.L. Sun, J. Tian, A. Laaksonen, T. Raatikainen, J. Rautiainen, P. Vaattovaara, M. Ehn, M.



- Kulmala, J.M. Tomlinson, D.R. Collins, M.J. Cubison, E.J. Dunlea, J.A. Huffman, T.B. Onasch, M.R. Alfarra, P.I. Williams, K. Bower, Y. Kondo, J. Schneider, F. Drewnick, S. Borrmann, S. Weimer, K. Demerjian, D. Salcedo, L. Cottrell, R. Griffin, A. Takami, T. Miyoshi, S. Hatakeyama, A. Shimono, J.Y. Sun, Y.M. Zhang, K. Dzepina, J.R. Kimmel, D. Sueper, J.T. Jayne, S.C. Herndon, A.M. Trimborn, L.R. Williams, E.C. Wood, C.E. Kolb, A.M. Middlebrook, U. Baltensperger, and D.R. Worsnop, 2009. Evolution of Organic Aerosols in the Atmosphere, *Science*, 326, 1525-1529., doi: 10.1126/science.1180353, 2009.
- Kozáková, J., Pokorná, P., Vodička, P., Ondráčková, L., Ondráček, J., Křůmal, K., Mikuška, P., Hovorka, J., Moravec, P., Schwarz, J., 2019. Influence of regional air pollution transport at a European air pollution hotspot. *Environ Sci Pollut Res* 26, 1675–1692.
- Křůmal, K., Mikuška, P., 2020. Mass concentrations and lung cancer risk assessment of PAHs bound to PM1 aerosol in six industrial, urban and rural areas in the Czech Republic, Central Europe. *Atmospheric Pollution Research* 11, 401–408.
- Kubelová, L., Vodička, P., Schwarz, J., Cusack, M., Makeš, O., Ondráček, J., Ždímal, V., 2015. A study of summer and winter high time-resolved submicron aerosol composition measured at a suburban site in Prague. *Atmospheric Environment* 118, 45–57.
- Mbengue, S., Fusek, M., Schwarz, J., Vodička, P., Holubová Šmejkalová, A. Holoubek, I., 2018. Four years of highly time resolved measurements of elemental and organic carbon at a rural background site in Central Europe. *Atmos. Environ.*, 182, 335–346.
- Lide, D. R.: CRC Handbook of Chemistry and Physics, CRC Press Inc, USA, 1991.
- Mbengue, S., Serfozo, N., Schwarz, J., Ziková, N., Holubová Šmejkalová, A., Holoubek, I. 2020. Characterization of Equivalent Black Carbon at a regional background site in Central Europe: Variability and source apportionment. *Environmental Pollution* 260, 113771
- Mikuška, P., Hopke, P.K., 2018. Source apportionment of aerosol particles at a European air pollution hot spot using particle number size distributions and chemical composition. *Environ. Pollut.* 234, 145–154.
- ~~Martins, J.V., Artaxo, P., Liousse, C., Reid, J.S., Hobbs, P.V., Kaufman, Y.J., 1998. Effects of black carbon content, particle size, and mixing on light absorption by aerosols from biomass burning in Brazil. *Journal of Geophysical Research* 103, 32,041–32,050.~~
- Middlebrook, A.M., Bahreini, R., Jimenez, J.L., Canagaratna, M.R., 2012. Evaluation of Composition-Dependent Collection Efficiencies for the Aerodyne Aerosol Mass Spectrometer using Field Data. *Aerosol Science and Technology* 46, 258–271.
- Milic, A., Mallet, M.D., Cravigan, L.T., Alroe, J., Ristovski, Z.D., Selleck, P., Lawson, S.J., Ward, J., Desservettaz, M.J., Paton-Walsh, C., Williams, L.R., Keywood, M.D., Miljevic, B., Biomass burning and biogenic aerosols in northern Australia during the SAFIRE campaign. *Atmos. Chem. Phys.* 17, 3945–3961.
- Moffet, R. C., Qin, X. Y., Rebotier, T., Furutani, H., and Prather, K. A., 2008. Chemically segregated optical and microphysical properties of ambient aerosols measured in a single-particle mass spectrometer, *J. Geophys. Res.-Atmos.*, 113, D12213.
- Ng, N.L., Canagaratna, M.R., Zhang, Q., Jimenez, J.L., Tian, J., Ulbrich, I.M., Kroll, J.H., Docherty, K.S., Chhabra, P.S., Bahreini, R., Murphy, S.M., Seinfeld, J.H., Hildebrandt, L., Donahue, N.M., DeCarlo, P.F., Lanz, V.A., Prévot, A.S.H., Dinar, E., Rudich, Y., Worsnop, D.R., 2010. Organic aerosol components observed in Northern Hemispheric datasets from Aerosol Mass Spectrometry. *Atmos. Chem. Phys.* 10, 4625–4641.
- Park, K., Kittelson, D. B., Zachariah, M. R., and McMurtry, P. H.: Measurement of Inherent Material Density of Nanoparticle Agglomerates, *J. Nanopart. Res.*, 6, 267–272, 2004.
- ~~Pitz, M., Cyrus, J., Karg, E., Wiedensohler, A., Wichmann, H.E., Heinrich, J., 2003. Variability of apparent particle density of an urban aerosol. *Environmental Science & Technology* 37, 4336–4342.~~

- Pitz, M., Schmid, O., Heinrich, J., Birmili, W., Maguhn, J., Zimmermann, R., Wichmann, H.E., Peters, A., Cyrys, J., 2008. Seasonal and Diurnal Variation of PM<sub>2.5</sub> Apparent Particle Density in Urban Air in Augsburg, Germany. *Environmental Science & Technology* 42, 5087–5093.
- Petit, J.-E., Amodeo, T., Meleux, F., Bessagnet, B., Menut, L., Grenier, D., Pellan, Y., Ockler, A., Rocq, B.; Gros, V., et al., 2017. Characterising an intense PM pollution episode in March 2015 in France from multi-site approach and near real time data. *Atmos. Environ.* 155, 68–84.
- Petit, J.-E., Pallarès, C., Favez, O., Alleman, L.Y., Bonnaire, N., Rivière, E., 2019. Sources and Geographical Origins of PM<sub>10</sub> in Metz (France) Using Oxalate as a Marker of Secondary Organic Aerosols by Positive Matrix Factorization Analysis. *Atmosphere* 10, 370.
- Pokorná, P., Schwarz, J., Krejci, R., Swietlicki, E., Havránek, V., Ždímal, V., 2018. Comparison of PM<sub>2.5</sub> chemical composition and sources at a rural background site in Central Europe between the years 1993/1994/1995 and 2009/2010: Effect of legislative regulations and economic transformation on the air quality. *Environmental Pollution* 241, 841–851.
- Poulain, L., Spindler, G., Birmili, W., Plass-Dülmer, C., Wiedensohler, A., Herrmann, H., 2011. Seasonal and diurnal variations of particulate nitrate and organic matter at the IfT research station Melpitz. *Atmos. Chem. Phys.* 11 (24), 12579–12599.
- Poulain, L., Spindler, G., Grüner, A., Tuch, T., Stieger, B., van Pinxteren, D., Petit, J.-E., Favez, O., Herrmann, H., Wiedensohler, A., 2020. Multi-year ACSM measurements at the central European Research station Melpitz (Germany) – Part 1: Instrument robustness, quality assurance, and impact of upper size cutoff diameter. *Atmos. Meas. Tech.*, 13, 4973–4994.
- Putaud, J.P., Raes, F., Van Dingenen, R., Brüggemann, E., Facchini, M., Decesari, S., Fuzzi, S., Gehrig, R., Hüglin, C., Laj, P., others, 2004. A European aerosol phenomenology—2: chemical characteristics of particulate matter at kerbside, urban, rural and background sites in Europe. *Atmos. Environ.* 38, 2579–2595.
- Putaud, J.P., Van Dingenen, R., Alastuey, A., Bauer, H., Birmili, W., Cyrys, J., Flentje, H., Fuzzi, S., Gehrig, R., Hansson, H.C., others, 2010. A European aerosol phenomenology — 3: physical and chemical characteristics of particulate matter from 60 rural, urban, and kerbside sites across Europe. *Atmos. Environ.* 44, 1308–1320.
- Qiao, K., Wu, Z., Pei, X., Liu, Q., Shang, D., Zheng, J., Du, Z., Zhu, W., Wu, Y., Lou, S., Guo, S., Chan, C.K., Pathak, R.K., Hallquist, M., Hu, M., 2018. Size-resolved effective density of submicron particles during summertime in the rural atmosphere of Beijing, China. *Journal of Environmental Sciences* 73, 69–77.
- Querol, X., Alastuey, A., Puigercus, J.A., Mantilla, E., Ruiz, C.R., Lopez-Soler, A., Plana, F., Juan, R., 1998. Seasonal evolution of suspended particles around a large coal-fired power station: chemical characterization. *Atmos. Environ.* 32, 719–731.
- Rissler, J., Nordin, E.Z., Eriksson, A.C., Nilsson, P.T., Frosch, M., Sporre, M.K., Wierzbicka, A., Svenningsson, B., Löndahl, J., Messing, M.E., Sjogren, S., Hemmingsen, J.G., Loft, S., Pagels, J.H., Swietlicki, E., 2014. *Environ. Sci. Technol.* 48, 11, 6300–6308
- Rolph, G., Stein, A., Stunder, B., 2017. Real-time environmental applications and display sYstem: READY. *Environ. Model. Software* 95, 210–228.
- Salcedo, D., Onasch, T. B., Dzepina, K., Canagaratna, M. R., Zhang, Q., Huffman, J. A., DeCarlo, P. F., Jayne, J. T., Mortimer, P., Worsnop, D. R., Kolb, C. E., Johnson, K. S., Zuberi, B., Marr, L. C., Volkamer, R., Molina, L. T., Molina, M. J., Cardenas, B., Bernabé, R. M., Márquez, C., Gaffney, J. S., Marley, N. A., Laskin, A., Shutthanandan, V., Xie, Y., Brune, W., Leshner, R., Shirley, T., and Jimenez, J. L., 2006. Characterization of ambient aerosols in Mexico City during the MCMA-2003 campaign with Aerosol Mass Spectrometry: results from the CENICA Supersite. *Atmos. Chem. Phys.* 6, 925–946.

- Salimi, F., Crilley, L.R., Stevanovic, S., Ristovski, Z., Mazaheri, M., He, C., Johnson, G., Ayoko, G., Morawska, L., 2015. Insights into the growth of newly formed particles in a subtropical urban environment. *Atmos. Chem. Phys.* 15, 13475–13485.
- Schwarz, J., Chi, X., Maenhaut, W., Civis, M., Hovorka, J., Smolík, J., 2008. Elemental and organic carbon in atmospheric aerosols at downtown and suburban sites in Prague. *Atmos. Res.* 90, 287–302.
- Schwarz, J., Štefancová, L., Maenhaut, W., Smolík, J., Ždímal, V., 2012. Mass and chemically speciated size distribution of Prague aerosol using an aerosol dryer – The influence of air mass origin. *Science of the Total Environment*
- Schwarz, J., Cusack, M., Karban, J., Chalupníčková, E., Havránek, V., Smolík, J., Ždímal, V., 2016. PM<sub>2.5</sub> chemical composition at a rural background site in Central Europe, including correlation and air mass back trajectory analysis. *Atmospheric Research* 176–177, 108–20.
- Seinfeld, J.H., Pandis, S.N., 2006. *Atmospheric Chemistry and Physics*. John Wiley & Sons, New York.
- Slowik, J.G., Stanken, K., Davidovits, P., Williams, L.R., Jayne, J.T., Kolb, C.E., Worsnop, D.R., Rudich, Y., DeCarlo, P.F., Jimenez, J.L., 2004. Particle Morphology and Density Characterization by Combined Mobility and Aerodynamic Diameter Measurements. Part 2: Application to Combustion-Generated Soot Aerosols as a Function of Fuel Equivalence Ratio *Aerosol Science and Technology*, 38, 1206–1222.
- Takegawa, N., Miyazaki, Y., Kondo, Y., Komazaki, Y., Miyakawa, T., Jimenez, J.L., Jayne, J.T., Worsnop, D.R., Allan, J.D., Weber, R.J., 2005. Characterization of an Aerodyne Aerosol Mass Spectrometer (AMS): Intercomparison with Other Aerosol Instruments, *Aerosol Science and Technology*, 39:8, 760–770.
- Turpin, B. J. and Lim, H.-J., 2001. Species contributions to PM<sub>2.5</sub> mass concentrations: revisiting common assumptions for estimating organic mass, *Aerosol Sci. Tech.*, 35, 302–610.
- Vodička, P., Kawamura, K., Schwarz, J., Kunwar, B., Zdímal, V., 2019. Seasonal study of stable carbon and nitrogen isotopic composition in fine aerosols at a Central European rural background station. *Atmos. Chem. Phys.* 19, 3463–3479.
- Vu, T.V., Delgado-Saborit, J.M., Harrison, R.M., 2015. Review: particle number size distributions from seven major sources and implications for source apportionment studies. *Atmos. Environ.* 122, 114–132.
- Waked, A., Favez, O., Alleman, L.Y., Piot, C., Petit, J.-E., Delaunay, T., Verlinden, E., Golly, B., Besombes, J.-L., Jaffrezo, J.-L., 2014. Source apportionment of PM<sub>10</sub> in a north-western Europe regional urban background site (Lens, France) using positive matrix factorization and including primary biogenic emissions. *Atmos. Chem. Phys.* 14, 3325–3346.
- ~~Watson, J.G., Chow J.C., 2011, Ambient aerosol sampling. In: Kulkarni, P., Baron, P.A., Willeke, K (eds) Aerosol measurement: principles, techniques and applications, third edition, 3rd edn. John Wiley & Sons, Inc., Hoboken, NJ, USA, pp 591–614.~~
- Wickham, H., 2016. *ggplot2: Elegant Graphics for Data Analysis*. Springer-Verlag, New York.
- Wiedensohler, A., Wiesner, A., Weinhold, K., Birmili, W., Hermann, H., Merkel, M., Müller, T., Pfeifer, S., Schmidt, A., Tuch, T., Velarde, F., Quincey, P., Seeger, S., Nowak, A., 2017. Mobility particle size spectrometers: Calibration procedures and measurement uncertainties. *Aerosol Science and Technology*, 52:2, 146–164.
- Zelenyuk, A., Cai, Y., Imre, D., 2006. From Agglomerates of Spheres to Irregularly Shaped Particles: Determination of Dynamic Shape Factors from Measurements of Mobility and Vacuum Aerodynamic Diameters. *Aerosol Science and Technology*, 40, 197–217.

- Zíková, N., Ždímal, V., 2013. Long-Term Measurement of Aerosol Number Size Distributions at Rural Background Station Košetice. *Aerosol and Air Quality Research*, 13, 1464–1474.
- Zíková, N., Ždímal, V., 2016. Precipitation scavenging of aerosol particles at a rural site in the Czech Republic. *Tellus B: Chemical and Physical Meteorology* 68, 27343, 1–14.

## APPENDIX

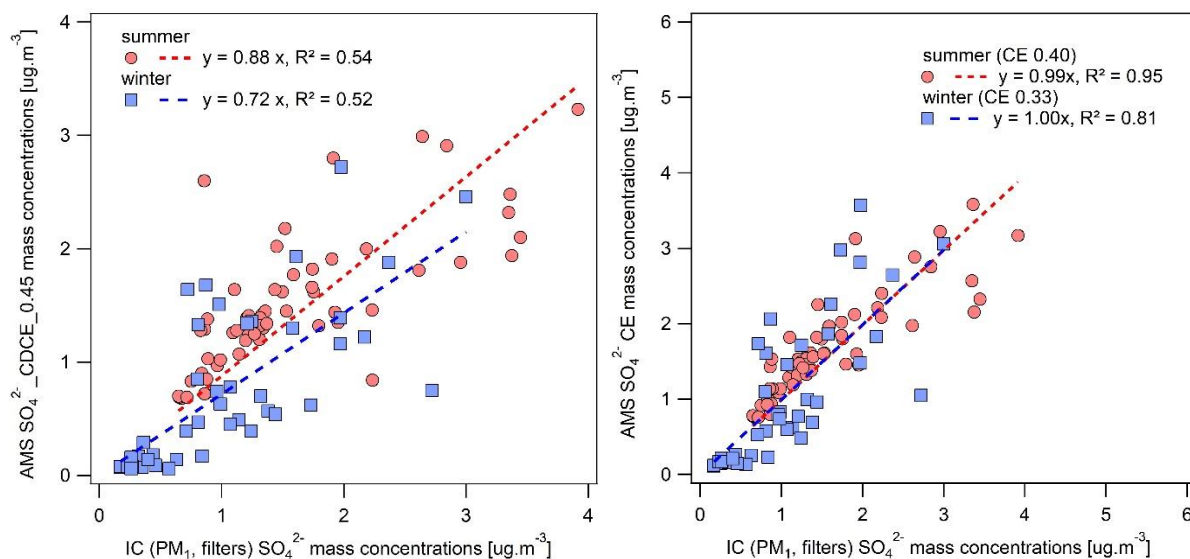
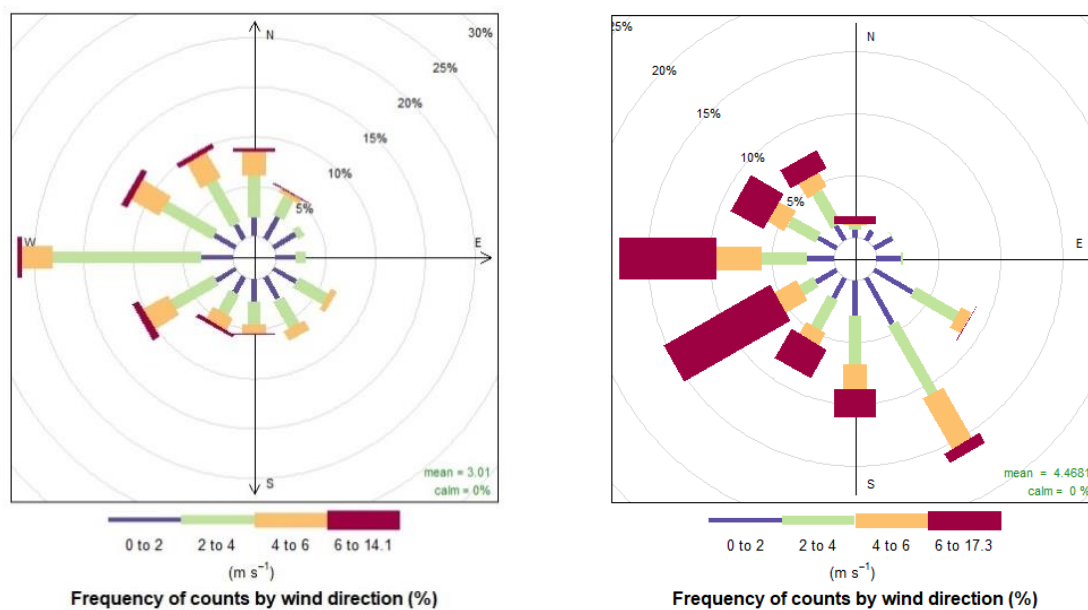


Figure A1. Comparison of sulphate concentrations measured by AMS and retrieved from  $\text{PM}_{10}$  filter analysis by IC with applied CDCE correction (left) and constant CE correction (right) for both measurement seasons.





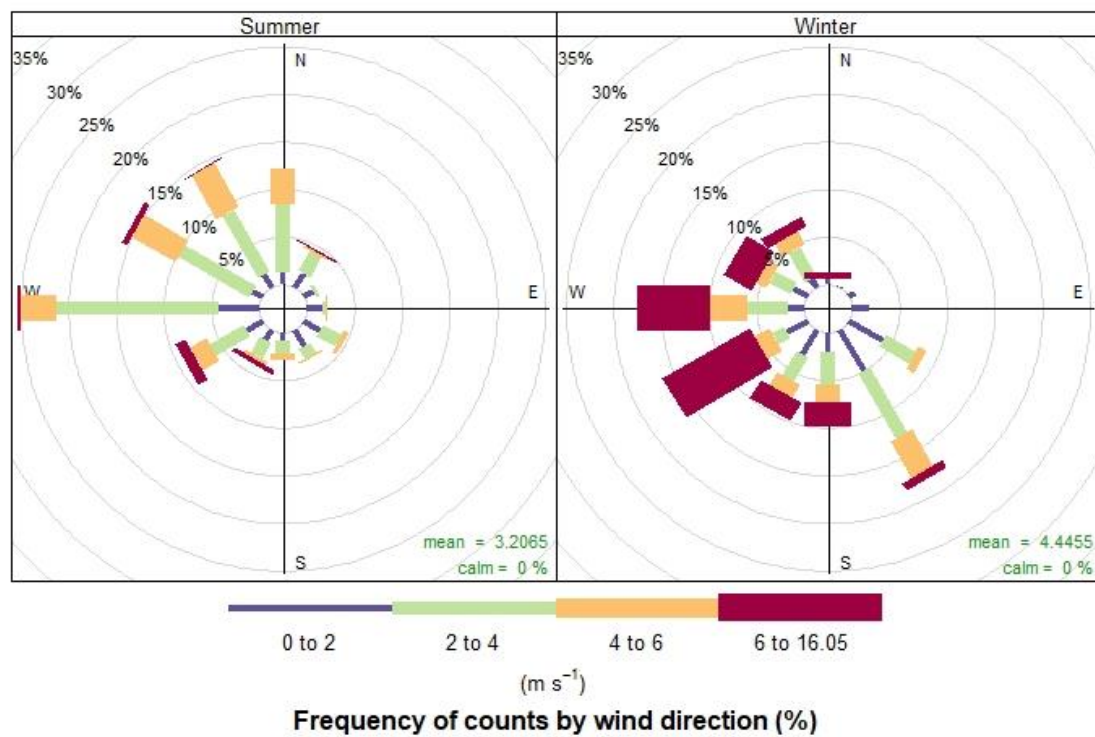


Figure A2. Wind rose summer and winter.

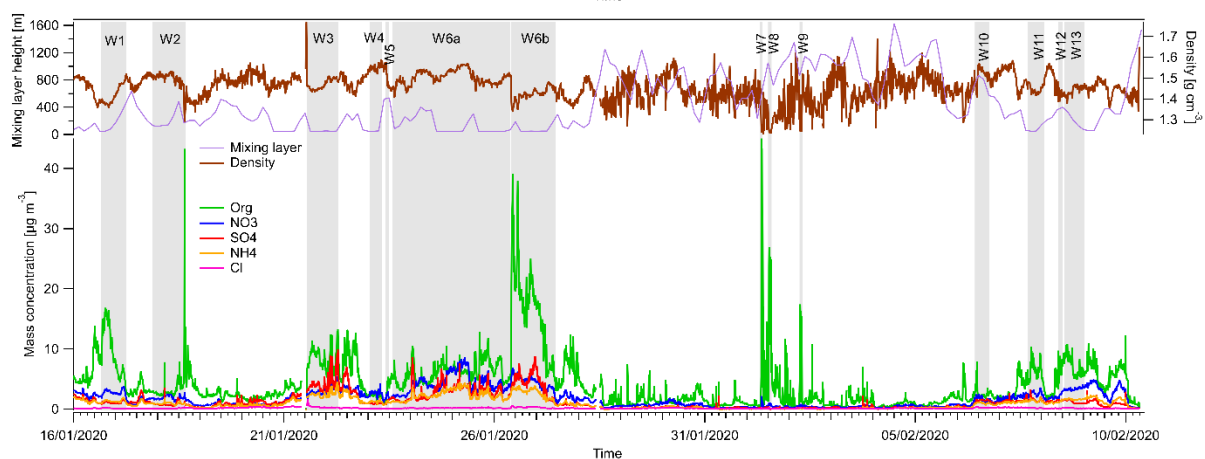
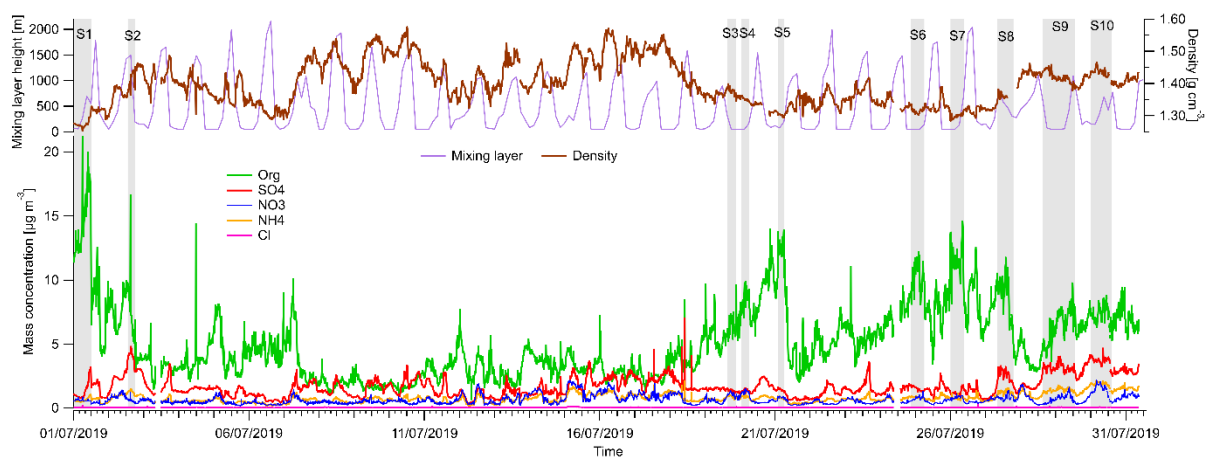


Figure A3. Mass concentration of Org, NO<sub>3</sub><sup>-</sup>, SO<sub>4</sub><sup>2-</sup>, and NH<sub>4</sub><sup>+</sup> measured by AMS with applied constant collection efficiency (CE) correction for summer (top) and winter (bottom) campaign with marked episodes of higher mass concentrations, mixing layer height and particle effective density calculated using Eq. (2) in the main text from Salcedo et al., 2006.

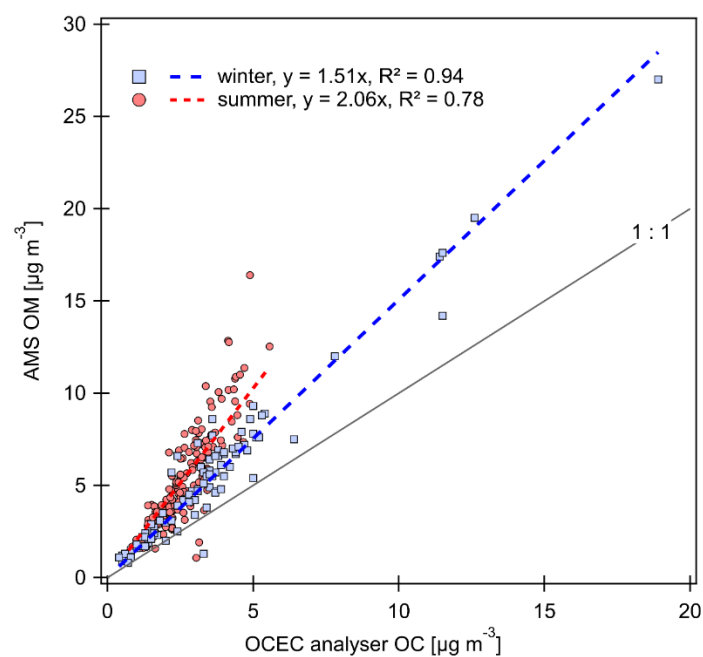


Figure A4. Comparison of organic mass concentration measured on-line by AMS (Org CE corrected) and by OCEC analyser in summer and winter.

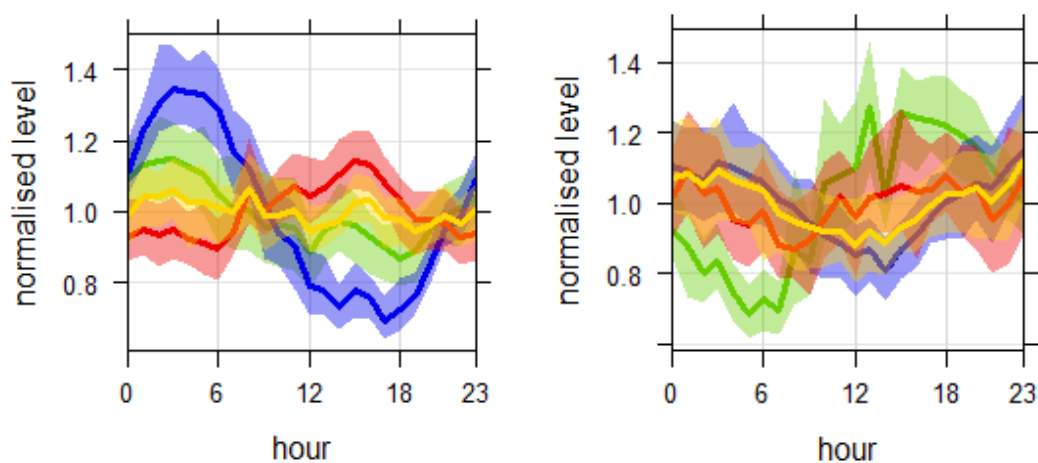


Figure A5. Diurnal trends of the NR-PM<sub>1</sub> species (common colour code) in summer (left) and winter (right).

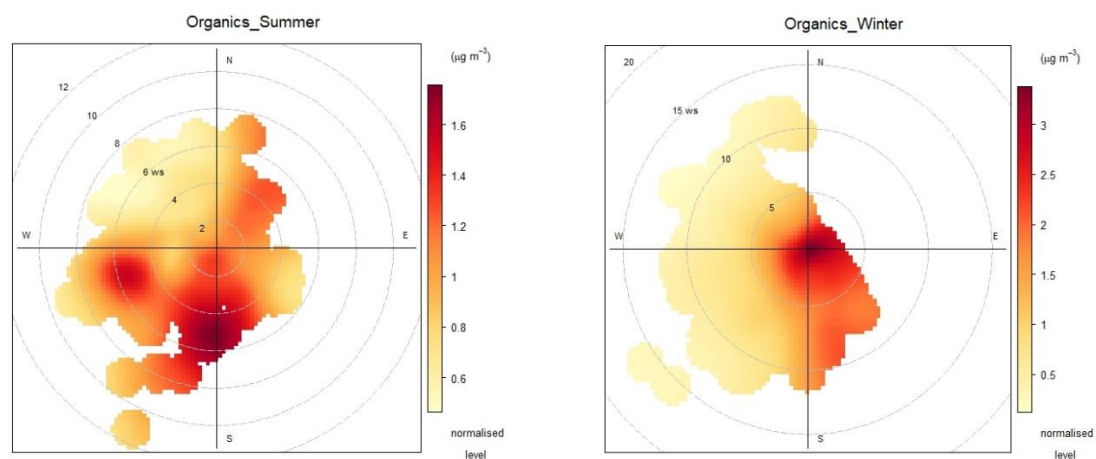


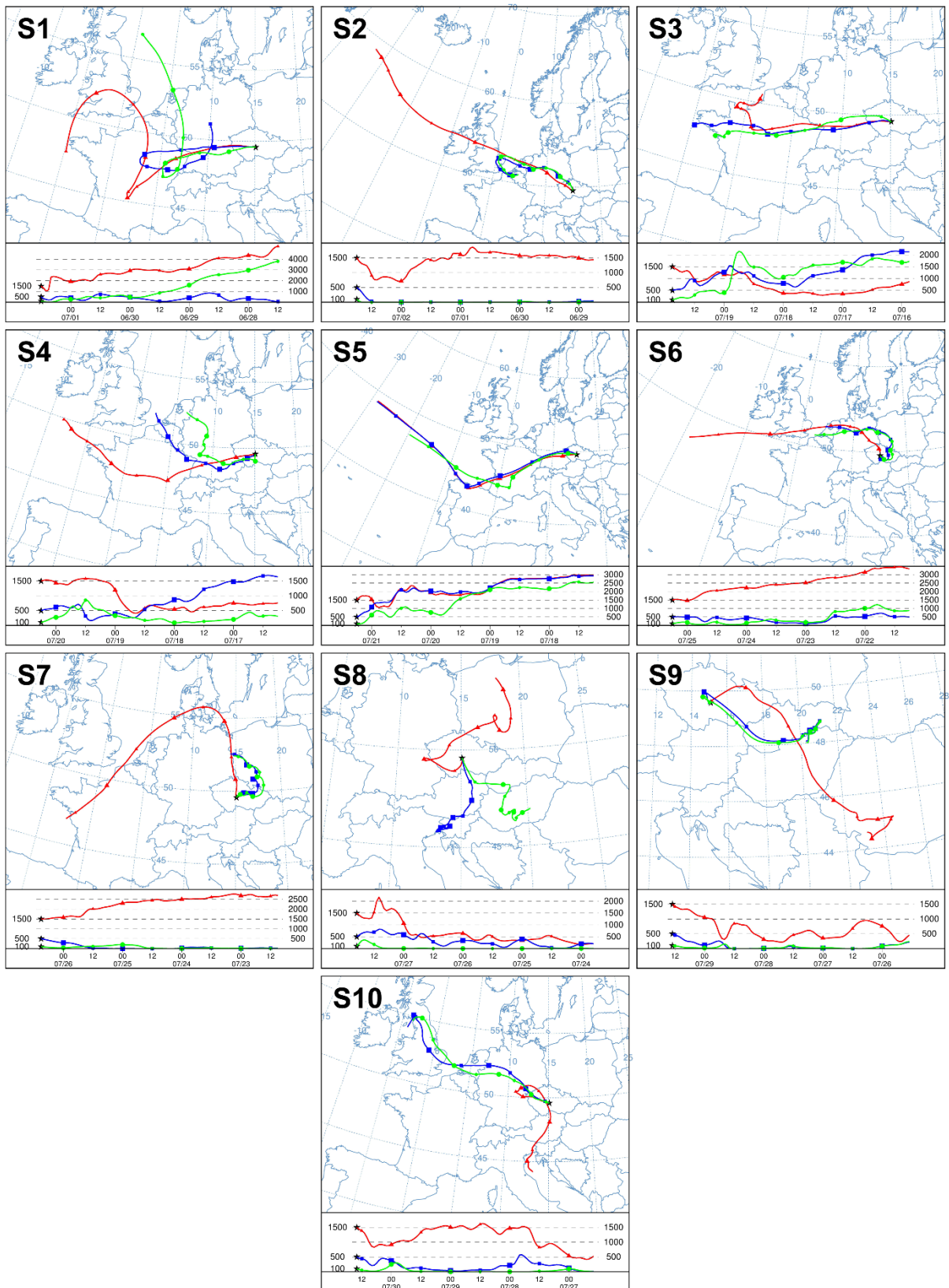
Figure A5. Polar plots showing the origin of organics in summer (left) and winter (right).

Table A1. Overview table presenting mass (M) and median diameter (d) of NR-PM<sub>1</sub> species calculated by fitting log-normal function to the AMS size distributions for the selected episodes in summer (S1 – S10) and winter (W1 – 13) along with meteorology recorded during the episodes (relative humidity – RH, global radiation – GR, temperature – T, wind speed – WS and wind direction – WD)

| Episode | Start            | End              | Duration<br>[h] | M_Org<br>[ug m <sup>-3</sup> ] | M_NO <sub>3</sub> <sup>-</sup><br>[ug m <sup>-3</sup> ] | M_SO <sub>4</sub> <sup>2-</sup><br>[ug m <sup>-3</sup> ] | M_NH <sub>4</sub> <sup>-</sup><br>[ug m <sup>-3</sup> ] | d_Org<br>[nm] | d_NO <sub>3</sub> <sup>-</sup><br>[nm] | d_SO <sub>4</sub> <sup>2-</sup><br>[nm] | d_NH <sub>4</sub> <sup>-</sup><br>[nm] |
|---------|------------------|------------------|-----------------|--------------------------------|---|--|---|---------------|--|---|--|
| S1      | 7.1.19<br>0:00   | 7.1.19<br>12:00  | 12              | 14.58                          | 0.82  | 1.24   | 0.91  | 314           | 285                                    | 414                                     | 498                                    |
| S2      | 7.2.19<br>13:00  | 7.2.19<br>18:00  | 5               | 6.33                           | 0.49  | 4.70   | 1.52  | 307           | 304                                    | 325                                     | 335                                    |
| S3      | 7.19.19<br>15:00 | 7.19.19<br>21:00 | 6               | 6.71                           | 2.00  | 1.84   | 1.15  | 373           | 421                                    | 470                                     | 453                                    |
| S4      | 7.20.19<br>1:00  | 7.20.19<br>6:00  | 5               | 8.41                           | 2.03  | 1.58   | 1.21  | 365           | 388                                    | 467                                     | 466                                    |
| S5      | 7.21.19<br>2:00  | 7.21.19<br>6:00  | 4               | 10.83                          | 1.01  | 1.53   | 0.95  | 358           | 333                                    | 473                                     | 504                                    |
| S6      | 7.24.19<br>21:00 | 7.25.19<br>6:00  | 9               | 8.94                           | 0.97  | 1.59   | 1.07  | 284           | 271                                    | 366                                     | 412                                    |
| S7      | 7.26.19<br>0:00  | 7.26.19<br>9:00  | 9               | 9.25                           | 0.98  | 1.43   | 0.99  | 279           | 253                                    | 382                                     | 454                                    |
| S8      | 7.27.19<br>8:00  | 7.27.19<br>18:59 | 10              | 9.63                           | 1.36  | 3.54   | 1.56  | 399           | 412                                    | 439                                     | 436                                    |
| S9      | 7.28.19<br>15:00 | 7.29.19<br>13:00 | 22              | 6.78                           | 1.16  | 4.49   | 1.76  | 409           | 414                                    | 430                                     | 439                                    |
| S10     | 7.30.19<br>0:00  | 7.30.19<br>14:00 | 14              | 9.57                           | 3.37  | 6.14   | 2.98  | 466           | 491                                    | 494                                     | 478                                    |
| W1      | 1.16.20<br>15:30 | 1.17.20<br>6:00  | 14.5            | 8.60                           | 5.63  | 1.39   | 3.47  | 357           | 378                                    | 447                                     | 392                                    |
| W2      | 1.17.20<br>21:00 | 1.18.20<br>16:00 | 19              | 4.04                           | 5.84  | 1.45   | 3.83  | 356           | 428                                    | 456                                     | 429                                    |
| W3      | 1.21.20<br>13:00 | 1.22.20<br>17:00 | 28              | 9.33                           | 7.50  | 7.13   | 7.90  | 563           | 609                                    | 636                                     | 607                                    |
| W4      | 1.23.20<br>1:00  | 1.23.20<br>8:00  | 7               | 1.90                           | 7.04  | 1.89   | 4.48  | 388           | 386                                    | 487                                     | 410                                    |
| W5      | 1.23.20<br>10:00 | 1.23.20<br>12:00 | 2               | 4.26                           | 7.27  | 3.20   | 5.46  | 357           | 386                                    | 433                                     | 391                                    |
| W6      | 1.23.20<br>14:00 | 1.27.20<br>11:00 | 93              | 7.82                           | 9.40  | 4.18   | 6.76  | 460           | 586                                    | 630                                     | 588                                    |
| W6a     | 1.23.20<br>14:00 | 1.26.20<br>9:00  | 67              | 6.18                           | 10.66   | 4.15   | 7.55  | 523           | 584                                    | 629                                     | 584                                    |
| W6b     | 1.26.20<br>9:30  | 1.27.20<br>11:00 | 25.5            | 13.23                          | 6.37  | 4.34   | 4.89  | 398           | 571                                    | 625                                     | 593                                    |
| W7      | 2.1.20<br>7:30   | 2.1.20<br>9:00   | 1.5             | 15.63                          | 0.93  | 0.74   | 0.96  | 336           | 276                                    | 241                                     | 390                                    |
| W8      | 2.1.20<br>12:00  | 2.1.20<br>14:00  | 2               | 10.32                          | 0.72  | 0.62   | 0.90  | 295           | 240                                    | 242                                     | 365                                    |
| W9      | 2.2.20<br>6:00   | 2.2.20<br>7:30   | 1.5             | 10.12                          | 0.17  | 0.41   | 0.76  | 296           | 787                                    | 287                                     | 392                                    |
| W10     | 2.6.20<br>10:00  | 2.6.20<br>18:00  | 8               | 2.15                           | 2.66  | 4.19   | 3.35  | 385           | 479                                    | 473                                     | 462                                    |
| W11     | 2.7.20<br>16:00  | 2.8.20<br>1:30   | 9.5             | 5.76                           | 5.09  | 2.50   | 3.30  | 366           | 419                                    | 488                                     | 446                                    |
| W12     | 2.8.20<br>9:30   | 2.8.20<br>12:00  | 2.5             | 6.52                           | 5.23  | 2.27   | 3.06  | 387           | 461                                    | 523                                     | 478                                    |
| W13     | 2.8.20<br>13:00  | 2.9.20<br>0:30   | 11.5            | 7.72                           | 8.12  | 1.93   | 4.35  | 379           | 436                                    | 498                                     | 451                                    |
| Episode | Start            | End              | Duration<br>[h] | RH [%]                         | GR<br>[W m <sup>-2</sup> ]                              | T [°C]   | WS<br>[m s <sup>-1</sup> ]                              | WD            |  |   |  |
| S1      | 7.1.19<br>0:00   | 7.1.19<br>12:00  | 12              | 49                             | 318   | 25.8   | 3.7   | W-SW          |  |   |  |
| S2      | 7.2.19<br>13:00  | 7.2.19<br>18:00  | 5               | 44                             | 566   | 22.8   | 3.7   | N-NNW         |  |   |  |
| S3      | 7.19.19<br>15:00 | 7.19.19<br>21:00 | 6               | 91                             | 92  | 17.3   | 1.5   | S-SE-W        |  |   |  |
| S4      | 7.20.19<br>1:00  | 7.20.19<br>6:00  | 5               | 97                             | 28  | 14.9   | 1.3   | SE            |  |   |  |
| S5      | 7.21.19<br>2:00  | 7.21.19<br>6:00  | 4               | 68                             | 31  | 19.7   | 2.5   | SW-NW         |  |   |  |



|     |                  |                  |      |    |     |      |     |                                  |
|-----|------------------|------------------|------|----|-----|------|-----|----------------------------------|
| S6  | 7.24.19<br>21:00 | 7.25.19<br>6:00  | 9    | 68 | 13  | 18.2 | 1.2 | SW-SE                            |
| S7  | 7.26.19<br>0:00  | 7.26.19<br>9:00  | 9    | 59 | 148 | 19.1 | 2.3 | W                                |
| S8  | 7.27.19<br>8:00  | 7.27.19<br>18:59 | 10   | 75 | 297 | 21.3 | 3.4 | SE                               |
| S9  | 7.28.19<br>15:00 | 7.29.19<br>13:00 | 22   | 81 | 156 | 20.5 | 2.4 | W-NW-SE                          |
| S10 | 7.30.19<br>0:00  | 7.30.19<br>14:00 | 14   | 81 | 196 | 20.9 | 3.7 | W                                |
| W1  | 1.16.20<br>15:30 | 1.17.20<br>6:00  | 14.5 | 92 | 3   | 1.1  | 2.1 | SE                               |
| W2  | 1.17.20<br>21:00 | 1.18.20<br>16:00 | 19   | 96 | 13  | 0.4  | 2.0 | SE-NW                            |
| W3  | 1.21.20<br>13:00 | 1.22.20<br>17:00 | 28   | 93 | 77  | -3.8 | 2.5 | <del>W</del> -NW-SE <del>W</del> |
| W4  | 1.23.20<br>1:00  | 1.23.20<br>8:00  | 7    | 88 | 0   | 0.1  | 1.7 | W-NW                             |
| W5  | 1.23.20<br>10:00 | 1.23.20<br>12:00 | 2    | 73 | 120 | 0.6  | 1.9 | SE                               |
| W6  | 1.23.20<br>14:00 | 1.27.20<br>11:00 | 93   | 93 | 34  | -1.1 | 1.7 | SE-S-SW                          |
| W6a | 1.23.20<br>14:00 | 1.26.20<br>9:00  | 67   | 94 | 20  | -2.4 | 2.0 | SE-S                             |
| W6b | 1.26.20<br>9:30  | 1.27.20<br>11:00 | 25.5 | 98 | 43  | -1.0 | 1.1 | SE                               |
| W7  | 2.1.20<br>7:30   | 2.1.20<br>9:00   | 1.5  | 77 | 22  | 9.2  | 3.9 | SW                               |
| W8  | 2.1.20<br>12:00  | 2.1.20<br>14:00  | 2    | 69 | 201 | 11.9 | 7.5 | SW                               |
| W9  | 2.2.20<br>6:00   | 2.2.20<br>7:30   | 1.5  | 75 | 0   | 4.1  | 8.1 | W                                |
| W10 | 2.6.20<br>10:00  | 2.6.20<br>18:00  | 8    | 76 | 112 | 0.4  | 6.0 | W-NW                             |
| W11 | 2.7.20<br>16:00  | 2.8.20<br>1:30   | 9.5  | 92 | 4   | 0.9  | 1.5 | SE                               |
| W12 | 2.8.20<br>9:30   | 2.8.20<br>12:00  | 2.5  | 85 | 237 | 0.8  | 3.9 | SE                               |
| W13 | 2.8.20<br>13:00  | 2.9.20<br>0:30   | 11.5 | 84 | 86  | 0.6  | 2.7 | <del>SW</del> -SE                |



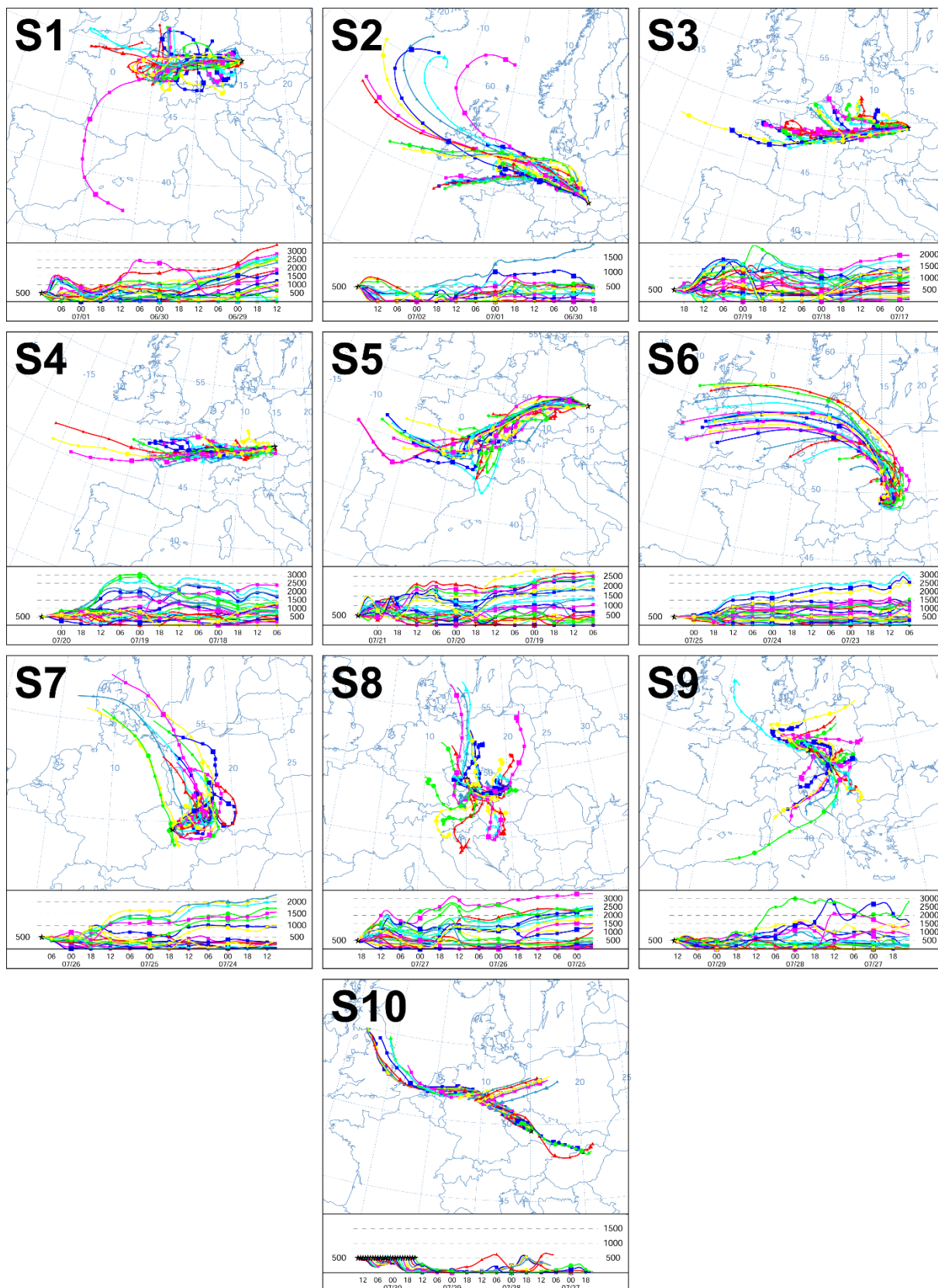
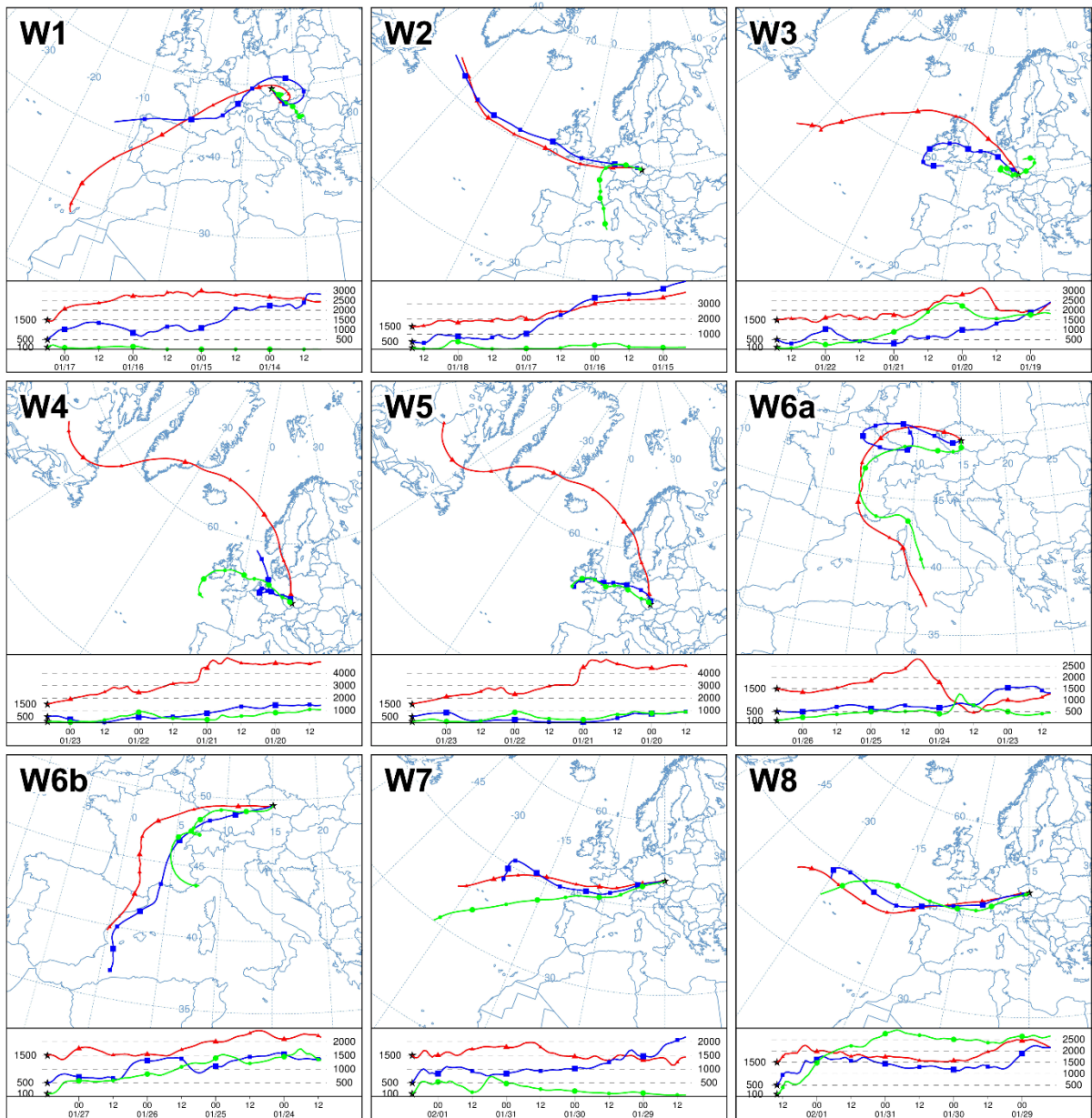


Figure A6A5. Backward air mass trajectories calculated by HYSPLIT for corresponding summer episodes (S1 – S10) of high concentration of species size distributions.





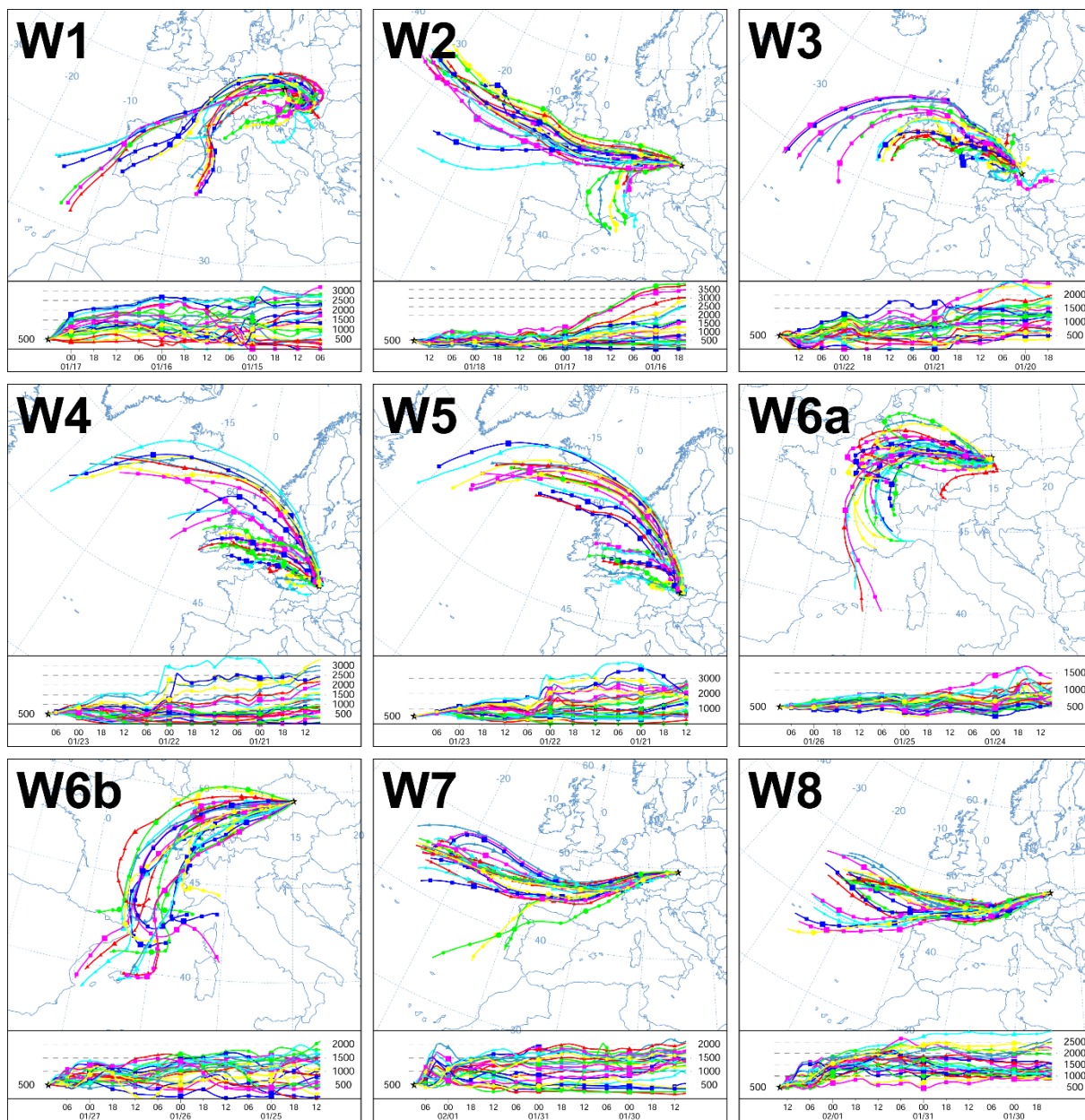


Figure continues.



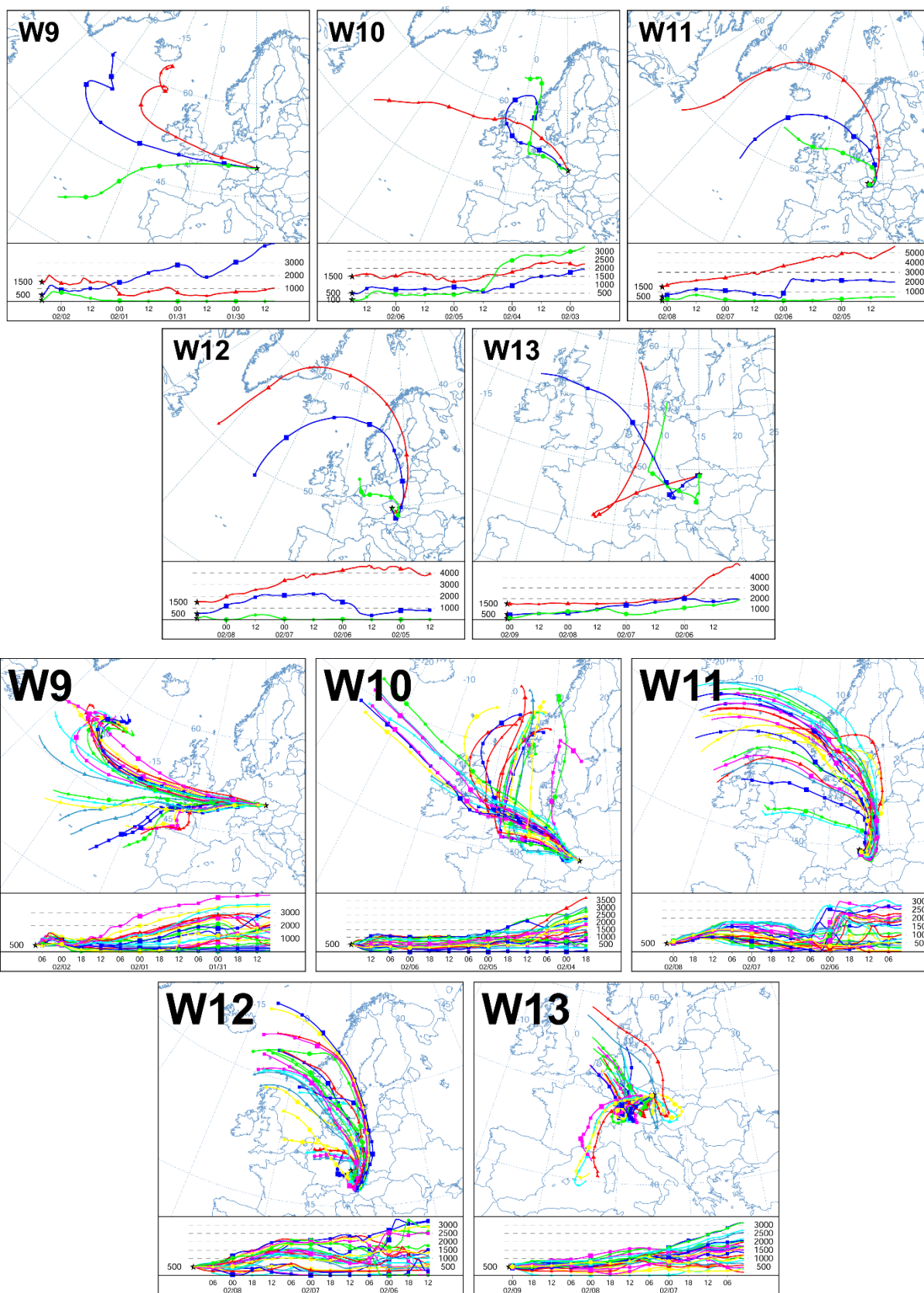
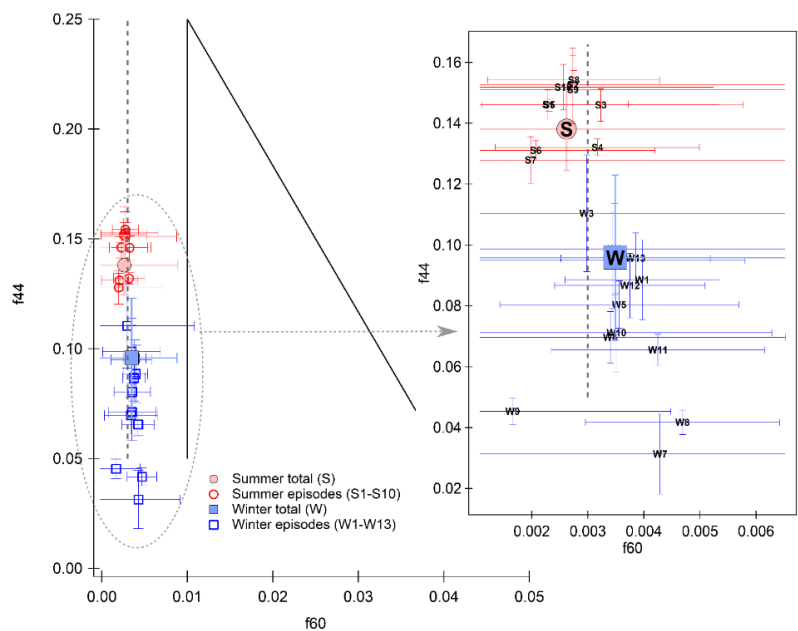


Figure A7A6. Backward air mass trajectories calculated by HYSPLIT for corresponding winter episodes (W1 – W13) of high concentration of species size distributions.

1114  
1115  
1116  
1117



1118  
1119  
1120  
1121  
1122  
1123

Figure A8A7. Comparison of organic fragments  $f_{44}$  and  $f_{60}$  for the whole campaigns (full markers) and for the specific episodes (empty markers). Bars represent standard deviation and the triangular space area of biomass burning (BB) influence and dashed line a limit for a negligible fresh BB influence (Cubison et al., 2011).

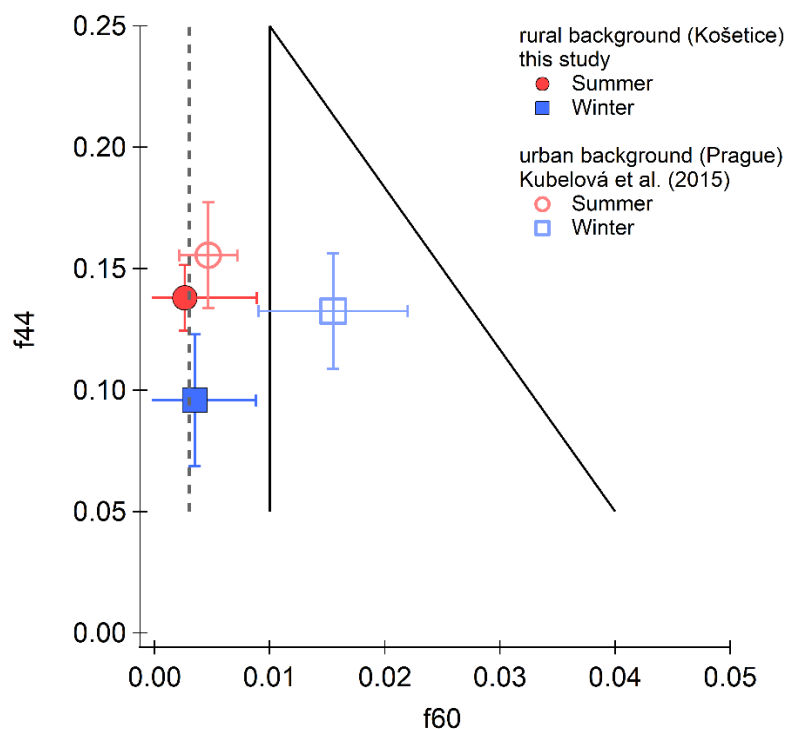
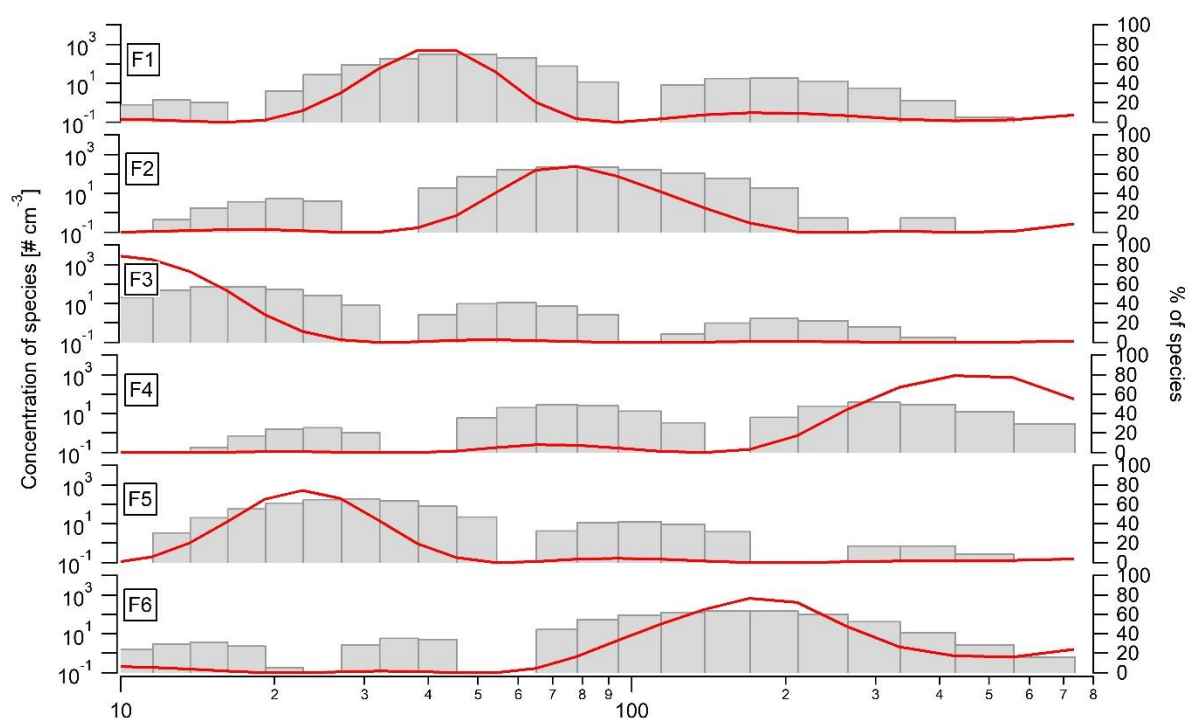


Figure A9A8. Comparison of organic fragments  $f_{44}$  and  $f_{60}$  determined at rural background site (NAOK) and urban background site (Prague, study by Kubelová et al., 2015) during summer and winter seasons.



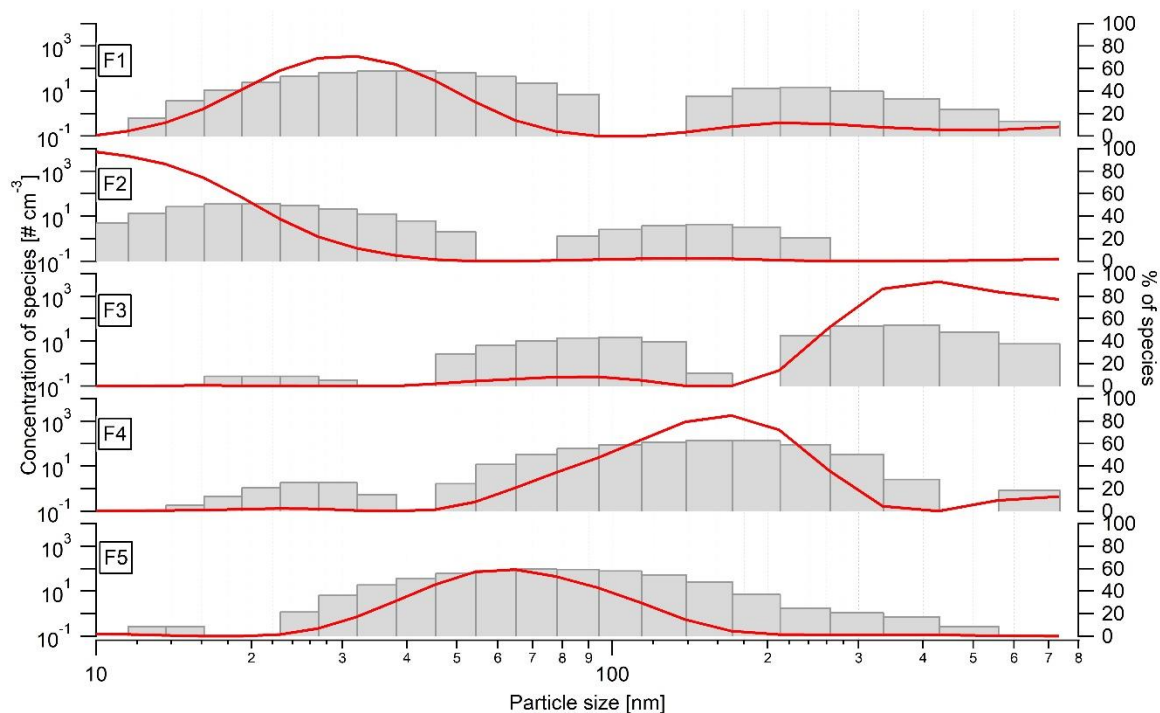
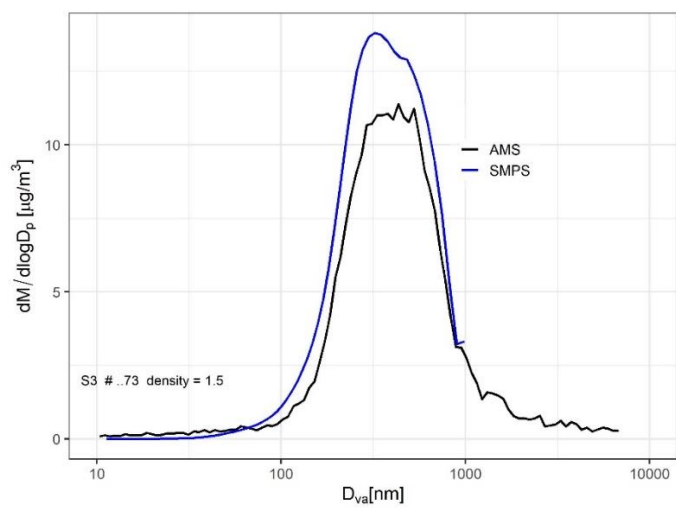
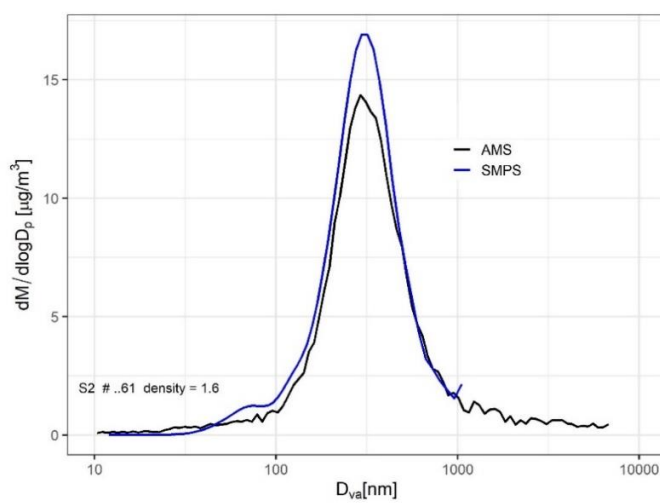
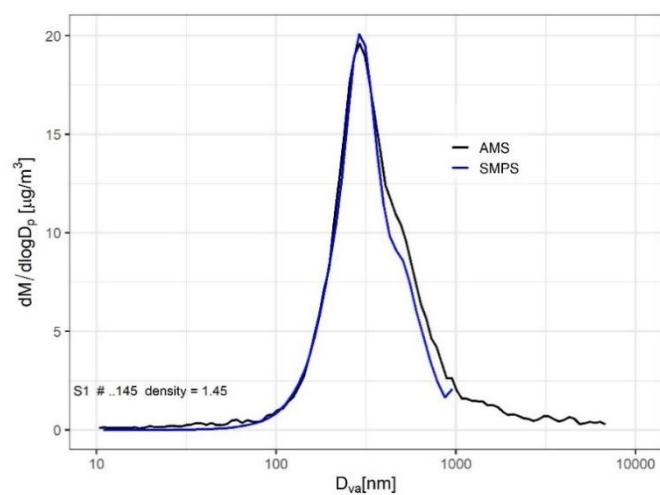


Figure A10A9. PNSD factor profiles for summer (top) and winter (bottom) campaign. The bars represent the number size distribution (y axis on the left), and the lines represent the contribution as a percentage (y axis on the right).

Table A2. Summary of PMF diagnostics for PNSD.

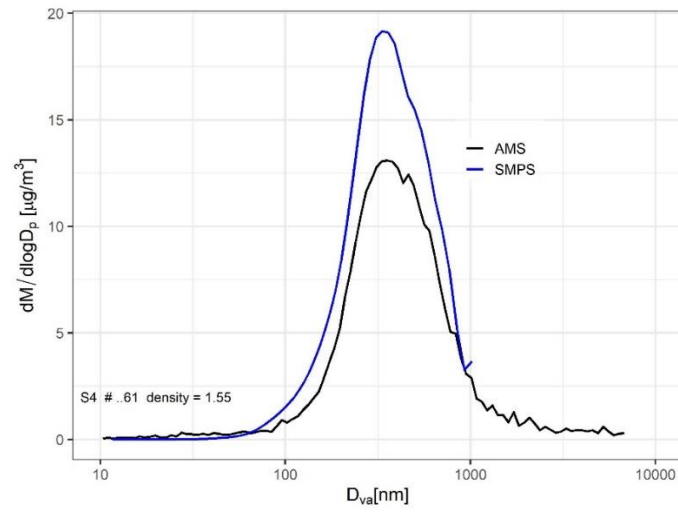
| Diagnostic                               | Summer | Winter |
|--|--------|--------|
| N. of observations                       | 8684   | 7414   |
| Missing values                           | 6.8%   | 0%     |
| Number of factors                        | 6      | 5      |
| $Q_{\text{expected}}$                    | 161224 | 103701 |
| $Q_{\text{true}}$                        | 129774 | 102925 |
| $Q_{\text{robust}}$                      | 130657 | 103495 |
| Species with $Q/Q_{\text{expected}} > 2$ | 0      | 263    |
| Extra modelling uncertainty              | 4.8%   | 4.0%   |
| DISP-swaps                               | 0      | 0      |
| BS-mapping                               | 100%   | 100%   |



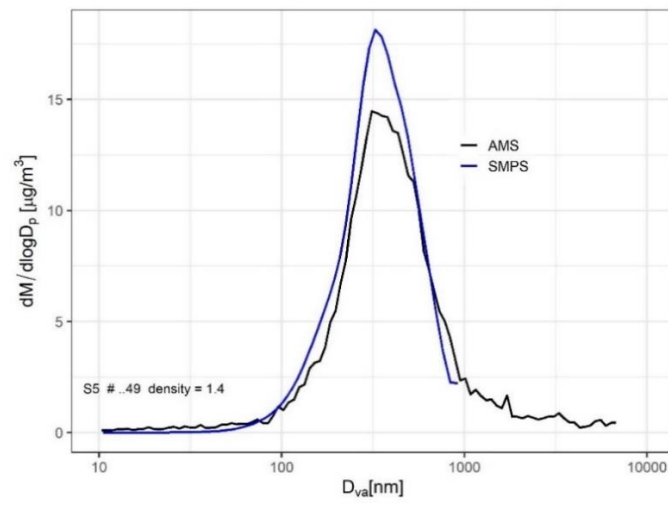
1140

1141

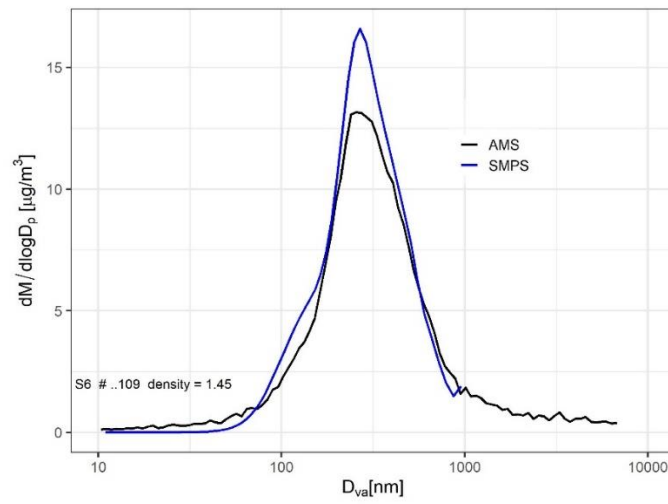




1142

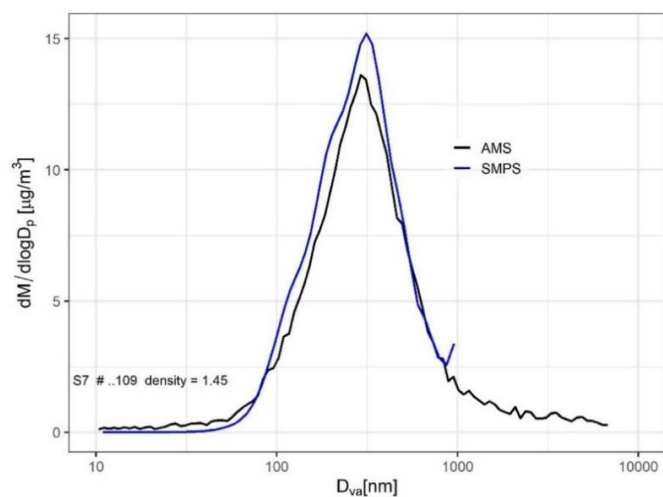


1143

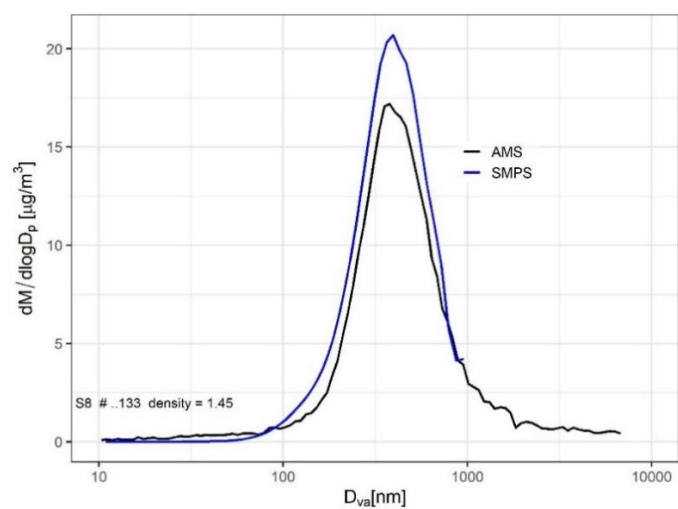


1144

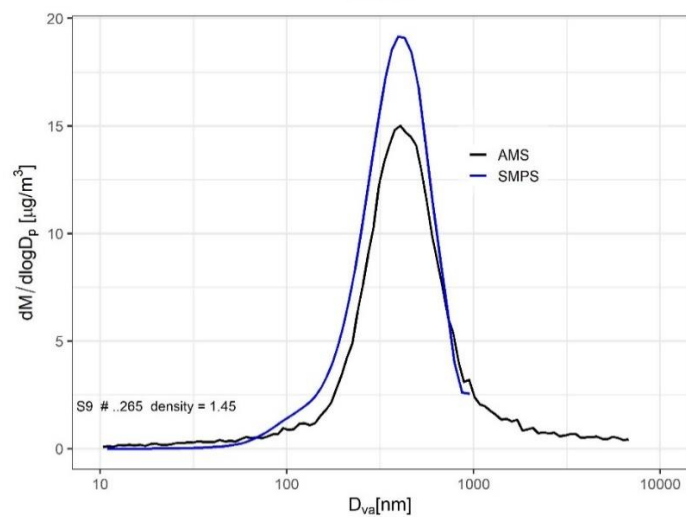
1145

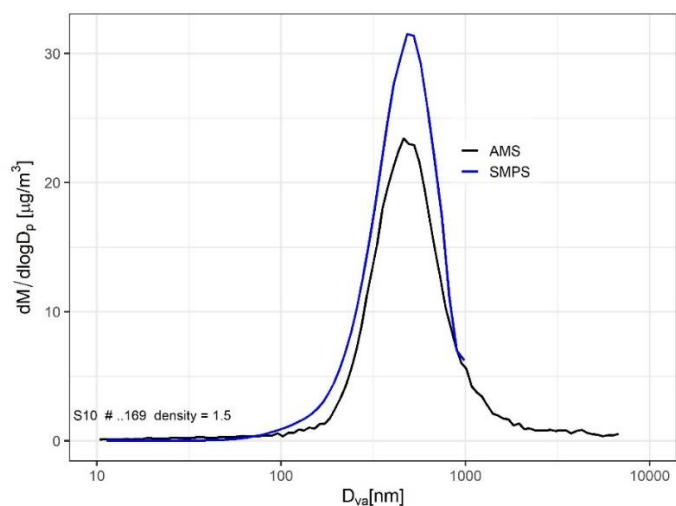


1146



1147

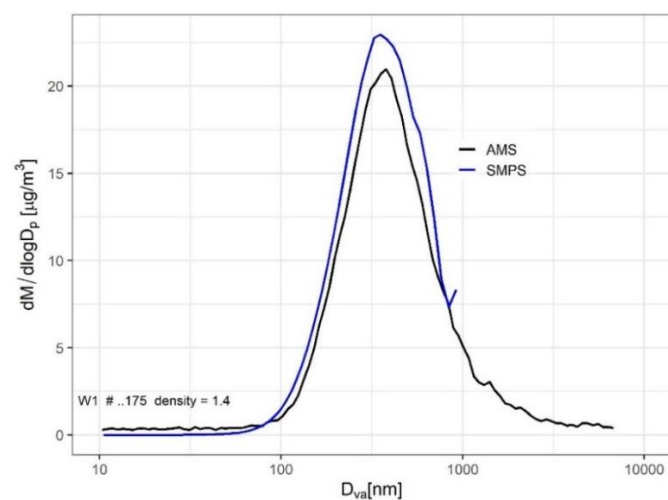




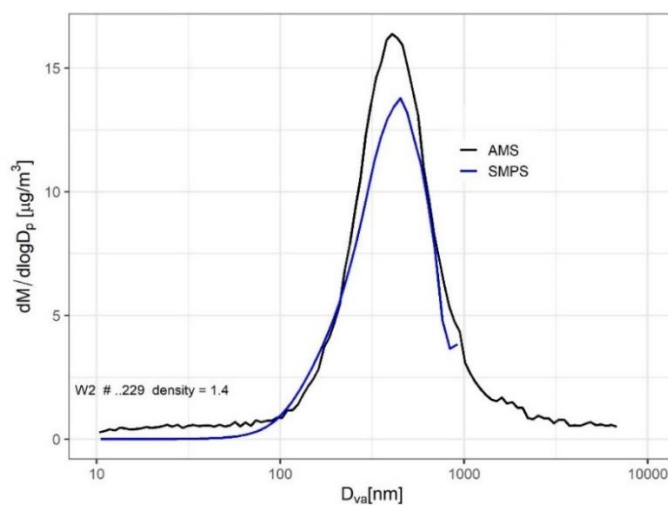
1148

1149

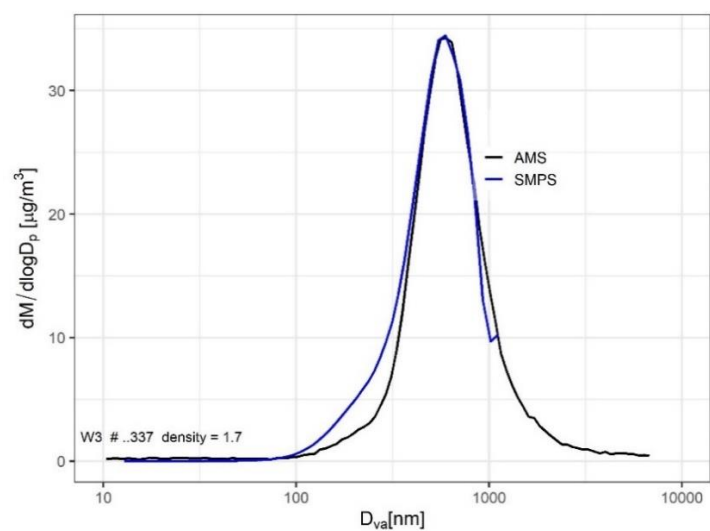
1150 Figure A11A910. Fit of AMS and MPSS mass size distribution spectra of summer episodes  
 1151 (S1 – S10) for density calculation.



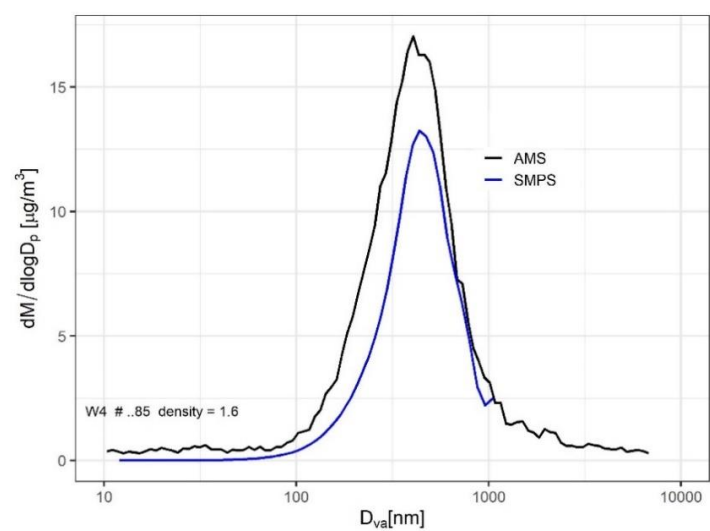
1152



1153

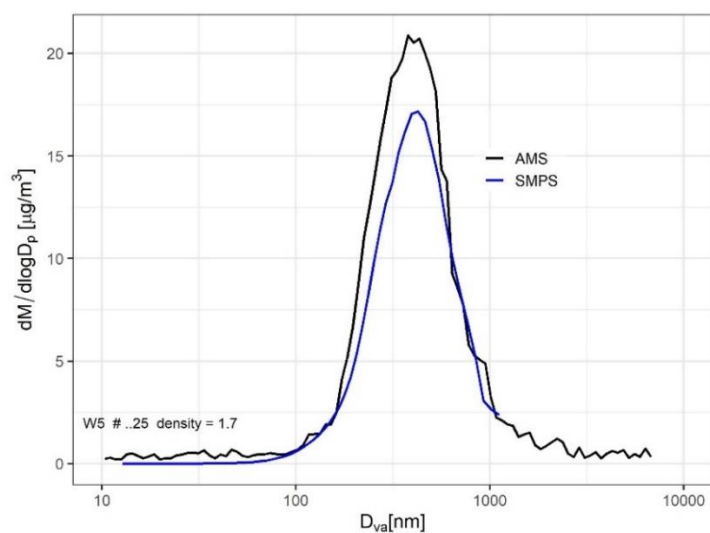


1154

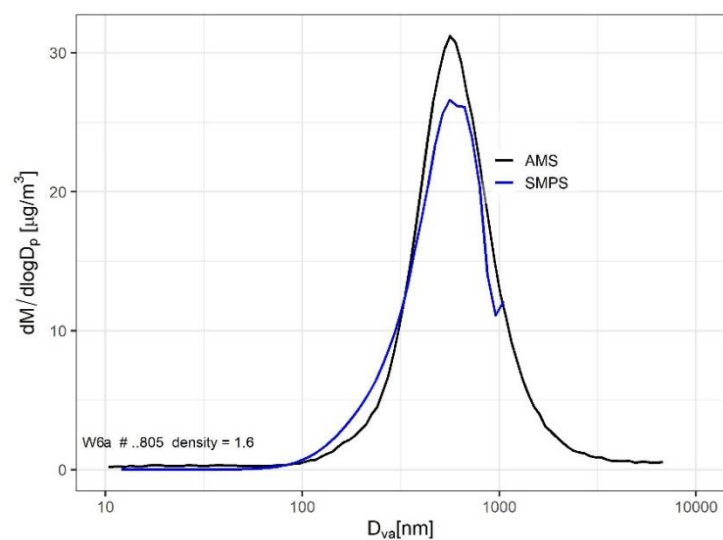


1155

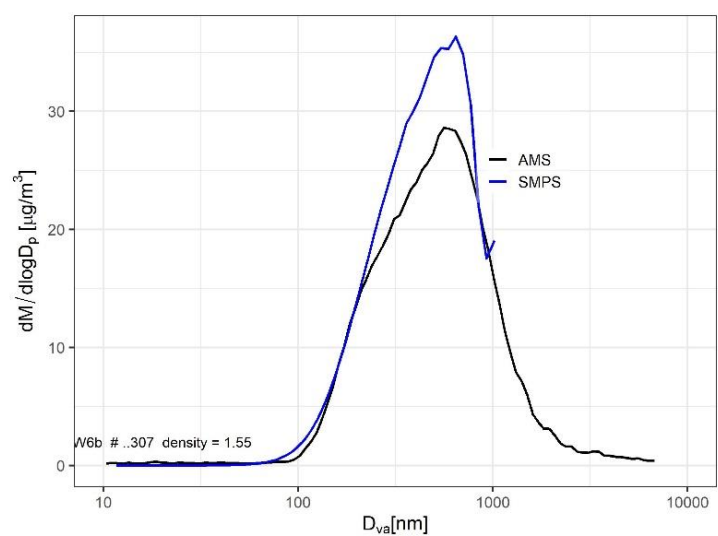
1156



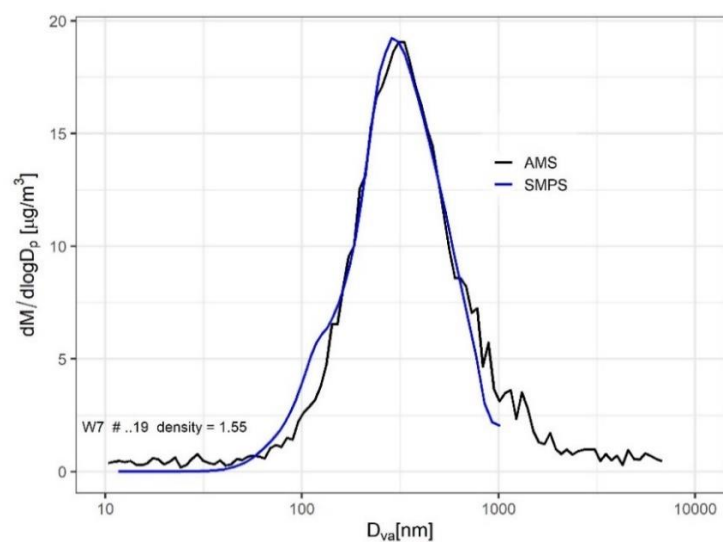
1157



1158

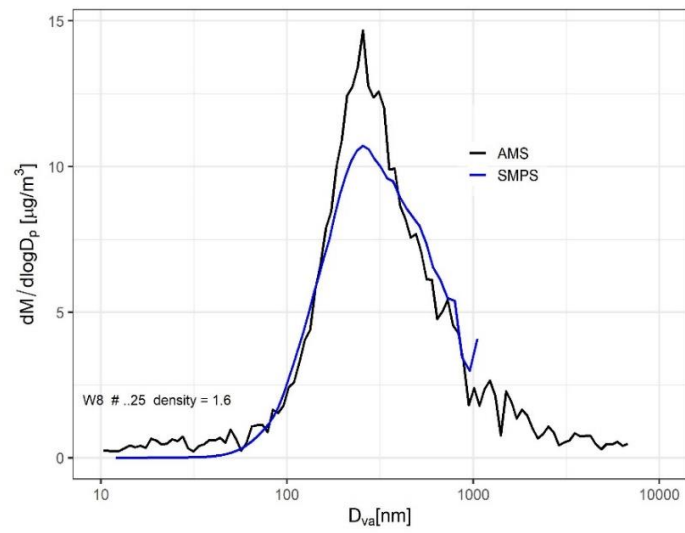


1159

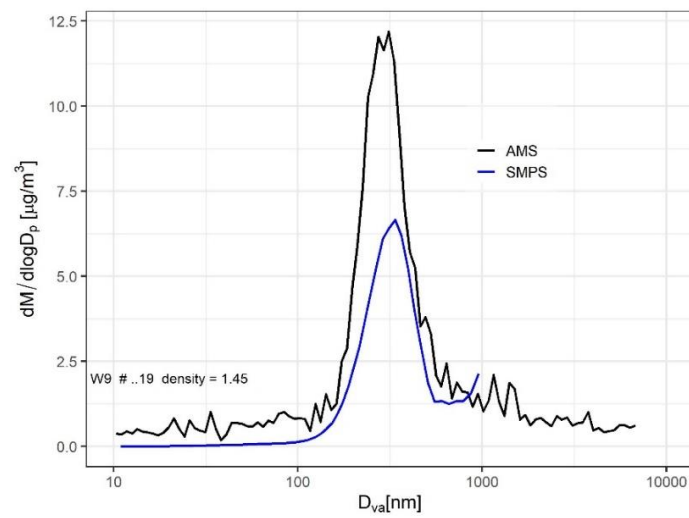


1160

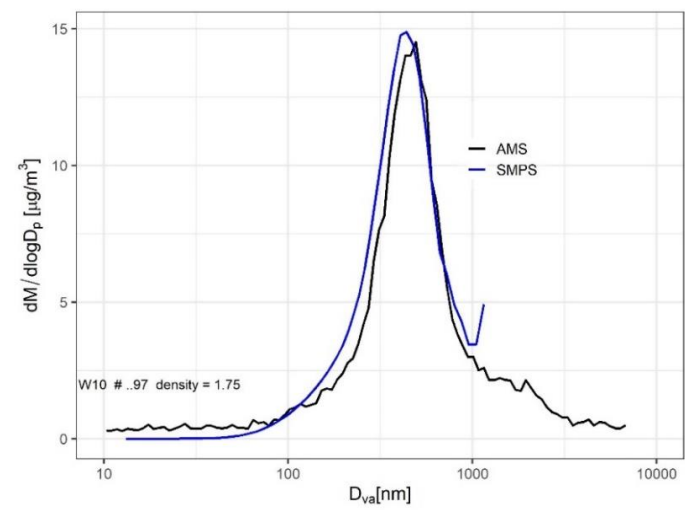




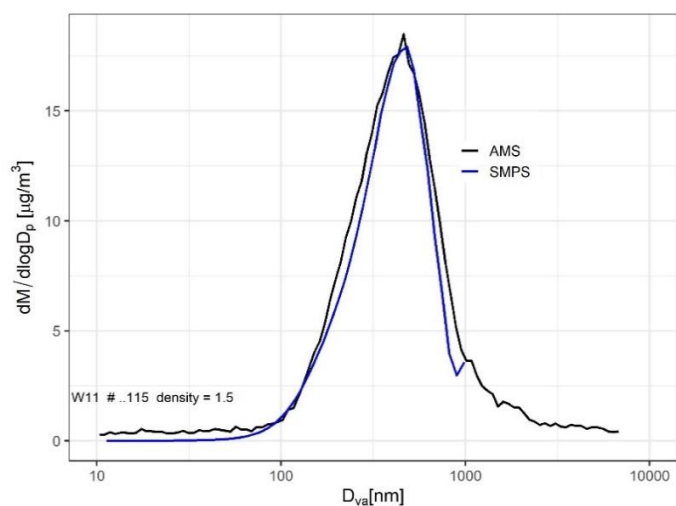
1161



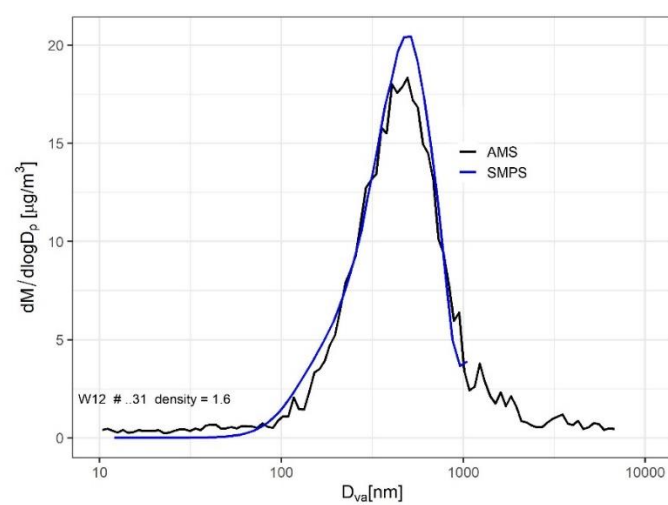
1162



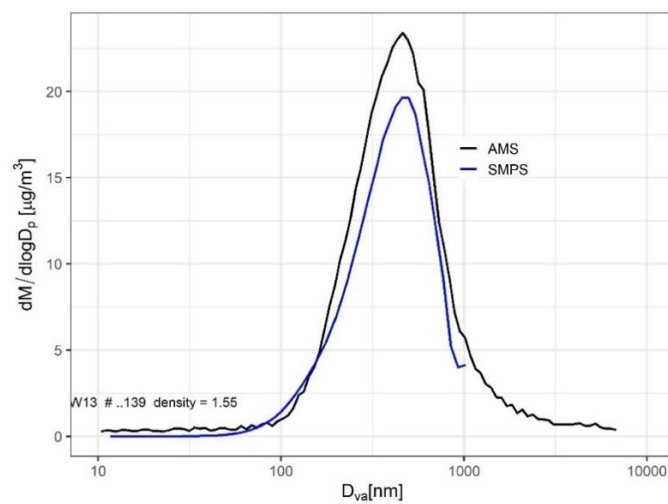
1163



1164



1165



1166

1167

1168 Figure [A12A101](#). Fit of AMS and MPSS mass size distribution spectra of winter episodes (W1  
1169 – W13) for density calculation.

1170

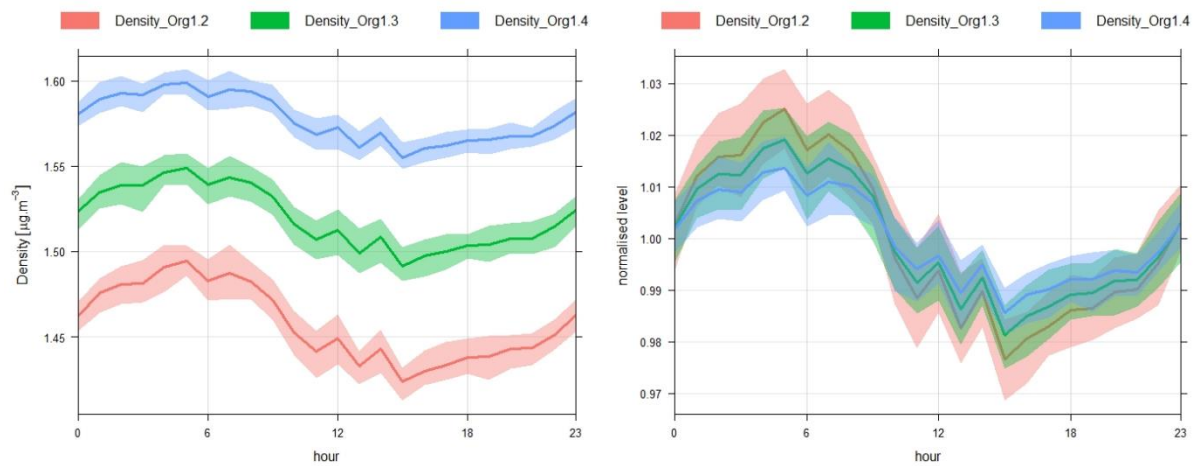


Fig. A11. Diurnal trends of average  $\rho_m$  calculated based on Eq. (2) in winter for different organic densities (1.2, 1.3 and 1.4 g cm<sup>-3</sup>) in absolute (left) and normalized (right) values.

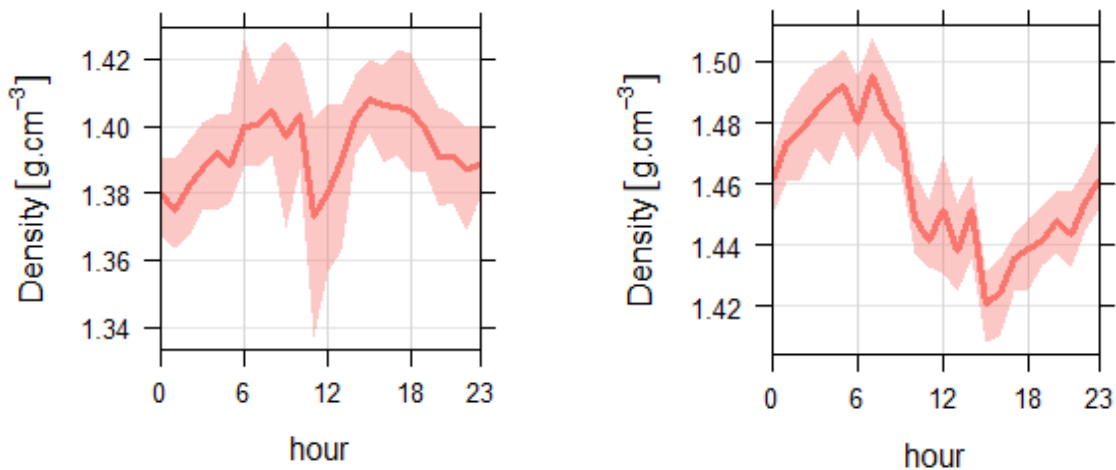


Figure A13. Diurnal trends of average effective particle density calculated based on Eq. (2) in the main text from Salcedo et al., 2006 in summer (left) and winter (right).

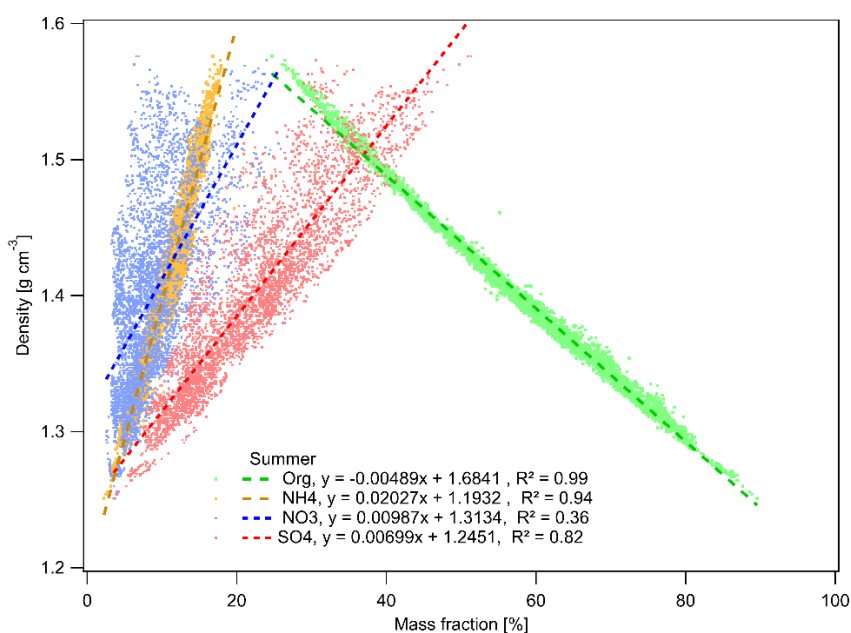
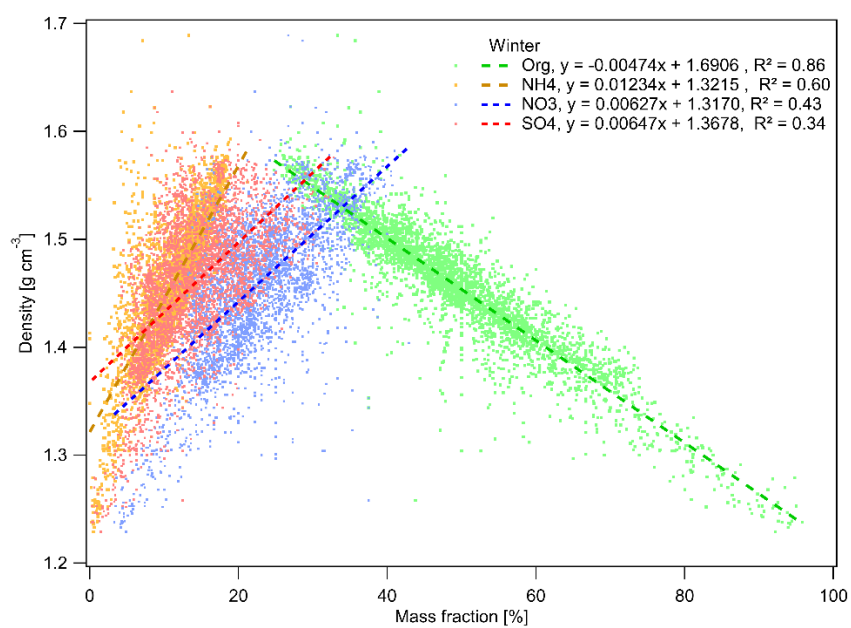


Figure A14. Relationship between density, calculated according to Eq., and mass fractions of the main NR-PM<sub>1</sub> species.

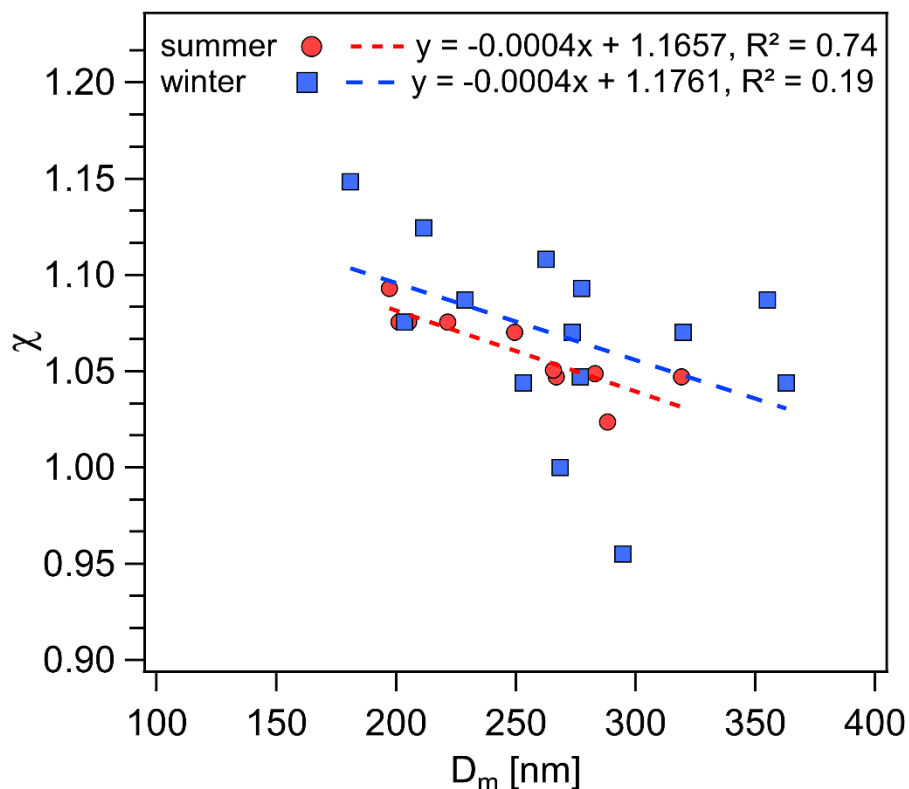


Figure A11. Calculated variation of the mobility diameter ( $D_m$ ) as a function of the dynamic shape factor ( $\chi$ ) for the summer and winter episodes of high mass concentrations.

### A1. Positive Matrix Factorization on PNSD

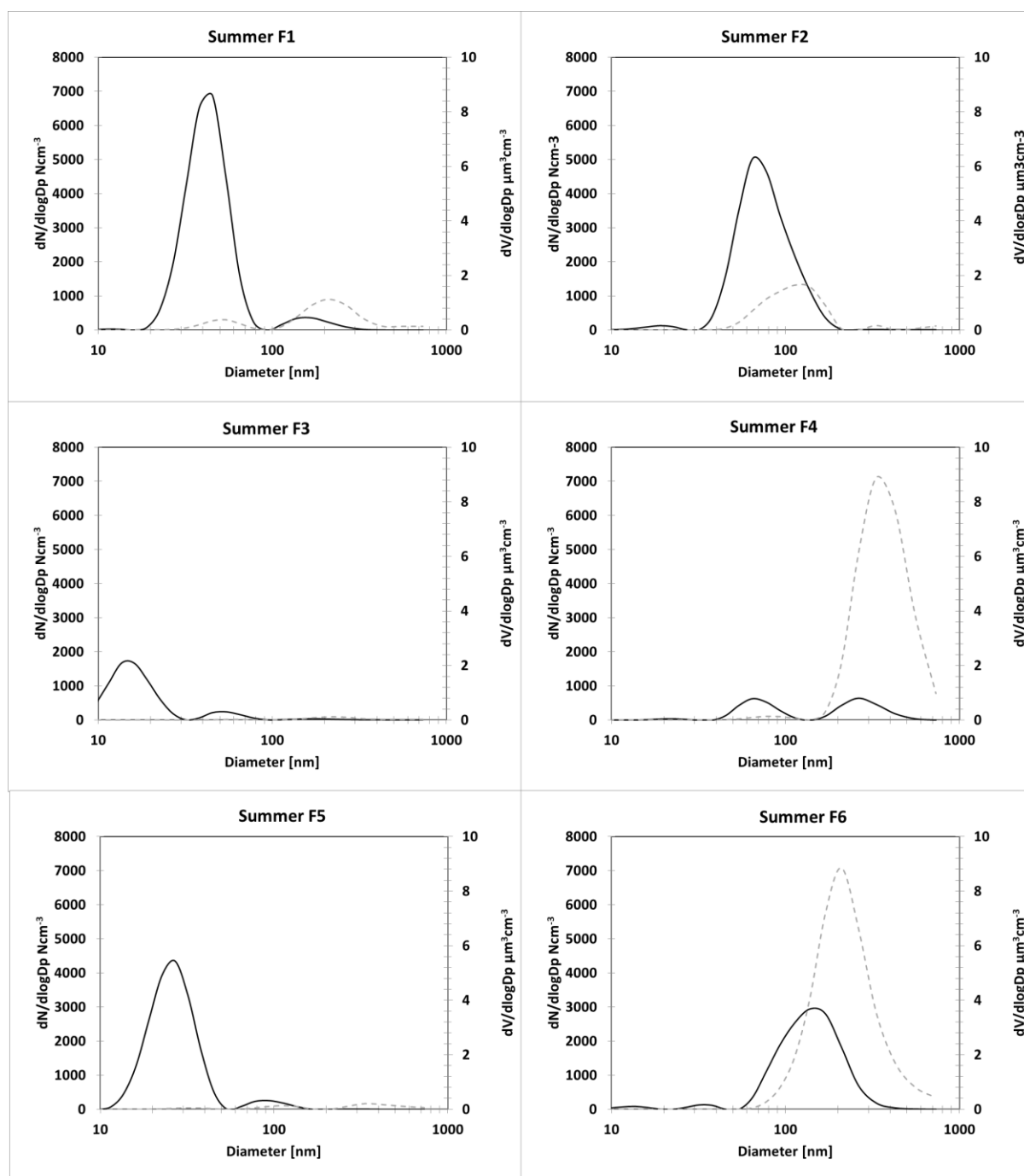
PMF (US EPA, version PMF 5.0) was applied to the seasonal 5-min PNSDs in the range from 10 nm to 800 nm to estimate the number and profile of the PNSD factors and their contributions to the receptor. Application of PMF on PNSD is commonly adopted in source apportionment studies since by investigating particles in various size ranges, it is possible to more clearly identify and apportion contributions from those sources that contributed more to the particle number than to the particle mass (e.g. Beddows et al., 2015; Masiol et al., 2016; Sowlat et al., 2016; Leoni et al., 2018; Pokorná et al., 2020; Zíková et al., 2020). Episodes in which the factor contributions to the total particle number concentrations were higher than 80 % were chosen for the subsequent particle density calculations.

The input data were prepared by merging three consecutive bins to reduce the noise in the raw data, decrease the number of variables, and reduce the number of zeroes in the raw data (Leoni et al., 2018). The uncertainties were calculated according to Vu et al. (2015). The total variables were calculated by summing all the bins (N10 – 800). PMF was conducted using different uncertainty input matrices and different C3 (Vu et al., 2015) to obtain the  $Q_{true}$  closest to  $Q_{expected}$ ; different modelling uncertainties and different numbers of factors were also applied. A C3 of 0.8 was chosen.

The PMF model was run several times until the most physically meaningful results (factor profiles, contributions to N10-800 and origin) and the best diagnostics were obtained. The four (9.7 nm, 11.5 nm, 557.2 nm and 733.6 nm; midpoint of the merged three consecutive size bins)

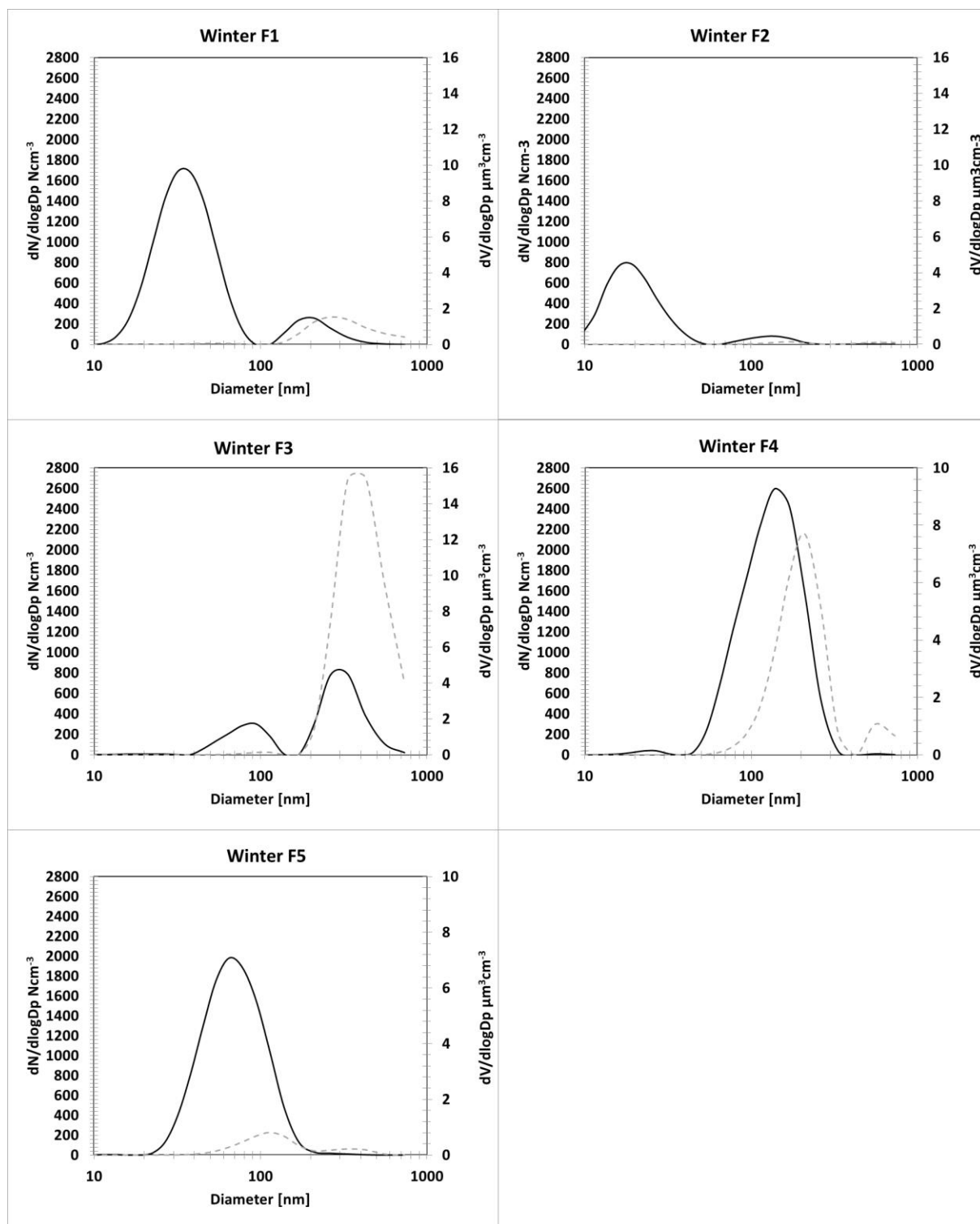


were set as weak along with the total variable ( $N_{10} = 800$ ). The model was run with different factor numbers (3 – 8). The most stable solution was found when 6 factors in summer and 5 factors in winter were considered (Fig. A122). With all runs converged, the scaled residuals were normally distributed, and any unmapped factors were detected with bootstrap error estimations. No swaps were observed with the displacement error analysis, indicating that the solution was stable (Table A2). The non-normalized PNSD ( $N\text{ cm}^{-3}$ ) was analysed using the model.



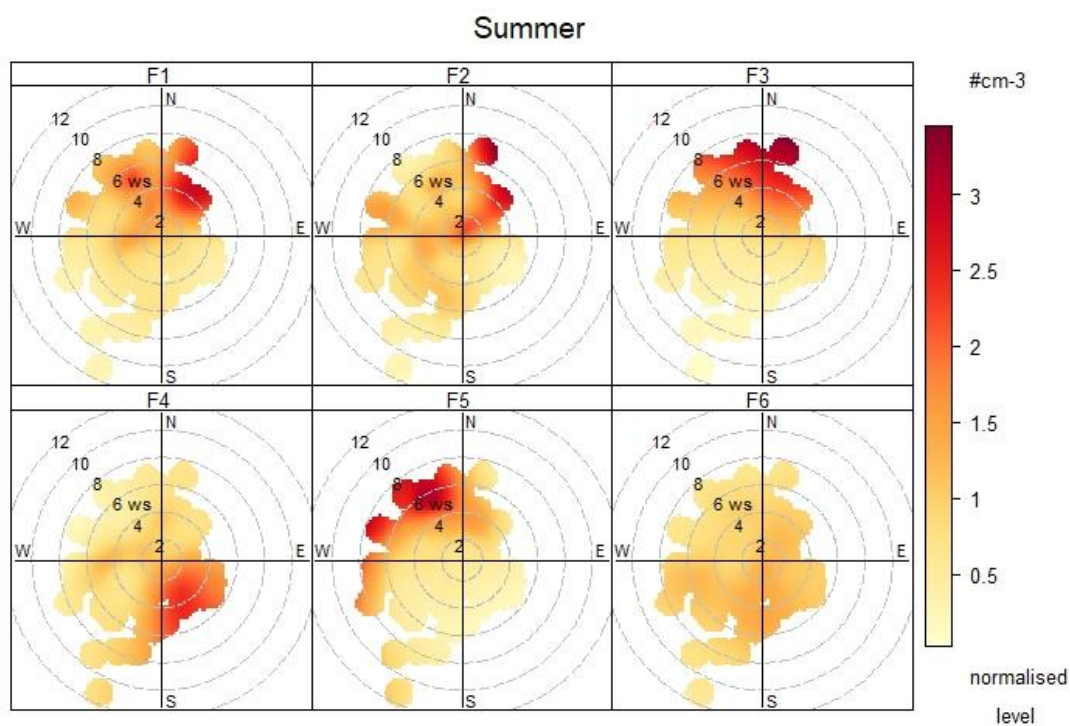
1228

1229

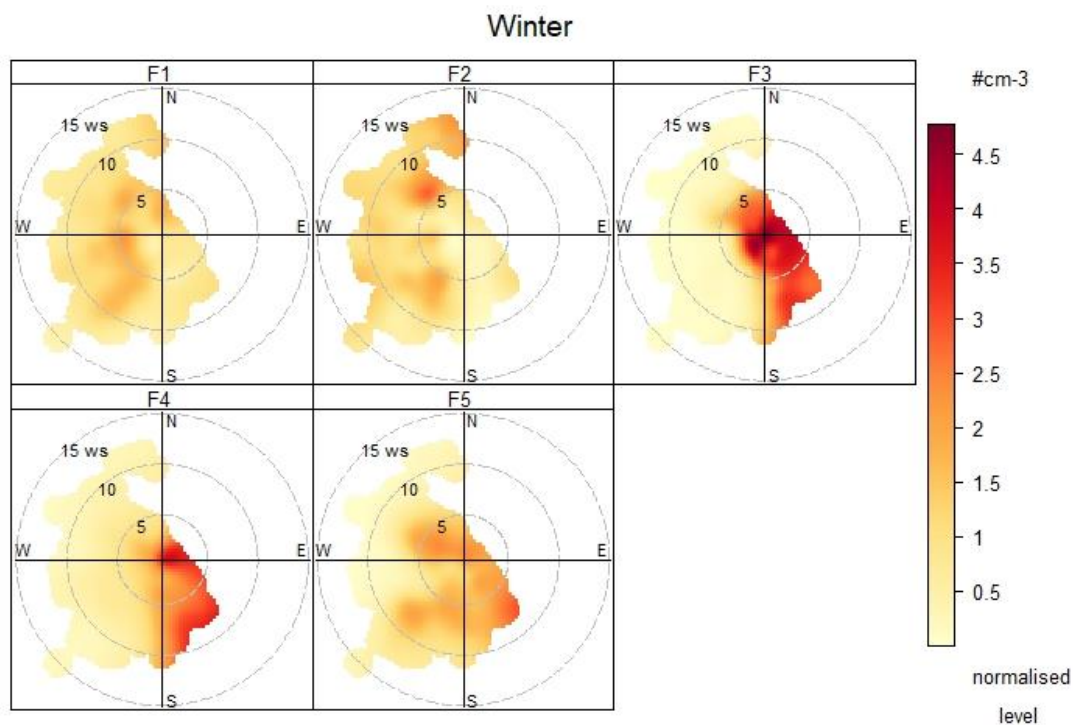


1230

1231 Figure A122. PNSD factor profiles for summer (top) and winter (bottom) campaign. NSD  
 1232 (black line, y-axis on the left), volume size distribution (grey dashed line, y-axis on the right).  
 1233 The volume size distribution was re-calculated from the NSD assuming spherical particles.



1234



1235

1236 Figure A13. Polar plot with factors concentrations (1-h vector averaged WS and WD) for  
 1237 summer (top) and winter (bottom).

Table A2. Summary of PMF diagnostics for PNSD.

| <u>Diagnostic</u>                              | <u>Summer</u> | <u>Winter</u> |
|--|---------------|---------------|
| <u>N. of observations</u>                      | <u>8684</u>   | <u>7414</u>   |
| <u>Missing values</u>                          | <u>6.8%</u>   | <u>0%</u>     |
| <u>Number of factors</u>                       | <u>6</u>      | <u>5</u>      |
| <u>Q<sub>expected</sub></u>                    | <u>161224</u> | <u>103701</u> |
| <u>Q<sub>true</sub></u>                        | <u>129774</u> | <u>102925</u> |
| <u>Q<sub>robust</sub></u>                      | <u>130657</u> | <u>103495</u> |
| <u>Species with Q/Q<sub>expected</sub> ≥ 2</u> | <u>0</u>      | <u>263</u>    |
| <u>Extra modelling uncertainty</u>             | <u>4.8%</u>   | <u>4.0%</u>   |
| <u>DISP swaps</u>                              | <u>0</u>      | <u>0</u>      |
| <u>BS mapping</u>                              | <u>100%</u>   | <u>100%</u>   |

Table A3. Overview table presenting median diameter (d) of N10-800 calculated by fitting log-normal function to the MPSS size distributions for the selected episodes (N\_W1 – N\_W8) along with meteorology recorded during the episodes (relative humidity – RH, global radiation – GR, temperature – T, wind speed – WS and wind direction – WD)

| <u>Episode</u> | <u>Start</u>         | <u>End</u>           | <u>Duration</u><br><u>[min]</u> | <u>d<sub>N10-800</sub></u><br><u>[nm]</u> | <u>RH [%]</u> | <u>GR</u><br><u>[W m<sup>-2</sup>]</u> | <u>T [°C]</u> | <u>WS</u><br><u>[m s<sup>-1</sup>]</u> | <u>WD</u><br><u>[°]</u> |
|----------------|----------------------|----------------------|---------------------------------|---|---------------|--|---------------|--|-------------------------|
| <u>N_W1</u>    | <u>1.22.20 3:00</u>  | <u>1.22.20 4:00</u>  | <u>60</u>                       | <u>623</u>                                | <u>96.6</u>   | <u>0</u>                               | <u>-5.8</u>   | <u>2.2</u>                             | <u>SE</u>               |
| <u>N_W2</u>    | <u>1.28.20 23:35</u> | <u>1.29.20 00:10</u> | <u>35</u>                       | <u>265</u>                                | <u>74.2</u>   | <u>0</u>                               | <u>1.3</u>    | <u>7.1</u>                             | <u>SW</u>               |
| <u>N_W3</u>    | <u>1.29.20 00:30</u> | <u>1.29.20 01:05</u> | <u>35</u>                       | <u>283</u>                                | <u>83.6</u>   | <u>0</u>                               | <u>0.2</u>    | <u>7.1</u>                             | <u>SW</u>               |
| <u>N_W4</u>    | <u>1.29.20 07:25</u> | <u>1.29.20 08:55</u> | <u>90</u>                       | <u>300</u>                                | <u>82.3</u>   | <u>10</u>                              | <u>-0.4</u>   | <u>6.0</u>                             | <u>S</u>                |
| <u>N_W5</u>    | <u>1.30.20 01:30</u> | <u>1.30.20 02:00</u> | <u>30</u>                       | <u>269</u>                                | <u>81.3</u>   | <u>0</u>                               | <u>0.3</u>    | <u>7.6</u>                             | <u>W</u>                |
| <u>N_W6</u>    | <u>1.30.20 05:35</u> | <u>1.30.20 05:55</u> | <u>20</u>                       | <u>356</u>                                | <u>84.0</u>   | <u>0</u>                               | <u>-0.2</u>   | <u>5.7</u>                             | <u>SW</u>               |
| <u>N_W7</u>    | <u>2.2.20 19:00</u>  | <u>2.2.20 19:30</u>  | <u>30</u>                       | <u>261</u>                                | <u>90.8</u>   | <u>0</u>                               | <u>9.0</u>    | <u>8.8</u>                             | <u>SW-W</u>             |
| <u>N_W8</u>    | <u>2.5.20 00:40</u>  | <u>2.5.20 01:15</u>  | <u>35</u>                       | <u>358</u>                                | <u>95.2</u>   | <u>0</u>                               | <u>-0.1</u>   | <u>8.3</u>                             | <u>W</u>                |

## References

- Beddows, D.C.S., Harrison, R.M., Green, D.C, Fuller, G.W., 2015. Receptor modelling of both particle composition and size distribution from a background site in London, UK. *Atmos. Chem. and Phys.* 15, 10107-10125.
- Leoni, C., Pokorná, P., Hovorka, J., Masiol, M., Topinka, J., Zhao, Y., Krůmal, K., Cliff, S., Mikuška, P., Hopke, P.K., 2018. Source apportionment of number size distributions and mass chemical composition in a European air pollution hot spot. *Environmental Pollution* 234, 145-154.

- Masiol, M., Vu, T. V., Beddows D. C. S., Harrison R. M., 2016. Source apportionment of wide range particle size spectra and black carbon collected at the airport of Venice (Italy). Atmos. Environ. 139, 56-74.
- Pokorná, P., Leoni, C., Schwarz, J., Ondráček, J., Ondráčková, L., Vodička, P., Zíková, N., Moravec, P., Bendl, J., Klán, M., Hovorka, J., Zhao, Y., Cliff, S.S., Ždímal, V., Hopke, P.K., 2020. Spatial-temporal variability of aerosol sources based on chemical composition and particle number size distributions in an urban settlement influenced by metallurgical industry. Environmental Science and Pollution Research 27, 38631–38643.
- Sowlat, M H., Hasheminassab S., Sioutas C., 2016. Source apportionment of ambient particle number concentrations in central Los Angeles using positive matrix factorization (PMF). Atmos. Chem. Phys 16, 4849-4866.
- Zíková, N., Pokorná, P., Makeš, O., Sedlák, P., Pešice, P., Ždímal, V., 2020. Activation of atmospheric aerosol in fog and low clouds. Atmospheric Environment 230, 117490, 1–11.